UNIVERSITÀ DELLA CALABRIA

Dipartimento di MECCANICA

DOTTORATO DI RICERCA IN INGEGNERIA MECCANICA

CICLO XXIII (2007-2010)

S.S.D. ING-IND/14 Mechanical Design and Machine Building

Biomechanics of the Human Eye Sclera

A Dissertation Submitted in Partial Fulfilment of the Requirements

for the Doctoral Research Degree in Mechanical Engineering

Doctoral Research Director

Prof. Sergio RIZZUTI

Supervisors

Dr. Eng. Luigi BRUNO

Eng. J. Crawford DOWNS, PhD

Candidate

Dr. Eng. Massimo Antonio FAZIO

Abstract

The biomechanics of the optic nerve head and peripapillary sclera have been hypothesized to play a central role in the individual susceptibility to glaucoma, which is the second leading cause of blindness worldwide.

The aim of this work is to provide a mechanical testing and experimental data analysis procedure to characterize mechanical properties of human sclera.

The overall goal of performing scleral tissue mechanical testing is to elucidate the role of ocular biomechanics in the development of this disease by constructing eye-specific finite element models of the posterior pole.

In this work it has been developed and validated a new methodology for computing sub-micrometer scale IOP-induced deformation obtained during pressurization testing of human scleral shells.
Genetic Algorithm-based procedure and a microstructure-based numerical fitting method have been adopted to assess structural material properties of the testes eyes.

Preliminaries results show the range of nonlinear, anisotropic mechanical properties of posterior sclera from normal eyes of human donors.

Acknowledgments

I would like to thank you some colleagues and friends that helped me during my studies on ocular tissue biomechanics.

I want to thank you *Amedeo Lucente* who introduced me in the study of the Glaucoma disease. He has been an invaluable source of motivations on ideas.

I want to give a special thanks to *Juan Reynaud* who daily supported me in all the lab issues during the experimental testing period.

I am profoundly thankful to *Crawford Downs* for every single help I received in the daily work spent at Devers Eye Institute and for providing me all the training I received about ocular tissue biomechanics.

I thank you *Ian Sigal* and *Rafael Grytz* for being an inexhaustible source of ideas, motivations, discussions, and human support.

I will be always thankful to *Andrea Poggialini* and *Luigi Bruno* for taking care of my technical formation. They have been much more than the mentors of my carrier.

TABLE OF CONTENTS

Introduction

The Importance of the Biomechanics of Human Sclera

The sclera is the most extensive load bearing tissue of the eye. Its major function is to provide structural support to the other two most extended tissues of the eye, the choroid and the retina. The retina is the tissue containing the optical receptors of the eye, while the choroid is meant to provide the nutritional blood supply to the retina.

The spherical shape of the eye is essential to allow the rays of light coming into the eye to be in focus on the retina. The sphericity of the eye is achieved by maintaining positive pressure the liquid inside the eye (i.e. humor vitreous and aqueous). This pressurized liquid creates a hydrostatic load on the ocular coats that is commonly referred to as intraocular pressure (IOP). Mechanically, the IOP inside the eye creates a hydraulic load, and the main function of the sclera is to provide structural stiffness to carry this mechanical load. The sclera also provides structural support to the choroid and the retina.

IOP is usually indirectly measured by applanation tonometers and its normal value is in the range of 10 - 21 *mmHg* (millimeters of Mercury). A pathological increase of IOP is associated to an increased risk in developing an optic neuropathy called glaucoma.

Glaucoma is the second leading cause of blindness in the world after cataracts, although cataracts can be treated surgically to reverse blindness. Loss of vision due to glaucoma is irreversible.

The mechanisms of damage to the retinal ganglion cell axons in glaucoma is not well understood, but it is hypothesized that elevated IOP affects the biomechanics of the tissues of the eye. In particular, glaucomatous damage takes place at the optic nerve head (ONH), a structure through which the axons that transport the visual information exit the eye on their path to the

brain. It is thought that the ONH is particularly susceptible to the effects of IOP, as it is generally less mechanically resistant to increased pressure loads. The sclera plays the major role in the global mechanical behavior of the eye, as it is the principal load bearing tissue of the globe. The sclera also surrounds the ONH, and therefore plays an important role in the biomechanics of the ONH.

In order to build an understanding of the role of ocular biomechanics in glaucoma, one must possess a detailed characterization of the mechanical properties of the sclera. The aim of this work is to develop a testing and analysis procedure for the mechanical characterization of the scleral tissue from human donor eyes.

The Existing Scleral Testing and Data Analysis Method

The mechanical testing procedure that served as the basis of this work is based on a procedure previously developed by Michael Girard in studies of scleral biomechanics in the monkey model of glaucoma (Girard M. J., 2008).

The existing procedure was based on the inflation test of posterior sclera shells clamped and imaged in a customized apparatus. The deformations experienced by the pressurized scleral shell were recorded by a commercial laser speckle interferometer (Q100, Dantec Dynamics A/S, Denmark), and the deformation field was calculated by the commercial software package that accompanied the interferometer. The computed experimental displacement fields were then used as the target displacement for a genetic algorithm-based inverse finite element procedure that fitted a set of mechanical parameters (defining the material model assumed to describe the mechanics of the sclera). The mechanical parameter set was varied until the finite element model displacement predictions closely matched the experimentally measured displacement field.

Eyemesh, a semi-automated *Matlab*^{TM} routine written by Michael Girard, was used to create an individual specific FE model of the tested eye. *Eyemesh* requires the following data inputs:

- A point cloud obtained from a 3D mechanical digitizer that was used to represent the 3D shape of the scleral outer surface.
- Scleral thickness measurements at 20 discrete locations collected by using an ultrasound transducer.
- The 3D displacements of the scleral outer surface calculated by the commercial software package that accompanied the interferometer.

These input data required a great deal of manual pre-processing, and were fraught with error as described in the next section.

Description of the Activities Performed by the Candidate During the 3 Years of the Doctoral Research Course

The goal the presented work was to revise, modify, and extend the previous work done by Michal Girard in mechanical testing of monkey sclera shells in order to perform automated, error corrected, mechanical testing of human scleral shells, and allow subsequent calculation of accurate mechanical properties.

A customized routine has been written in *Mathematica*^{TM} to reconstruct the experimentally recorded displacement fields from the raw interferometer output, thereby bypassing the erroneous processing in the commercial interferometry software. All the optical errors inherent in the testing set-up were taken into account. This approach eliminated substantial errors in the displacement field calculation previously disregarded by the commercial software package.

The corrected displacement fields computed by the new custom routine were then used as the target values of a material property fitting procedure to estimate the material properties of the sclera. The derived custom routine

eliminated the errors in the experimentally measured displacement maps, which otherwise would cascade into wrong and missleading fitted scleral material properties.

In particular, portions of the genetic algorithm procedure were rewritten in *Fortran 77* and *Fortran 90* to perform a different numerical formulation of the eye-specific FE models used to estimate the sclera's mechanical response to the load produced by IOP.

The *Eyemesh* routine was modified and extended such that all the tasks necessary to create the individual specific FE model of the eye are completely automated. This automation brought some important improvements:

- A vast reduction in processing time.
- An objective and repeatable pre-processing of the experimental data.
- The addition of graphic-based control of the experimental data pre-processing.

Previously, the 3D displacement fields were calculated by the commercial software that accompanied the interferometer. This software has been entirely replaced by new custom routine written in *Mathematica*^{TM} that reconstructs the experimental displacement fields at any IOP level directly from the raw data recorded by the interferometer. The key features of the now fully automated processing program are the following:

- Direct management of the raw data recorded by the interferometer and of the scleral thickness and scleral surface geometry data.
- Computation of the absolute phase change maps of the recorded speckle field (a function of the recorded deformation fields) by performing a custom *unwrapping* procedure.
- Elimination of the errors associated with the change of the laser wavelength and the angle of the laser beams induced by speckle

recording through an optical window in a saline-filled chamber (refraction changes).

- Providing a mathematical representation of the geometry of the scleral shell, and of the experimentally recorded 3D displacement fields.

The new analysis procedure is now performed by this completely automated, graphics-assisted program. The new program completely replaced the previously described *Eyemesh* routine, except for the creation of the nodal coordinates of the scleral shell finite element mesh.

Introduction to the Chapters of this Dissertation

The present dissertation is split in several chapters each one describing a step of the work done in the 3 years Doctoral Research Course attended by the candidate. The main topic of each chapter is summarized in the following list:

Chapter 1: In this chapter, the importance of sclera biomechanics and how it potentially relates to the mechanical damage seen in Glaucoma is discussed.

Chapter 2: In this chapter, an overview on speckle methodology is presented. The speckle methodology presents the basis of the interferometric technique used to record the scleral surface displacement fields during mechanical pressure testing.

Chapter 3: This chapter gives a detailed description of the experimental set-up used to perform the mechanical inflation test and a description of the testing instrumentation. Furthermore, the mathematical formulation used for the constitutive material description and the inverse FE models are presented.

Chapter 4: In this chapter, the procedure to analyze the experimental data from mechanical inflation test is described. This includes the management

and computation of the speckle interferometric data. After a brief introduction to the genetic algorithm-based optimization technique, it is here introduced the genetic algorithm used in this work, and how material properties are computed adopting this procedure is presented.

Chapter 5: Preliminary results obtained by the genetic algorithm-based fitting procedure and achieved by the analysis performed on four human eyes are reported in this chapter. Results shown in this section have been obtained by the genetic algorithm-based procedure described in Chapter 4, and the main outcomes of the procedure are analyzed and discussed.

Chapter 6: In this chapter, the new computational method that was developed to analyze the recorded speckle interferometric data is introduced and described. The optical set-up used in the scleral inflation experiments did not satisfy the simplifying assumptions typically employed in classic holography (and used by the commercial software accompanying the interferometer); the developed procedure accounts for all the optical features considering the real testing conditions of the mechanical testing procedure and of the experimental set-up are described.

Chapter 7: A microstructure-based numerical fitting method developed by Rafael Grytz is presented. This fitting method is used to estimate the mechanical properties of the human sclera form the corrected displacement measurments. It allows to assess some important features of the biological structure of the scleral tissue. Some preliminary results obtained with this new approach are reported.

Chapter 8: This chapter includes the discussion of the preliminary results obtained from the genetic algorithm-based procedure (Chapter 4) and from the microstructure-based numerical fitting method (Chapter 7).

Chapter 1

Glaucoma and Ocular Tissues Biomechanics

1.1. Introduction

The principal aim of this work is to provide a mechanical testing and analysis procedure to assess the mechanical properties of human eye sclera. Mechanical testing has been performed on about 40 pairs of human eyes and 4 pairs of monkey eyes with advanced experimental glaucoma.

The mechanical testing of the scleral shells from the human donor eyes has been carried out to fulfill the aims of the following grants from the U.S. National Institute of Health:

- NIH R01-EY018926, *Age-related Changes in Optic Nerve Head Structure and Biomechanics.*

  Principal investigators: *J. Crawford Downs and Christopher A. Girkin.*

- NIH R01-EY019333 *Racial Variations in Optic Nerve Head Structure and Biomechanics.*

  Principal investigators: *J. Crawford Downs and Christopher A. Girkin.*

Tested eyes from human cadaver have been collected from young normal donors and old normal donors of European descent, as well as donors of African descent.

The overall goals of these projects are to evaluate the influence of ocular biomechanics on the increased age- and race-related susceptibility to glaucoma. In particular, the presented work focuses on the differences in scleral stiffness due to aging and racial variations, and how scleral mechanical properties affect the biomechanics of ONH in the human eye.

The ONH biomechanics are understood here as the interactions between IOP and the connective tissues of the ONH and peripapillary sclera, or in particular, the structural stiffness these tissues (the combination of tissue architecture and material properties). Our overarching hypothesis is that the ONH biomechanics are inextricably linked, either primarily or secondarily, to IOP-related and pathophysiologic changes in the blood flow, nutrient diffusion and cellular activity within those tissues. The immediate goals of focused in this research grants are to characterize age- and race-related differences in ONH biomechanics and elucidate their effects on ONH susceptibility to IOP insult. The long-term goal of the research proposal is to develop clinical diagnostics and interventions designed to manage each important biomechanical risk factor in the development and progression of glaucoma.

Sclera biomechanics is thought to be important in the development and progression of glaucomatous optic neuropathy. This is described in the *Age-related Changes in Optic Nerve Head Structure and Biomechanics* grant proposal submission made by the Principal investigator of this research proposal J. Crawford Downs, which is included below. This grant proposal provides a brief, detailed review of the scientific considerations on the topic that lead to the formulation of the hypothesis that changes in sclera mechanical properties (considered dependent to aging and ethnicity) are likely to increase the vulnerability of the ONH connective and neural tissues to IOP-related axonal injury in glaucoma.

1.2. The ONH as a Biomechanical Structure

The lamina cribrosa (Figure 1) provides structural and functional support to the retinal ganglion cell (RGC) axons as they pass from the relatively high-pressure environment within the eye to a lower pressure region in the retrobulbar cerebrospinal space (Zeimer, 1995). To protect the RGCs in this unique anatomic region, the lamina in higher primates has developed into a complex structure composed of a three-dimensional network of flexible

beams of connective tissue, nourished by a capillary bed primarily arising from the short posterior ciliary arteries penetrating the immediate peripapillary sclera (Burgoyne, Downs, Bellezza, & Hart, 2004) (Burgoyne, Downs, Bellezza, Suh, & Hart, 2005) (Quigley & Addicks, 1981) (Jeffery, Evans, Albon, Duance, Neal, & Dawidek, 1995). This intra-scleral and intra-laminar vasculature is unique in that it is encased in load-bearing connective tissue, either within the scleral wall adjacent to the lamina cribrosa, or within architecture of the laminar beams themselves (Hayreh, 1986).

The anatomy of the lamina cribrosa and peripapillary sclera merits several considerations regarding the etiology of glaucomatous cupping and implies that the classic “mechanical” and “vascular” mechanisms of glaucomatous injury (Fechtner & Weinreb, 1994) are inseparably intertwined (Burgoyne, Downs, Bellezza, Suh, & Hart, 2005) (Figure 2 and Figure 3). For example, prior to structural damage, purely IOP-related stress could detrimentally affect the blood supply to the laminar segments of the axons by direct deformation of the capillary-containing connective tissue structures or due to changes in the extracellular matrix that may limit the diffusion of nutrients to RGC axons in the laminar region. Reciprocally, primary insufficiency in vascular supply to the laminar region could induce connective tissue changes that would serve to weaken the laminar beams, making them more prone to failure under similar levels of IOP-related mechanical stress.

To incorporate these concepts within a global hypothesis, a biomechanical model of glaucomatous optic neuropathy has been proposed (Burgoyne, Downs, Bellezza, Suh, & Hart, 2005). This model proposes that IOP-related stress and strain play an essential and causative role in the pathophysiology of the changes seen in all of the tissue types within the ONH and in its blood supply. These not only include the load-bearing connective tissues within the lamina cribrosa, the scleral canal wall, and the peripapillary sclera, but also the cellular components of these tissues, including astrocytes, glial cells, endothelial cells, and pericytes, along with their basement membranes and the RGC axons.

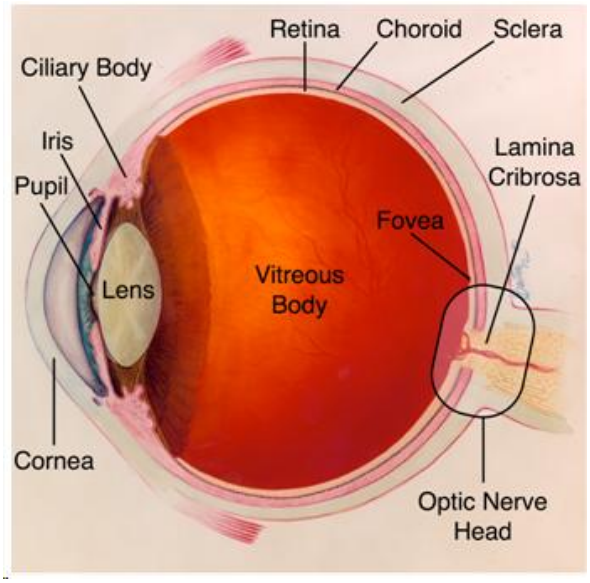

Figure 1. Anatomy of the human eye. Lamina cribrosa is highlighted in the boxed region at the posterior pole. Figure provided by the National Eye institute and National institutes of Health, http://www.nei.nih.gov/photo/.

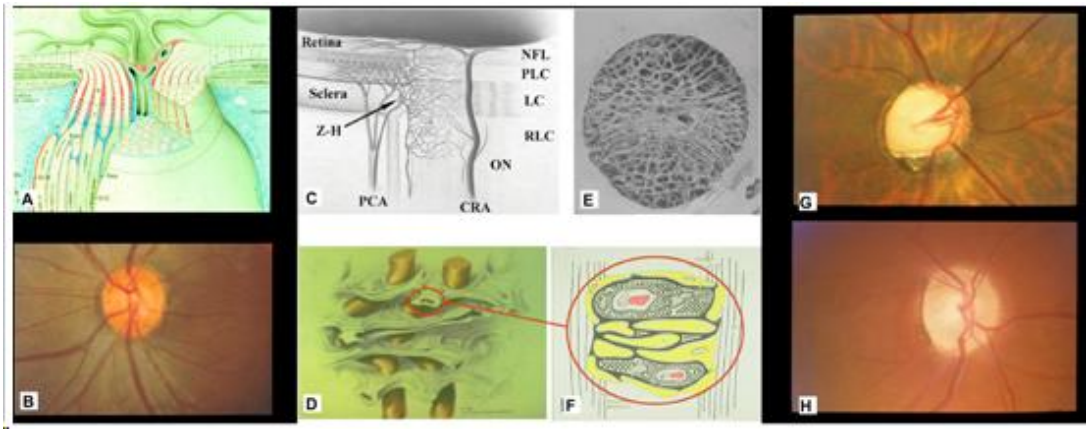

Figure 2. The optic nerve head (ONH) is influenced by IOP-related stress and strain. (A) The ONH is made up of prelaminar, laminar and retrolaminar regions. (B) Within the clinically visible surface of the normal ONH (also referred to as the optic disc), central retinal vessels enter the eye and retinal ganglion cell (RGC) axons appear pink/orange due to their capillaries. (C) the blood supply for the laminar region (LC) is from the posterior ciliary arteries (PCA). The primary site of RGC axon insult in glaucoma is within the lamina cribrosa, which is schematically depicted with axon bundles (brown) in (D). The laminar connective tissues, isolated by trypsin digest in a scanning electron micrograph in (E), provide structural support to the ONH, which is the weak spot in an otherwise strong pressure vessel. The laminar beams, drawn in (F) with stippled extracellular matrix (ECM), central capillary (red) and surrounding astrocytes (yellow with basement membranes in black), also contain the capillary network and much of the cellular structure that support the axons in the laminar zone. The clinical manifestation of IOP-induced damage to the ONH is most commonly “deep cupping” (G), but in some eyes cupping can be shallower accompanied by pallor (H). Z-H, circle of Zinn-Haller; PCA, posterior ciliary arteries; NFL, nerve fiber layer; PLC, prelaminar region; LC, lamina cribrosa; RLC, retrolaminar region; ON, optic nerve; CRA, central retinal artery. (A) Reprinted with permission from Doug Anderson ; (C) reprinted with permission from Cioffi GA; (D) Reprinted with permission from Quigley HA; (E) Reprinted with permission from Quigley HA; (F) Reprinted with permission from Morrison JC.

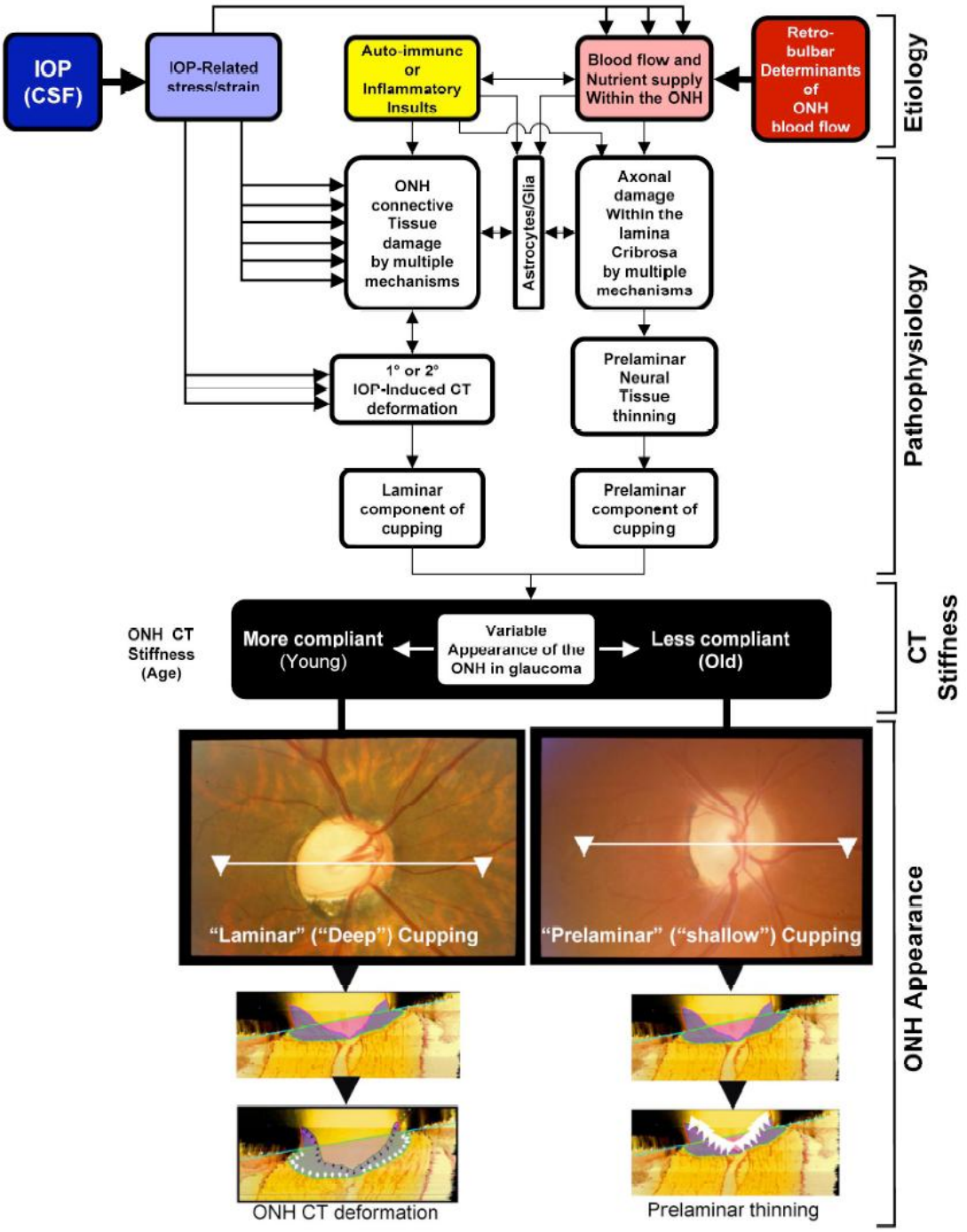

Figure 3. IOP-related stress and strain influence both the ONH connective tissues (CT) and the volume flow of blood primarily, and the delivery of nutrients secondarily, through chronic alterations in CT stiffness and diffusion properties (blue and red). Other primary insults to the ONH CT (yellow) can damage the ONH CT and/or axons. Once damaged, ONH CT can become more or less rigid depending upon lamina cribrosa astrocyte and glial response. If weakened, ONH CT deform in a predictable manner. The clinical ONH appearance of cupping can be divided into "laminar" and "prelaminar" components. Prelaminar cupping follows loss of prelaminar neural tissues without laminar involvement (white arrows, lower right). Deep or laminar cupping follows ONH CT damage and deformation. Laminar cupping is important because it establishes that IOP is actively involved (either 1°or 2°). Laminar cupping may be accompanied by a prelaminar component (small black arrows, lower left).

Regardless of the primary insult in glaucomatous injury, IOP-related stress and strain in the laminar connective tissues are key elements in this model and are dependent on the 3D ONH architecture and material properties of these connective tissues (Zeimer R. , 1995) (Burgoyne, Downs, Bellezza, Suh, & Hart, 2005) (Burgoyne & Morrison, 2001) (Quigley H, 1995) (Bellezza, Rintalan, Thompson, Downs, Hart, & Burgoyne, 2003) (Downs, Suh, Thomas, Bellezza, Hart, & Burgoyne, 2005) (Quigley & Addicks, 1981) (Sigal, Flanagan, & Ethier, 2005) (Zeimer & Ogura, 1989).

1.3. Association Between Normal Aging and the Vulnerability to IOP Related Injury

The results of the several randomized prospective trials have identified the risk factors associated with the development or progression of Glaucoma (Table 1) (AGIS Investigators, 2002) (EGPS Investigators, 2007) (Leskea, Heijl, Hyman, Bengtsson, & Komaroff, 2003). Across several studies, IOP, age, central corneal thickness, increased optic disc cupping, and African ancestry are independently associated with glaucomatous progression. It is important to note that all of these risk factors have a biologically plausible association with either the level of IOP, the severity of disease (visual field severity), or biomechanical properties of the ONH (age, (Albon, Purslow, Karwatowski, & Easty, 2000), African ancestry (Girkin, McGwin, & Xie, 2005), corneal thickness (Lesk, Hafez, & Descovich, 2006), increased cupping).

Importantly, age is the only risk factor other than IOP that is independently associated with the onset and progression of glaucoma across all of the major prospective clinical trials conducted over the past twenty years.

Table 1. Risk factors for glaucomatous progression	
Risk Factor	**Prospective Study**
Increasing Age	**AGIS, CIGTS, EMGT, OHTS, EGPS**
African Ancestry	AGIS, CIGTS, CNGTS
Visual Field Severity	EMGTS, AGIS, OHTS, EGPS
Diabetes	AGIS, CIGTS
Disc Hemorrhage	EMGT, CNGTS
Follow-up IOP	EMGT, CNGTS
Cup-Disc Ratio	OHTS, EGPS
Corneal Thickness	OHTS, EGPS
Pseudoexfoliation	EMGT
Initial IOP	EMGT
Female Gender	CNTGS
Male Gender	AGIS

AGIS, Advanced Glaucoma Intervention Study [34]; **EMGT,** Early Manifest Glaucoma Treatment Study [38]; **CIGTS**, Collaborative Initial Glaucoma Treatment Study; **CNTGS**, Collaborative Normal Tension Glaucoma Study [35]; **OHTS**, Ocular Hypertension Treatment study [37]; **EGPS,** European Glaucoma Prevention Study [36]

In addition to data from prospective trials in glaucoma and ocular hypertension, every population-based survey conducted to date has demonstrated a strong relationship between the prevalence of glaucoma with advancing age (Rudnicka, Mt-Isa, Owen, Cook, & Ashby, 2006), despite almost all studies showing no changes in IOP (Leske, Connell, Wu, Hyman, & Schachat, 1997) (Weih, Mukesh, McCarty, & Taylor, 2001). Furthermore, while normal tension glaucoma is not uncommon within elderly populations (Levene, 1980) (Chumbley & Brubaker, 1976), it is not seen in children or young adults other than in a few isolated case reports (Geijssen, 1991). These findings indicate that the aging ONH becomes increasingly vulnerable to glaucomatous injury at similar levels of IOP.

Developing techniques to quantify the biomechanical behavior of the ONH will allow for the determination of how the affects of aging are mediated in the causality of glaucomatous injury. This will also form the groundwork for continued studies investigating the effects of individual variation in ONH structure and biomechanics on the vulnerability to IOP-related injury as seen in at–risk groups such as individuals of African ancestry.

1.4. The Affects of Normal Aging on ONH Biomechanics

As with any solid structure, the degree of local deformation (strain) experienced by the ONH under a given level of stress is dependent upon its 3D architecture and material properties (Bellezza, Hart, & Burgoyne, 2000) (Downs, Suh, Thomas, Bellezza, Hart, & Burgoyne, 2005) (Sigal, Flanagan, & Ethier, 2005). Thus, variation in ONH anatomy and material properties that occur with aging may account for the increased susceptibility to IOP-induced injury (Figure 3 and Figure 4).

Previous researches have shown that even at physiologic level of IOP substantial stress and strain may occur within the lamina and peripapillary sclera that may lead to alteration in the ONH architecture (Bellezza, Hart, & Burgoyne, 2000) with subsequent increase in the vulnerability to mechanical failure.

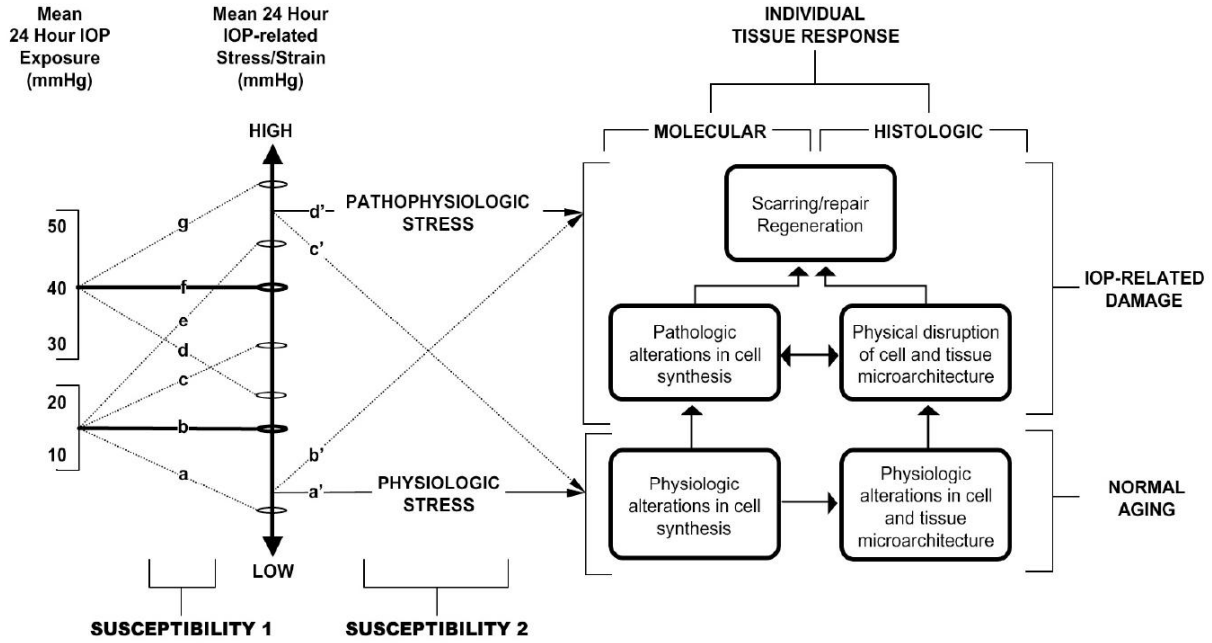

Figure 4. The complex relationships between normal aging, IOP, mechanical stress and strain, and ONH susceptibility. Susceptibility 1: for a given ONH, IOP generates low or high levels of mechanical stress and strain depending upon the 3D architecture and mechanical properties of the ONH connective tissues. Some ONHs will have relatively low mechanical stress at high IOP (d), while others will have high mechanical stress at low IOP (e). Susceptibility 2: Whether a given level of IOP-related stress and strain is physiologic or pathophysiologic depends upon the individual ONH's resistance to IOP-related connective tissue strain, blood flow reduction, and cellular activation, all of which are affected by aging. Strong connective tissues, a robust blood supply and stable astrocytes and glia should increase the chance of an individual undergoing normal ONH aging and withstanding the deleterious effects of IOP, even if that IOP is higher than normal.

It has also been shown that the material properties of the sclera are altered early in glaucoma in the monkey model (Downs, Suh, Thomas, Bellezza, Hart, & Burgoyne, 2005), which indicates that the cellular response to connective tissue strain can quickly alter the mechanical behavior of the tissue.

These findings may have important clinical ramifications in that for a given magnitude of IOP insult, the aged ONH ought to demonstrate shallower cupping than a young ONH, as seen in the senile sclerotic variant of glaucoma (Broadway, Nicolela, & Drance, 1999) (Nicolela MT, 1996). Interestingly, preliminary data from an analysis of imaging results from patients participating in a longitudinal glaucoma study seem to indicate that older patients tend to have shallower degrees of cupping than young patients when controlled for disease severity, race, pre-treatment IOP, and current IOP.

1.5. Changes in Laminar Material Properties and Morphology with Age

A variety of age-related changes in the ONH connective tissue may affect ONH compliance (Morrison, LHernault, Jerdan, & Quigley, 1989) (Albon, et al., 2007) (Albon J. , Karwatowski, Avery, Easty, & Duance, 1995) (Bailey, Paul, & Knott, 1998) (Hernandez MR, 1989). In the young adult, the laminar beams are composed of a central core of elastin fibers and fibrillar collagen surrounded by basement membrane components (collagen IV, and laminin). During aging, immunohistochemistry has demonstrated increases in collagens I, III, IV, and V, along with thickening of the elastic fibers within the laminar beams. In addition, quantitative studies revealed an increase in the total collagen and advanced glycation end products, with reduction in the proportion of collagen III, total sulphated glycosaminoglycans, and lipid concentration (Quigley, Brown, Morrison, & Drance, 1990) (Albon, et al., 2007) (Albon J. , Karwatowski, Easty, Sims, & Duance, 2000) (Brown, Vural,

Johnson, & Trinkaus-Randall, 1994) (Hernandez MR, 1989). In all, these changes should result in a stiffening of the connective tissues of the ONH (Zeimer & Ogura, 1989) (Albon, Purslow, Karwatowski, & Easty, 2000).

Age-related increases in the thickness of the laminar beams have been reported, with associated reductions in the proportional area of laminar pores [63,66]. Since changes in morphology will affect the biomechanical behavior of any load bearing structure, these age-related morphologic variations certainly must exert some effect on the biomechanical behavior of the ONH.

1.6. Changes in Biomechanical Behavior with Age

Several *in-vivo* techniques have been developed to study the compliance of the ONH. In cadaver eyes, ONH compliance has been quantified using scanning laser tomography (Burgoyne, Mercante, & Thompson, 2002) (Yan, Coloma, Metheetrairut, Trope, Heathcote, & Ethier, 1994), Doppler velocimetry (Zeimer, Wilensky, Goldberg, & Solin, 1981), and radiographic evaluation of platinum wires embedded within the lamina (Zeimer & Ogura, 1989). Albon and colleagues demonstrated that there is an overall increase in structural stiffness of the lamina cribrosa with age, with greater deformation of the lamina seen in younger eyes at any given IOP (Albon, Purslow, Karwatowski, & Easty, 2000). While these results confirm the increased stiffness of the lamina with age, they are limited to imaging only the surface of the lamina and peripapillary sclera.

Sigal and colleagues determined that variations in scleral thickness, radius of the eye, laminar stiffness, and scleral thickness have the greatest influence on the biomechanical response of the ONH using finite element modeling based on axisymmetric idealized geometries (Sigal, Flanagan, Tertinegg, & Ethier, 2004). This research demonstrates that variation in the material properties of the sclera and lamina are important determinates of the stress/strain relationship within the ONH. However, these idealized models lack sufficient anatomic detail to define the biomechanical changes within the

microarchitecture of the lamina, which is the primary site of axonal injury. In contrast to prior work, this proposal will combine methods that will define both the material properties and microarchitecture of the ONH necessary to develop biomechanical models based on individual human eyes.

Chapter 2

Speckle interferometry - Theoretical Introduction

2.1. The Speckle Phenomenon

When a surface - with a roughness greater than or equal to the wavelength of the illuminating light - is illuminated with a coherent light beam at a certain distance from the surface, it can be observed in a field of light characterized by a myriad of light and dark spots randomly distributed in the space. This speckle phenomenon is created by the scattering of light waves when reflected by the rough surface. Theoretically, this phenomenon can occur not only when the illuminating light is in the visible spectrum, but it can be also generated by other oscillatory phenomena of different wavelengths such as radio waves or X-ray.

The formation of these structures was observed the first time by researchers working in the field of holography. The speckle was thus initially considered as a noise effect inevitably superimposed on the information encoded in the recorded holographic fringes. The speckle signal was later investigated as a means of measurement. The statistical distribution of light intensity, amplitude, and phase of the electromagnetic field generated by the speckle effect have been obtained theoretically (Goodman, 1975).

A spatial random distribution of a speckle field is shown Figure 5, in which the three-dimensional surfaces are equal light intensity regions.

The size of the single speckle, denoted by δ, is a very important parameter.

It can be evaluated using the following formula:

$$\delta = 1.22 \frac{\lambda z}{D} \qquad \text{(eq. 1)}$$

where λ is the wavelength of the light source, z and D are defined in terms of how the speckle field is observed.

If the speckle is directly observed (without any optical means) it is termed *objective speckle* and in this case *z* is the distance between the observation point and the observed surface, while *D* is the diameter of the illuminated area (assumed to be circular and uniformly illuminated).

If the surface is observed through a lens, it is termed *subjective speckle*; in this case, *z* is the distance between the plane of the lens and the plane of focus, while *D* is the diameter of the smallest lens in the optical set-up used.

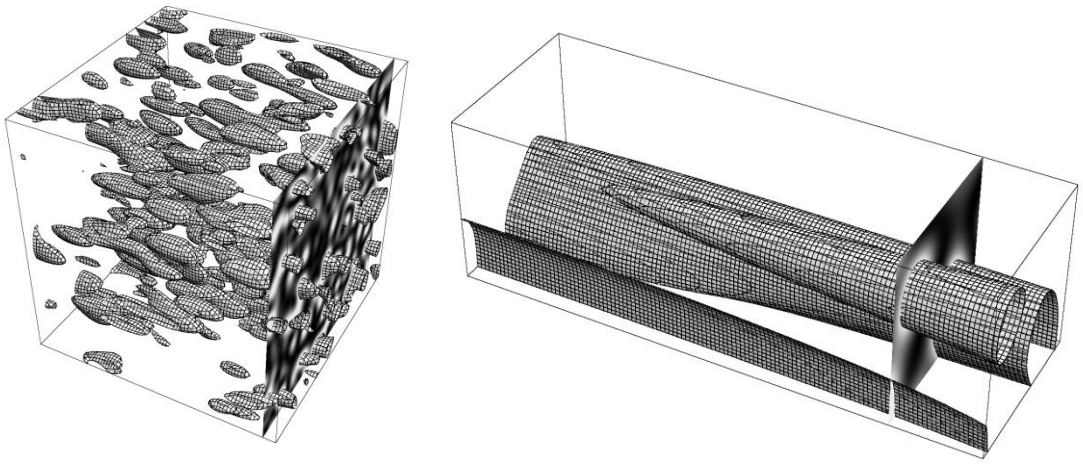

Figure 5. Three-dimensional reconstruction of the speckle observed at far distance (left) and short distance (right).

For this reason, the speckle size changes as a function of the observation distance *z*.

The transverse size of the speckle also changes as a function of the optical set-up. In this case, the size of the single speckle is

$$\delta = 8\,\lambda\frac{z}{D} \qquad \text{(eq. 2)}$$

It can be seen in Figure 5 that the surfaces of the speckle are quite spherical and the structure changes rapidly when viewed from afar (left side), but the speckles tend to stretch and grow when viewed closely (right side), and the structure tends to remain the same.

This last condition is necessary for conducting experimental measurements using the speckle phenomenon. In fact, this speckle field created by illuminating a rough surface can be directly used for applications such as metrology.

Speckle effect can be regarded as a sort of “fingerprint” of a surface, and it can be used to detect any changes in the surface as rigid motions or local deformations.

Some techniques based on digital correlation or aperiodic decorrelation of speckle fields have been adopted by many researchers. Digital correlation (Oliver & Pharr, 1992) (De Fazio, Syngellakis, & Fugiuele, 2001) is a technique that can be regarded as the modern version of the speckle photography (Beghini M, 1999). Speckle photography consists of using a photographic plate to record the same speckle field at two different configurations, i.e. before and after the observed surface is deformed. To measure deformations by exploiting the speckle phenomenon, it is necessary that interference occur between the speckle field generated by the beam illuminating the observed surface and another light field consistent with the first (created by a beam generally called *reference beam*).

The basic principle is shown schematically in Figure 6, wherein two coherent sources interfere with each other. If one source undergoes a shift at a generic point in space, it produces a cyclical variation of the light intensity whose frequency depends on the wavelength of illuminating light used.

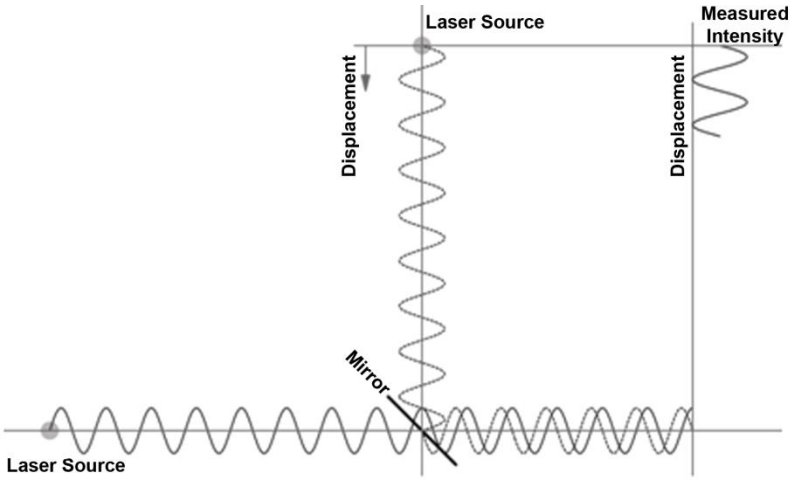

Figure 6. Schematic representation of an interferometer.

So, if two stationary waves with same frequency interfere, the resulting light intensity (L_{int}) depends only on the phase relationship existing between the two waves. Using a complex notation, the resulting light intensity equation for a generic stationary wave can be written as follow:

$$L_{int} = Ae^{j\emptyset} \quad \text{(eq. 3)}$$

where *A* represents the waves amplitude and ϕ the phase value. By summing the two interfering waves and calculating the resulting intensity, it can be shown that:

$$L_{int} = \left\| A_1 e^{j\emptyset_1} + A_2 e^{j\emptyset_2} \right\| = {A_1}^2 + {A_2}^2 + 2A_1A_2\cos(\emptyset_1 - \emptyset_2) \quad \text{(eq.4)}$$

The evolution of the resulting intensity is shown in Figure 7, where it can be seen that the change in light intensity depends on the phase difference. Hence, the cyclical variation in light intensity can be traced back to the dealignment between the two sources that created the phase difference.

Speckle interferometry, as well as holographic interferometry, have the advantage of being able to operate on surfaces that don't need to be observed along their normal direction because the light is diffused by the

object and theoretically, every point in the space has a light intensity that is function of the diffused light made by all the points on the surface.

This feature imputes a great advantage to speckle interferometry in that it is able to measure both out-of-plane displacement components (as in classical interferometry) and in-plane components (such as in moiré interferometry) of displacement.

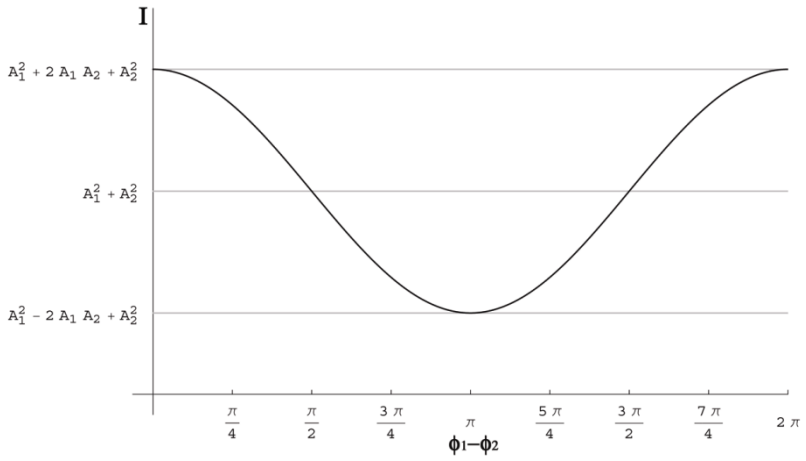

Figure 7. Resulting light intensity as a function of the phase shift $\emptyset_1 - \emptyset_2$

Alternate and Mean values are plotted in the ordinate coordinate axis.

2.2. Interferometers for Measuring Displacements

As shown by the multitude of scientific publications (Doval, 2000) (Sirohi R. S., 2002) and specialized texts (Erf, 1978) (Sirohi, Speckle metrology, 1993) there are different types of interferometers that have been proposed by many researchers working in speckle interferometry. One way to classify interferometers has been proposed in (Bruno & Poggialini, 2000), where the classification is made on the basis of which displacement component the device is sensitive to, and on how the illumination and observation directions are set up.

Another feature that distinguishes an interferometer is the number of beams used for illuminating the object. By using this classification method

interferometers are classified as *single* or *double illumination*, depending on the number of light sources, and *single* or *double observation*, depending on how many images of the object observed are focused on the CCD of the observation camera.

The interferometer used in this work can be classified as a S*ingle-Light and Single-Image Absolute interferometer.*

2.3. Single-Light and Single-Image Absolute interferometer

This kind of interferometer is the simplest set-up, it is sensible to only a single generally oriented displacement component. By considering in the Figure 8 a generic point P(*x,y,z*) belonging to the surface under examination, it is possible to define a direction of illumination by joining the light source point S and the generic point P. The direction of observation can be defined by joining the point P and the observation point O (which normally coincides with the optical center of the lens). The direction of illumination and observation are uniquely identified by two unit vectors k_i and k_o, and the angle between the viewing directions and lighting is *2* θ.

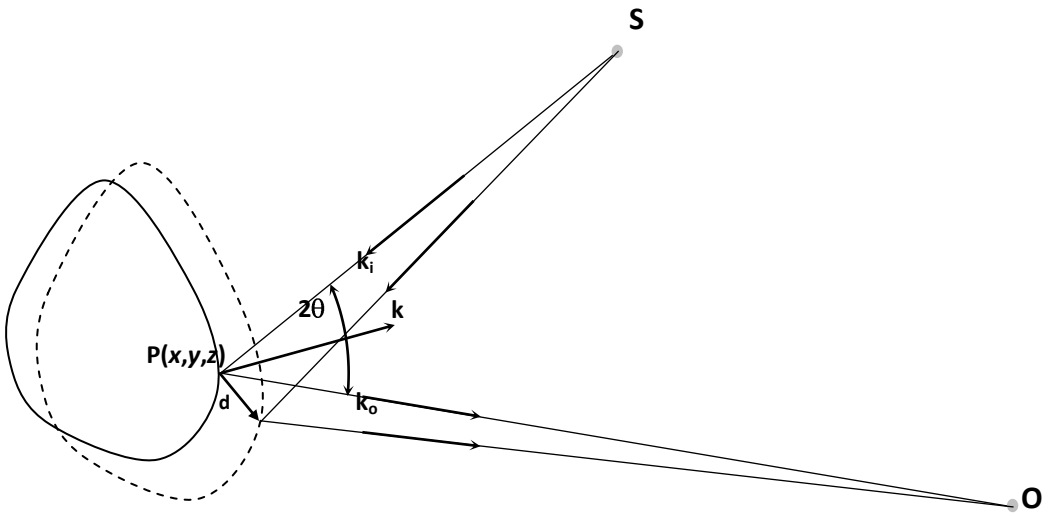

Figure 8. Schematic representation of a *Single-light and Single-image Absolute Interferometer.*

Indicating with $\vec{d}$= $\{d_x, d_y, d_z\}$ the shift affecting the point P and neglecting (in this instance) the variations of the unit vectors $\vec{K_i}$ and $\vec{K_o}$, it can be written the well known formula of the holographic interferometry (Vest, 1979)(still applicable in speckle interferometry):

$$\phi = \frac{2\pi}{\lambda} \vec{d}.(\vec{K_i} - \vec{K_o}) = d_x K_x + d_y K_y + d_z K_z \qquad \text{(eq. 5)}$$

where λ is the wavelength of the used light and ϕ is the phase shift that arises due to the displacement $\vec{d}$. The vector $\vec{K}$=(K_x, K_y, K_z) is called sensitivity vector, its module is $(\frac{4\cos\theta\,\pi}{\lambda})$ and it is oriented along the line bisecting the illumination and the observation directions.

Therefore, by using an interferometer of this type is theoretically possible to measure a displacement vector oriented along any direction in the space.

By choosing a suitable point of view and three linearly independent lighting directions, it is possible to reconstruct three independent displacement components describing the surface deformation.

Of course, the determination of the phase change must be made by using a reference beam interfering with the light diffused by the object and constant in direction throughout the deformation of the object.

It has to be considered that the observed objects are never perfectly diffusing and most of the light is sent back, more or less, in the direction of illumination. This implies that to have good contrasted light intensity distributions in the space the sensitivity vector has to lay close to the illuminating direction

2.4. Double Illumination and Dual Image Differential Interferometer

In the case of double illumination and dual image differential interferometer the phase relationship is obtained differentiating the phase relationship of the single image interferometer.

The optical set-up of this interferometer is shown in Figure 9, and the relation between the change in phase with the measurements is the follows:

$$\delta\emptyset = \Delta K_x\left(\frac{\partial d_x}{\partial x}dx + \frac{\partial d_y}{\partial y}dy\right) + \Delta K_x\left(\frac{\partial d_y}{\partial x}dx + \frac{\partial d_y}{\partial y}dy\right) + \\ +\Delta K_z\left(\frac{\partial d_z}{\partial x}dx + \frac{\partial d_z}{\partial y}dy\right) \qquad \text{(eq. 6)}$$

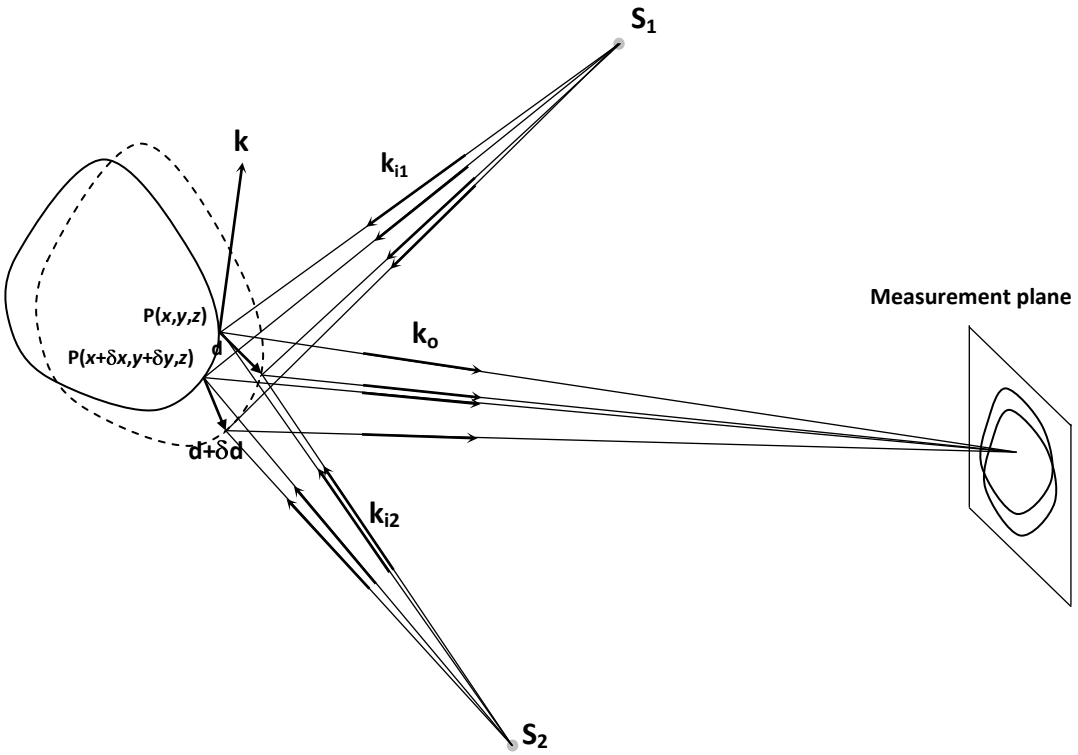

Figure 9. Geometry of a differential interferometer with double lighting and double image.

This type of interferometer is mainly sensitive to the in-plane components, so it is suitable to measure the first derivatives of displacements in the plane.
This type of interferometer (shearing interferometer or shearometer) is not widely used due to the low visibility of the fringes (Tyrer & Petzing, 1997).
An interesting application of this interferometer has been recently adopted to analyze human corneas shell mechanical properties (Knox Cartwright, Tyrer, & Marshall, 2010).
A more effective method to measure the first derivatives of the in-plan displacements is to use the shearometer by recording two measures in order to have a sensitivity vector symmetrical to the normal (Steinchen, Kupfer, Mäckel l, & Vössing, 1999) (Fan, Wang, & Tan, 1997).
In this way, by using a simple sum and difference operation on the double measurement of the phase detected at any point, it is possible to separate the in-plan and out-of-plane deformation components.

2.5. The Phenomenon of Speckle Decorrelation

Using speckle interferometry as a measuring device for deformations introduces some carefulness to be taken into account. The most relevant problem that has to be avoided is the *speckle decorrelation*.

This phenomenon occurs when there is a change in the structure of the speckle field. In speckle interferometry it is assumed that while a point of a surface is undergoing a deformation each pixel of the camera keeps intercepting the same portion of the speckle field created by the surface.

The light intensity varies cyclically according to the diagram of Figure 7 and the cyclical variation has to be compared with the light intensity spatial distribution of the undeformed body using a simple subtraction operation. The decorrelation occurs when a portion of the speckle field intercepted by a pixel changes. In this case the light intensity of the deformed condition cannot be compared with the reference condition. of course, this phenomenon does not occur instantaneously but it occurs gradually.

There are several models to explain the decorrelation, and the simplest geometric model is shown schematically in Figure 10 (Bruno, Pagnotta, & Poggialini, 2000) where speckle decorrelation is due to a rigid rotation of the surface. The objective speckle field moves in front of the lens changing the structure of the speckle observed by a single pixel. The decorrelation of the field is higher the most the lens is far and the most is great the rotation ψ.

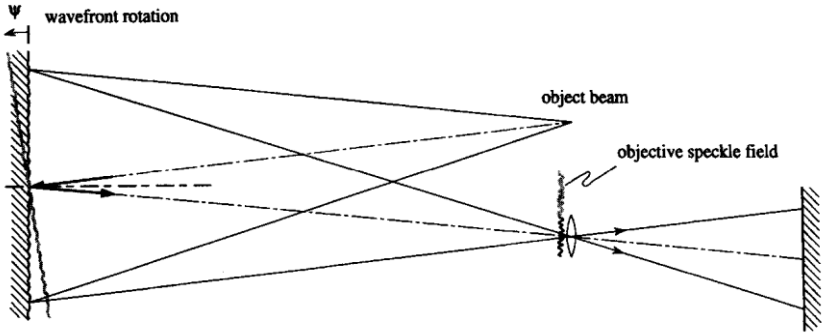

Figure 10. Schematic model of the decorrelation effect due to a rotation of the observed surface.

Without addressing particular details to the problem of decorrelation, for which aim there are many articles in the literature (Huntley, 1997) (Lehmann, 1997) (Joenathan, Haible, & Tiziani, 1999), it can be assessed that in the most of the cases decorrelation effects cannot be compensate. In particular, it is never possible to recover the decorrelation due to oxidation or surface plasticity, nor for decorrelation induced by particular cases of large deformations.

Instead, in theory at least, decorrelation can be compensated when made by effects of rigid motions of the observed body. Speckle decorrelation compensation technique can be adopted in some cases to properly reconstruct the speckle field (Molimard, Cordero, & Vautrin, 2008) (Hung, Wang, & Hovanesian, 1997).

2.6. Determination of the Phase

Figure 7 shows a sinusoidal variation in light intensity made by two interfering sources and how light intensity can be characterized by a mean value and an alternate value commonly named average and modulation intensity.

Figure 11 it is shown a vector-based diagram that plots on the horizontal axis the measured light intensity represented as the projection on this axis of the vector sum of the average intensity i_m (always parallel to the horizontal axis) and the modulation i_a (whose contribution depends on the value of the phase).

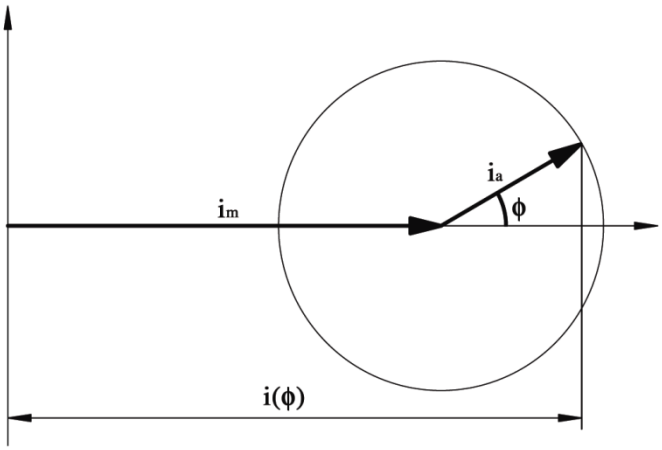

Figure 11. Light intensity as a function of the phase value Ø.

A useful notation to represent the light intensity as a function of the phase value is the complex notation:

$$i\ (\emptyset) = i_m + i_a \cos(\emptyset) \qquad \text{(eq. 7)}$$

Each pixel of the image can be considered as a standalone speckle interferometer. The light intensity detected for each pixel contains three bits

of information: the phase value (Ø), the average intensity (i_m) and modulation (i_a). Therefore, to determine these three variables, it has to be performed three independent measurements of the light intensity. To obtain these three characteristics of the light intensity it is necessary to introduce a known variations of phase so that it can be defined an invertible system of equations. It is also possible to make a larger number of measurements obtaining a system with a redundant number of equations. In this way the unknowns will be obtained through a method of minimization that would allow a reduction of measurement errors.

A known phase shifts α_i can be introduced by changing the length of the optical path in one of the two interfering beams.

If a phase shift of α_i is introduced, the detected intensity light would be:

$$i_i = i_m + i_a \cos(\emptyset + \alpha_i) = i_m + i_a \cos \emptyset \cos\alpha_i - i_a \sin \emptyset \sin \alpha_i$$

(eq. 8)

The easiest way to impose these phase shifts (though not always the cheapest) is to shift a mirror with piezoelectric actuators, which are devices capable of controlling with high stability and repeatability movements of the order of the light wavelength.

For N measurements it can be obtained a redundant system of equations:

$$\begin{vmatrix} 1 & \cos\alpha_1 & -\sin\alpha_1 \\ 1 & \cos\alpha_2 & -\sin\alpha_2 \\ \vdots & \vdots & \vdots \\ 1 & \cos\alpha_N & -\sin\alpha_N \end{vmatrix} \begin{Bmatrix} i_m \\ i_{a\mathrm{Re}} \\ i_{a\mathrm{Im}} \end{Bmatrix} = \begin{Bmatrix} i_1 \\ i_2 \\ \vdots \\ i_N \end{Bmatrix} \qquad \text{(eq. 9)}$$

with $i_{a\mathrm{Re}} = i_a \cos \emptyset$ and $i_{a\mathrm{Re}} = i_a \sin \emptyset$

With $\mathbf{M}$ the coefficient matrix, which depends only on the introduced phase shifts, and $\mathbf{I}$ the vector of known values obtained from the measured intensity. The real part, the complex part, and the modulation of the intensity light can be derived using the following equations:

Defining $$\mathbf{M} = \begin{vmatrix} 1 & \cos\alpha_1 & -\sin\alpha_1 \\ 1 & \cos\alpha_2 & -\sin\alpha_2 \\ \vdots & \vdots & \vdots \\ 1 & \cos\alpha_N & -\sin\alpha_N \end{vmatrix} \text{ and } \mathbf{I} = \begin{Bmatrix} i_1 \\ i_2 \\ \vdots \\ i_N \end{Bmatrix} \qquad \text{(eq. 10)}$$

Light intensity components can be obtained as follow:

$$\begin{Bmatrix} i_m \\ i_{a\mathrm{Re}} \\ i_{a\mathrm{Im}} \end{Bmatrix} = (\mathbf{M}^T\mathbf{M})^{-1}\mathbf{M}^T\mathbf{I} \qquad \text{(eq. 11)}$$

Phase and modulation can be now obtained by:

$$i_m = \sqrt{{i_{a\mathrm{Re}}}^2 + {i_{a\mathrm{Im}}}^2} \qquad \text{(eq. 12)}$$

$$\theta = \arctan\frac{i_{a\mathrm{Im}}}{i_{a\mathrm{Re}}} \qquad \text{(eq. 13)}$$

A so defined phase have a value included in the interval [- π, π [.

Chapter 3

Investigation Methods

3.1. Introduction

In this chapter, the constitutive model used in this work to model the scleral material response and its physiologic motivation will be presented. In addition, the choice of an inflation test as the mechanical testing procedure will be discussed. The experimental set-up used to perform the inflation test on the sclera shells will be described.

3.2. Preliminary Considerations

Soft tissues often show having a little compressibility when hydrostatically compressed. A parameter used to express the elastic compressibility of a material is the bulk modulus (B), that when expressed as a function of the elastic modulus (E) and of the coefficient of Poisson (ν) takes the form:

$$B = \frac{E}{3(1-2\nu)} \qquad \text{(eq. 14)}$$

B can be also expressed as a function of the volume (V) change of the tissue:

$$B = -P / (\Delta V / V) \qquad \text{(eq. 15)}$$

An incompressible material or a barely compressible material doesn't change in volume when uniformly compressed by a pressure load. These materials are usually considered as having an infinite value of the bulk modulus. Because of that, Poisson ratio value for incompressible material is usually approximated to about 0.5.

$$\lim_{\nu \to 0.5} \frac{E}{3(1-2\nu)} = \infty \qquad \text{(eq. 16)}$$

Biological soft tissues have a high water content, and human sclera consists of about 70% water (Nicoli, et al., 2009). This high water content makes the sclera barely compressible when hydrostatically loaded.

The high density of collagen fibers in the sclera is responsible of the non-linear mechanical behavior. When the tissue is unloaded, collagen fibers crimp or buckle. When mechanically loaded, the induced deformation of the tissue straightens and stretches the collagen fibers constituting the sclera. Straightening the collagen fiber crimp results in a nonlinear stiffening of the tissue (Grytz & Meschke 2009). Because of the inhomogeneous alignment of these collagen fibers, the sclera is characterized by an anisotropic (or orientation dependent) constitutive response as has been reported for porcine sclera (Girard M. J., Downs, Burgoyne, & Suh, 2008), monkey sclera (Girard M. J., Downs, Bottlang, Burgoyne, & F. Suh, 2009), and in human sclera by using a bi-axial testing procedure (Eilaghi, Flanagan, Tertinegg, Simmons, Brodland, & Ethier, 2010).

Incompressibility, non-linearity and anisotropy make the mechanical characterization of this tissue difficult to achieve.

The first studies on mechanical characterization of scleral tissue used simplified material models and low-resolution techniques for fitting experimental data obtained by traction test (Friberg & Lace, 1988) and inflation test (Woo, Kobayashi, Schlegel, & Lawrence, 1972).

While these first attempts to find a load-deformation relationship are still valid references for a qualitatively estimation of the constitutive response of human sclera, more detailed and extensive analysis are needed to quantitatively estimate the anisotropic non-linear sclera mechanical properties.

A common approach of mechanical characterization of soft tissues is based on techniques of reverse engineering. This procedure consists of finding a

set of material properties best fitting experimental data directly measurable on the investigated material.

Reverse engineering technique applied on soft tissue is a new branch of scientific research. For this reason, material models implemented ad hoc for describing mechanical behavior of soft tissues are in progress of development. While material models based on physical parameters at the micro- and meso-scales have recently been developed (Grytz & Meschke, Constitutive modeling of crimped collagen fibrils in soft tissues, 2009), engineers originally approached biological tissues characterization by using phenomenological material models.

The tendency of biological tissue to allow large deformations when mechanically loaded, their incompressible behavior, and the anisotropy caused by the inhomogeneous distribution of its collagen fibers, make the scleral constitutive response similar to a fiber reinforced rubber- like material.

Available rubber-like material constitutive models account for finite deformations, non linearity, as well as for anisotropic fiber-architecture.

Moreover, rubber-like material constitutive models are often formulated to account for incompressibility.

Due to their capability to fit complex mechanical behaviors, rubber-like constitutive models are considered as suitable to be used in the mechanical characterization of biological soft tissues by mean of reverse engineering procedure.

3.3. Material Constitutive Model

Constitutive model of rubbers are predominantly formulated by defining a *strain energy density function* whose derivative with respect to the strain describes the stress tensor.

Strain energy function (W) is a scalar valued function describing the amount of elastic energy stored in the material. It doesn't account for the loading condition history of the material, neither for thermal loads.

For isotropic homogenous materials the strain energy function is commonly written as a function of the principal stretches ($\lambda_1, \lambda_2, \lambda_3$) or of the deformation invariants (I_1, I_2, I_3).

$$W = \hat{W}(\lambda_1, \lambda_2, \lambda_3) = \tilde{W}(I_1, I_2, I_3) = \bar{W}(\bar{I}_1, \bar{I}_2, J) = U(I_1^c, I_2^c, I_3^c)$$

$$\bar{I}_1 = J^{-2/3}\ I_1\ ; \quad I_1 = \lambda_1^2 + \lambda_2^2 + \lambda_3^2\ ; \quad J = \det(\boldsymbol{F})$$
$$\bar{I}_2 = J^{-4/3}\ I_2\ ; \quad I_2 = \lambda_1^2\lambda_2^2 + \lambda_2^2\lambda_3^2 + \lambda_3^2\lambda_1^2 \qquad \text{(eq. 17)}$$

As mentioned, biological tissues are constituted by collagen fibers whose rate of alignment depends on the nature of the tissue. For example, tendons have a high rate of collagen fibers alignment making this tissue strongly anisotropic; at the opposite, collagen fibers in skin are randomly distributed, this confers an isotropic mechanical behavior to this soft tissue (Fratzl, 2008). Collagen fibers distribution stands in the middle of these two extreme cases. Fibers orientation rate widely changes through the whole sclera tissue. Sclera exhibits both regions with high and very low rate of fibers' alignment.

Histological analysis on human sclera gave a rough mapping of collagen fibers distribution as shown Figure 12 (Kokott, 1934).

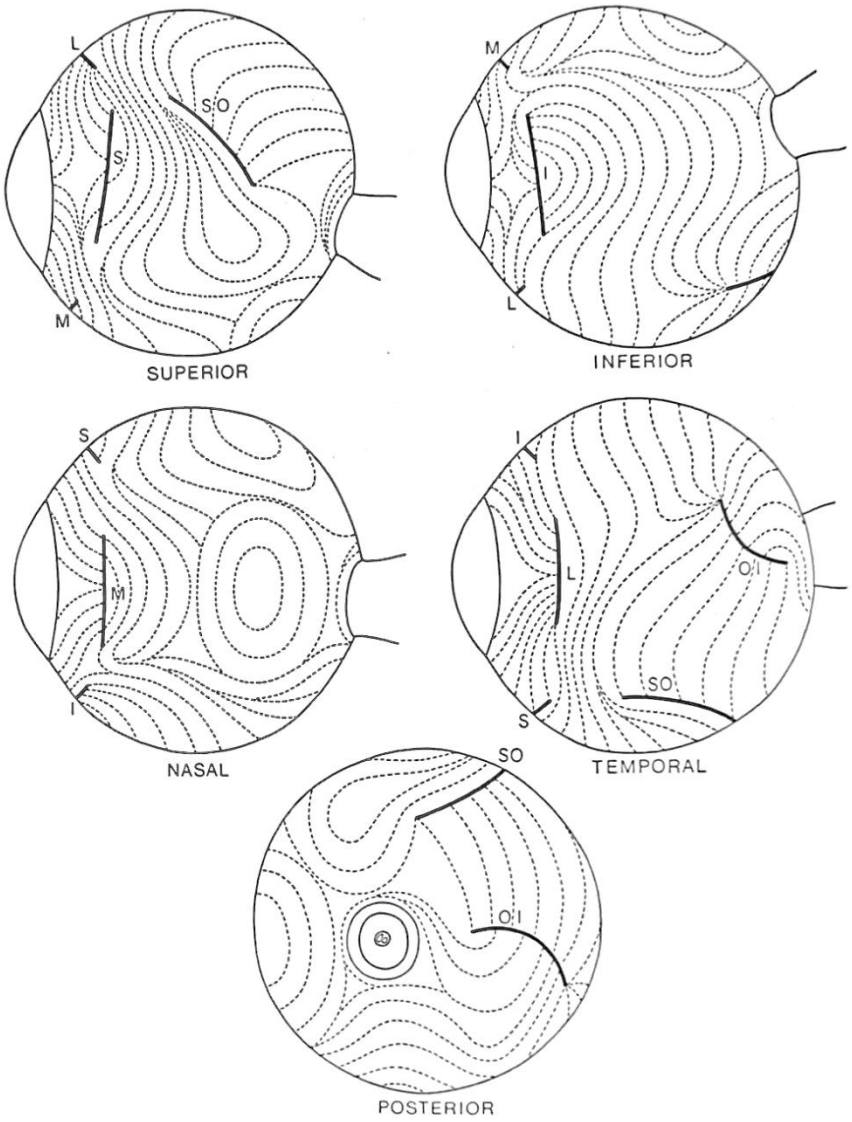

Figure 12. Fiber distribution obtained by histological section (Kokott, 1934); fiber orientation widely changes in the different regions of the sclera.

Modern techniques such Small Angle Laser Scattering applied on rats (Girard, Dahlmann, Vijay, Khaw, & Ethier, 2010) and other optical techniques based on laser scattering (Yan, McPheeters, Johnson, Utzinger, & Vande Geest, 2010) confirmed this not homogeneous distribution of the collagen fibers distribution through the whole sclera.

While elasticity is a reasonable hypothesis to be considered, linearity and isotropic behavior are clearly not suitable for describing such a complex structure present in the sclera.

The sclera can be macroscopically considered as constituted by two major constituents:

1. A ground substance matrix which contains the elastin fibers, proteoglycans, fibroblasts, tissue fluid and all other tissue constituents except collagen.
2. Collagen fibers.

Since the structural stiffness of the ground substance is much lower than the stiffness of the collagen fibers, its anisotropic contribution to the constitutive response can be disregarded. Therefore, the ground substance matrix is assumed to deform isotropically.

With these physiologically-based assumptions, the sclera can be thought as a fiber-reinforced hyperelastic material.

To account for anisotropy, strain energy function (W) can be reformulated decoupling an isotropic (W_{isotr}) plus a transverse isotropic ($W_{transv.isotr}$) energetic contribution (Weiss, Maker, & Govindjee, 1996).

$$W = W_{isotr} + W_{transv.isotr} \qquad \text{(eq. 18)}$$

This formulation can be definitively adopted to built a material constitutive model describing sclera mechanics.

Deformation of the ground substance matrix can be accounted in the isotropic part of the strain energy function, while collagen stretching can be considered affecting the transverse isotropic energetic contribution part of the function.

Use of a transverse isotropic model is justified by a mechanical interpretation of a physiological feature of the scleral tissue.

Collagen fiber direction is assumed to be stress orientation dependent, as it has been observed in bones remodeling (Wolff, 1892) and in cardiac tissue (Rubbens, Mol, Boerboom, Bank, & Baaijens, 2009).

While a physiological explanation of this collagen fibers' attitude is not clearly revealed, it is experimentally observed that collagen fiber orientation changes as a function of the stress/strain surrounding conditions.

Eye bulb can be considered as a thin walled recipient under pressure, so stress field can be considered approximately constant through eye's thickness (Timoshenko, 1940). By considering the mentioned stress-dependent orientation feature of collagen fibers and relating it to an approximately constant stress field through the thickness of the sclera, we assume that collagen fibers architecture doesn't significantly change through the sclera thickness.

In this condition the anisotropic behavior of this tissue is represented by a transverse isotropic formulation.

3.4. The Inflation Test

Adopting a material constitutive model depending on the principal stretch components to describe the mechanical behavior of this soft tissue arises important complexities in the mechanical testing procedure.

A purely traction test carried on strips of sclera tissue would create a mono-directional strain deformation field. In that case the only not null component of the stress tensor would be the one oriented along the traction direction.

While perfectly suitable to characterize linear elastic response of typical engineering materials such as steel or other rigid metals, traction tests seem not be a suitable testing procedure components of . A multi-axial mechanical test has to be performed to assess a multi-parameter of a hyperelastic constitutive model (Kao & Razgunas, 1986) such as the one used in this work. Furthermore, anisotropic characteristics cannot be assessed by a single uniaxial test.

The eye can be understood as an nearly spherical recipient subjected to intra-ocular pressure produced by the internal liquid constituting the humor vitreous. The nearly spherical geometry makes the eye a self-equilibrating hyperstatic structure. In this condition the stress tensor does not only

dependent on the loading condition, but it is also dependent on the eye geometry.

Because of these mechanical features, an experimental testing set-up that preserves the natural geometrical configuration of the tissue might result in a more realistic mechanical characterization of the tissue properties compared to uniaxial or biaxial testing of tissue strips.

The nonlinear mechanical response of the slera makes its material properties dependent on the absolute magnitude of the tissue deformation. Clamping effects, stress concentration effects, and geometrical distortions caused by the loading procedure may alterate the experimental measurements and should, therefore, be minimized.

Bi-axial tests are widely used in hyperelastic material characterization since multi-directional stress condition may be investigated. Bi-axial testing is commonly performed on thin soft materials, such as rubber-based membranes.

In case of an in-plane stress loading condition, several simplifying assumptions can be incorporated on the tensor describing the stress condition in the material. For this reason, biaxial and uniaxial tests need to minimize undesired bending momentum forces that would introduce out-of-plane stress components in the stress tensor violating the typically applied assumptions.

While bi-axial test can be considered as a 2-dimensional testing procedure, inflation tests are performed on 3-dimensional shaped specimens.

Hyperelastic material models are usually calibrated and validated by FEM modeling of the testing procedure. Therefore, it is desirable to keep the loading condition during the experiment close to the idealized one considered in the FEM model.

Thin rubber-like membranes are useful materials to validate experimental procedures such as inflation tests as they satisfy the equi-biaxal stress

conditions in the center of the inflated membrane, thereby achieving a uniform stress distribution similar to the idealized condition considered in the FEM formulation.

The physiological spherical shape of the eye can be closely maintained during an inflation experiment. Accordingly, experimental data obtained from inflation tests can be considered as a suitable basis for inverse engineering techniques, which try to elucidate realistic biomechanical properties of scleral shells.

3.5. Inflation Test Set-up

In this section the customized charging apparatus used to perform the inflation tests on the scleral tissue samples is presented. The testing set-up used in this work was modified from a previous set-up used on monkey scleral tissue samples (Girard M. J., Downs, Bottlang, Burgoyne, & F. Suh, 2009). The customized testing set-up is illustrated in Figure 13.

A circular hole was machined in the clamping stage to accept stainless steel clamping rings of different sizes. Clamping is performed by elevating the vertical stage and by squeezing the tissue close to the equatorial region of the posterior pole of the scleral shell between the border of the steel ring and the plastic ring shown in Figure 14. This clamping condition eliminates any rigid movements of the sample during the mechanical test and ensures the sealing condition that is always verified after clamping the eye.

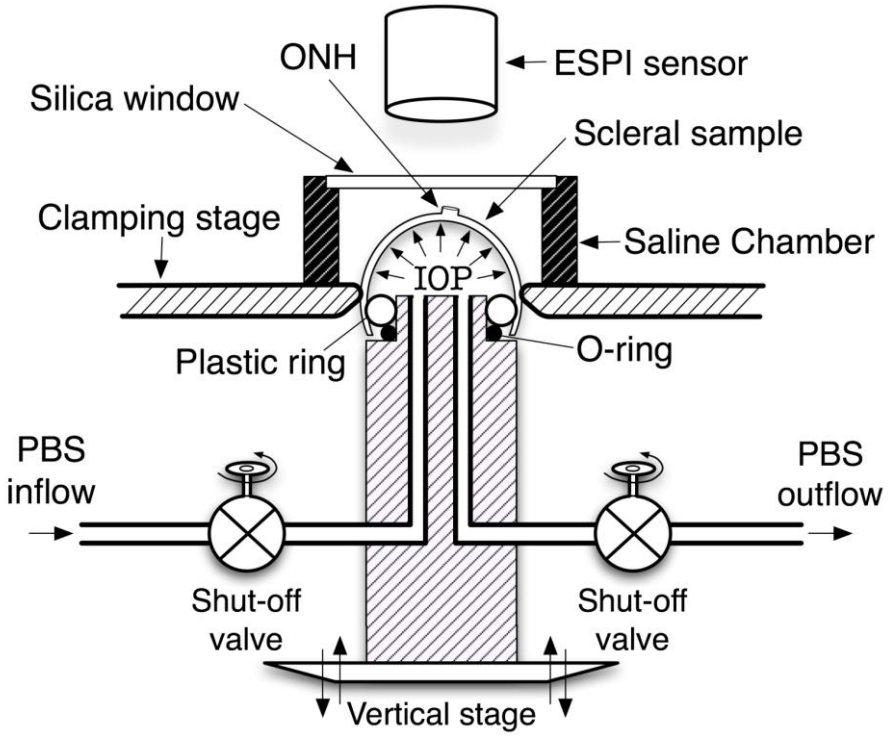

Figure 13. Charging apparatus for mechanical inflation test.

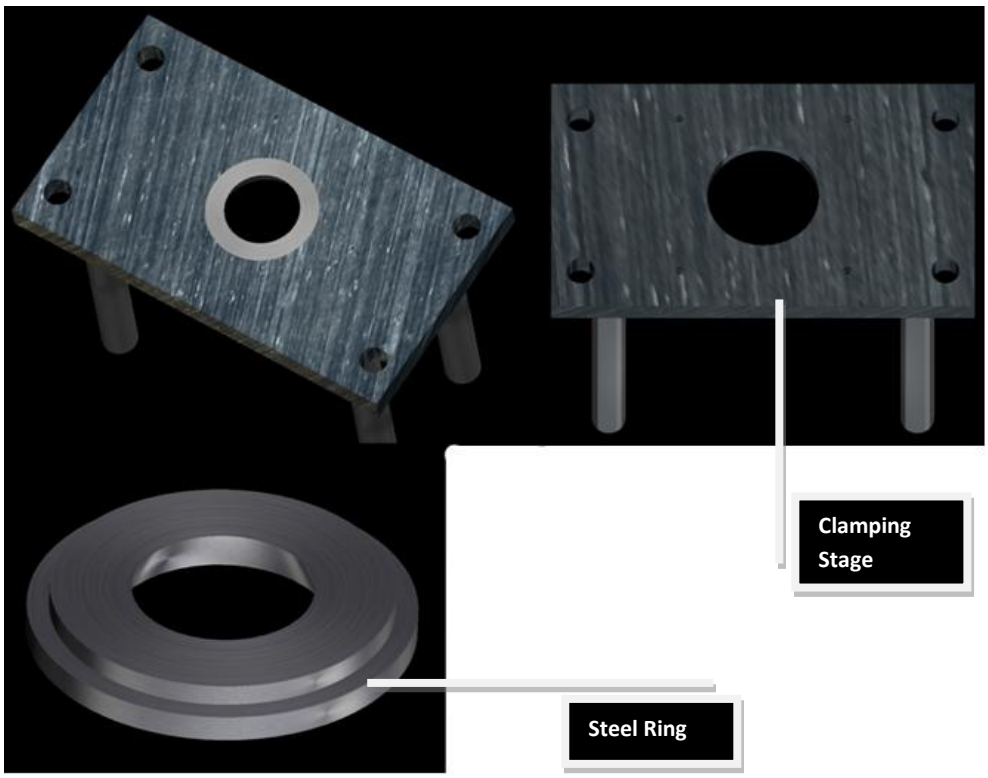

Figure 14. Clamping stage after and before the steel ring is mounted.

A sealed chamber filled of saline solution (Phosphate Buffered Saline, or PBS) is mounted on the steel plate. The saline chamber (Figure 15) maintains tissue hydration during the entire inflation test.

Two fluid lines allow for inflow and outflow of saline solution inside the hemisphere of the eye mounted on the pressurization apparatus. The pressure inside the eye is controlled by a digital manometer connected in parallel to the outflow line.

Pressure increases are obtained by raising a bottle of saline solution via a motor-controlled vertical stage. An automated system controls the pressure step increase by integrating information from the digital manometer with the position of the saline bottle.

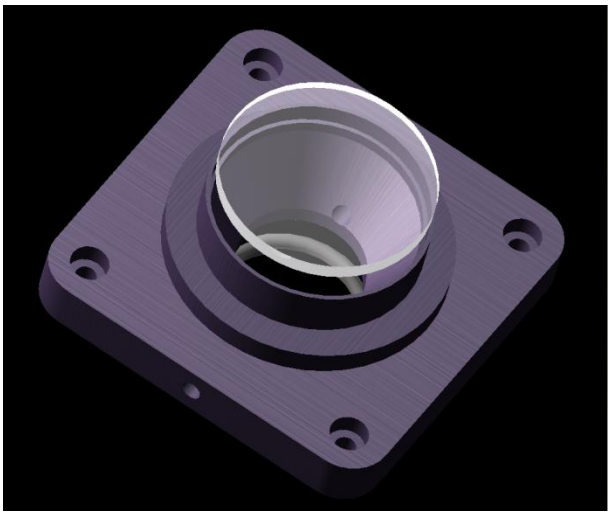

Figure 15. Saline chamber mounted on the pressurization apparatus.

The phase variations of the speckle fields caused by the deformation of the outer scleral surface induced by the pressure increase is recorded by a commercial Electronic Speckle Pattern interferometer (Q100, Dantec Dynamics A/S, Denmark).

The interferometer consists of a unit containing four lasers symmetrically positioned around the CCD (Coupled Charge Device) of the unit, connected to a central controller.

Part of the final set-up is shown in Figure 16.

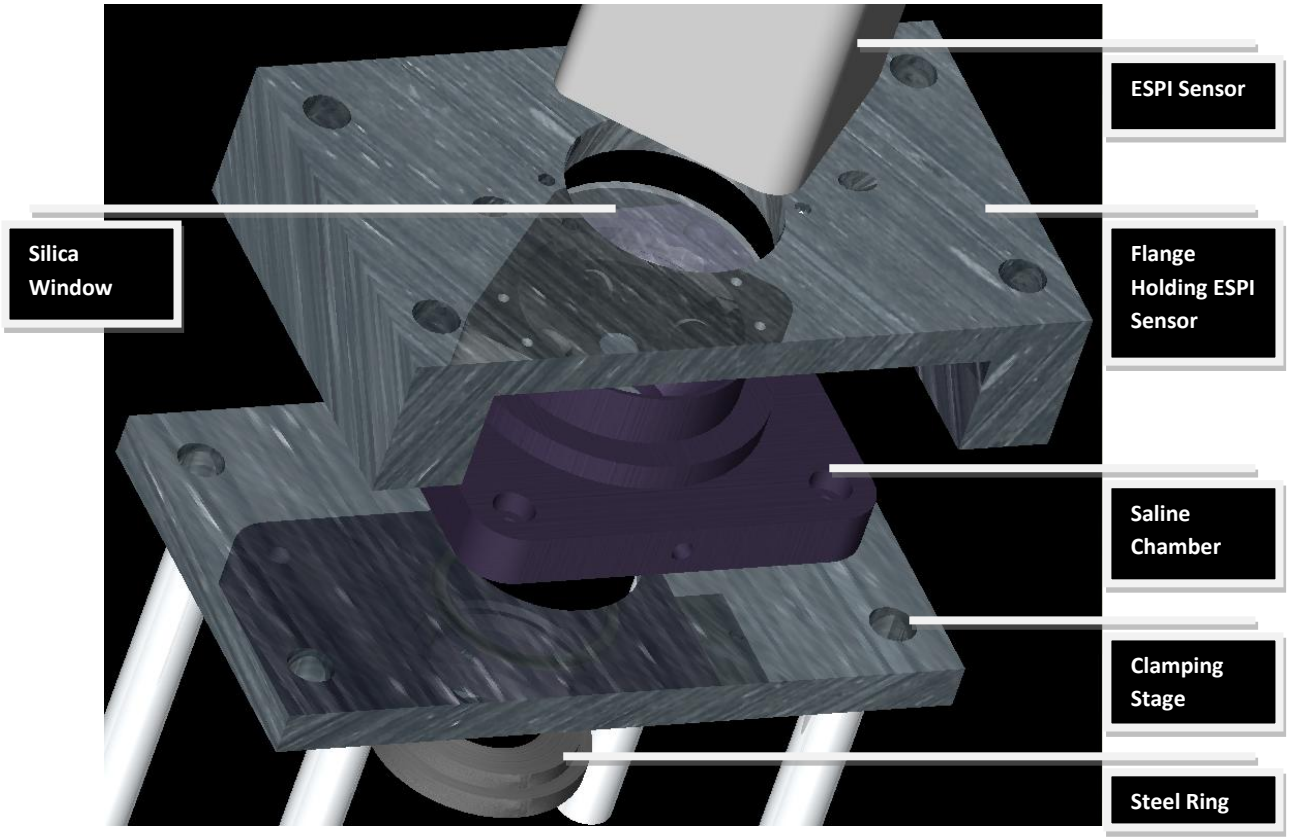

Figure 16. Part of the experimental set-up for the mechanical testing.

All the figures describing the mechanical testing set-up have been made in Pro-Engineer™. During the data collection period the following parts were redesign from its original form: The Design of new components have been designed with the mentioned CAD program.

For all the tested eyes internal pressure has been raised from a baseline of 5 *mmHg* up to 45 *mmHg.* The baseline of 0 *mmHg* couldn't be used since the posterior hemisphere doesn't keep its shape at zero pressure. A 5 *mmHg* initial internal pressure was just enough to pre-stretch the eye into its natural shape while keeping the pre-existing stress low.

Each scleral shell was subjected to IOP preconditioning, consisting of 20 IOP cycles from 5 *mmHg* to a maximum of 30 *mmHg* at a rate of 5 *mmHg* per second, and then allowed to recover for 15 minutes.

Soft tissues mechanical behavior is affected at several ways by preconditioning loads (Cheng, Clarke, & Bilston, 2009), and physiological changes made by preconditioning on soft tissues it is still not clarified. Fortunately, studies on porcine thoracic aortas has shown that testing of soft tissue carried using equi-biaxial test procedure makes the tissue less prone to be affected by the nature and amount of the preconditioning load (Zemánek, Burša, & Děták, 2009).

All sclera shell have been tested adopting the same preconditioning loads while the tissue was kept at constant room temperature and fully immersed in the PBS solution to maintain the hydration constant (Belkoff & Haut, 2008). Adopting the same testing procedure for all the tested eyes should allow to reduce the incidence of the variables affecting the load history of the tissue. Furthermore, the analysis of the sclera stiffness will consist in a comparative study of how stiffness relates to age and ethnicity. Because of the comparative analysis of the obtained results, a systematic error occurring for load history miss considerations will barely affect the consistency of the results.

The adopted interferometric technique allows to track displacement magnitude of several hundreds of nanometers. As described in chapter 2, the used interferometric technique consists of comparing two speckle fields generated respectively by an undeformed surface configuration taken as reference, and by a deformed surface configuration. Differences between these two speckle fields cannot be too high or the technique fails to track the deformation of the observed surface due to the speckle decorrelation and to avoid having fringe centers to close to each other, condition that would make failing the unwrapping procedure (later described).

To avoid these two mentioned issues the magnitude of the pressure steps used to test the eyes in the pressure range variation from 5 to 45 *mmHg* have been of about 0.1 - 0.4 *mmHg.*

The pressure step magnitude increase was automatically managed by the main control unit of the customized charging system in a way to account for the stiffening that sclera experiences when the internal pressure is risen from the baseline to 45 *mmHg*.

3.6. Geometric Properties Reconstruction

After loading the specimen with a pressure controlled hydraulic load, and performing the inflation test procedure described above, the saline chamber has been removed to allow the measurement of the outer surface of the posterior pole of the eye. Hydration of the sclera was now only provided by the saline inside the hemisphere. Saline was kept at a constant pressure level of 15 *mmHg*. Even if the hydration rate provided by the only liquid inside the eye was sufficient to avoid visible degradation of the biological tissue, geometry recording was performed the fastest possible to preserve any mechanical characteristic can be altered by changes in the hydration rate.

A three-dimensional mechanical digitizer (Figure 17) (MicroScribe G2X, Immersion) was used to collect a cloud of several thousand of points belonging to the outer surface of the sclera.

The recorded cloud of points was later fitted by using an interpolation method in a way to obtain a continuous function over the region of the eye describing the shape of the sclera shell. Continuity and derivability of this fitting function allows one to compute directions of the normal vectors of the surface. Normal vector information can be used to evaluate rotations of the deformed surface that are directly related to bending stress components present in the deformed surface.

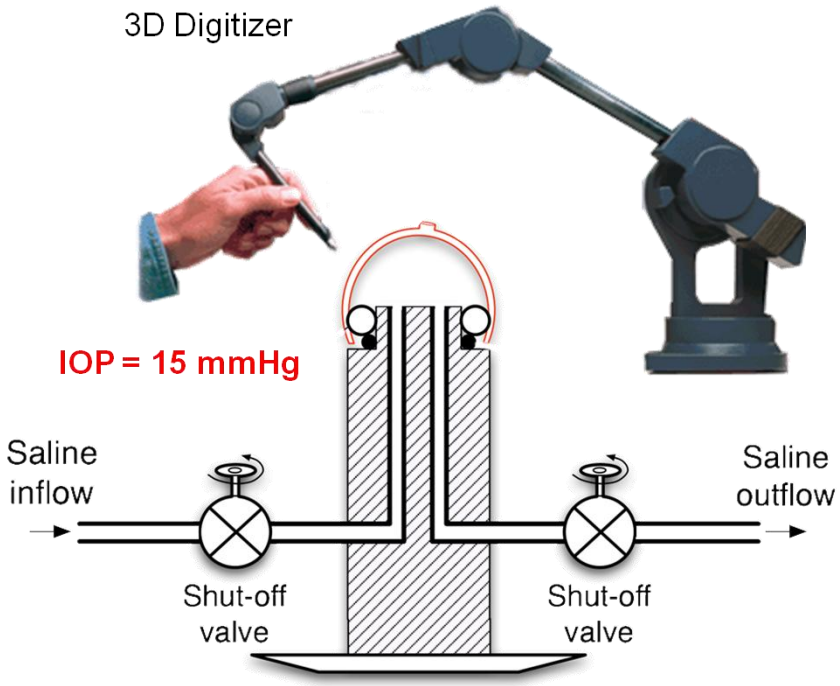

Figure 17. 3D mechanical digitizer for recording the eye shape; in this step of the procedure pressure level inside the hemisphere was of 15 *mmHg.*

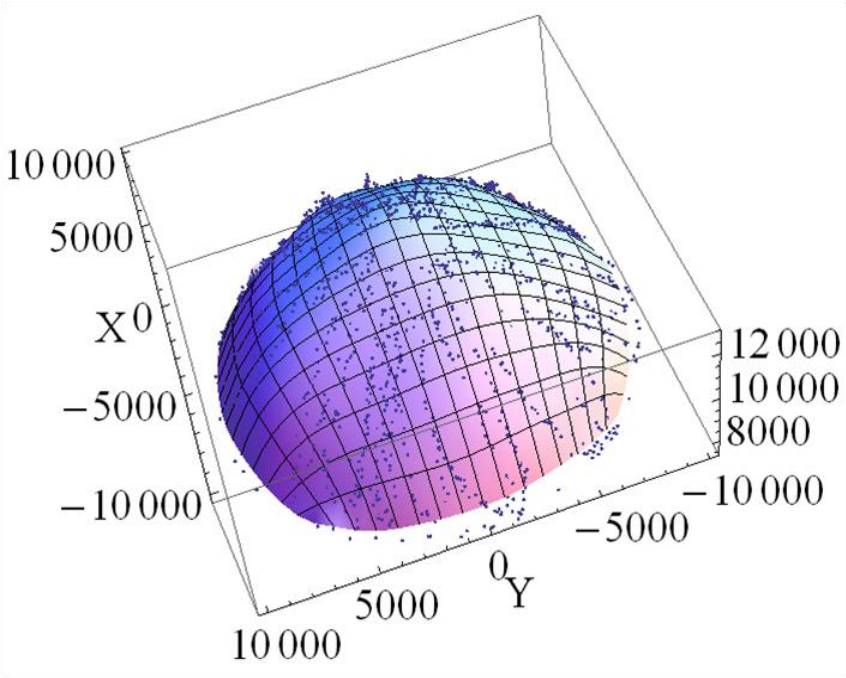

Figure 18. Points cloud fitted by B-spline based functions. Shape of the eye was described by a continuous function over the region of the shell.

As mentioned, the pressure level is kept constant through this measurement at 15 *mmHg.*

Usual values of deformation magnitude experienced in the inflation test are of some hundreds of microns for a pressure variation of 40 *mmHg*. Considering this, we can reasonably assume that geometry at 15 *mmHg* is similar to the geometry of the eye at 5 *mmHg*, so this value is assumed as reference in the displacement measurement. Keeping the eye at 15 *mmHg* in this part of the procedure increased the accuracy of the measurement because a slightly stiffer sclera than at 5 *mmHg* didn't allow the tip of the digitizer arm to deform the shape while this was touching the surface to record the cloud of points.

To have a complete description of the 3 dimensional structure of the posterior pole of the sclera it would be required the measurement of the inner surface as well.

As already mentioned, scleral tissue needed to be slightly internally pressurized to keep the 3 dimensional physiological shape. Because it was not possible to unclamp and to make reachable by the digitizer the inner surface, it has been adopted a method providing a valid approximation of the inner surface shape.

A 20 MHz ultrasound transducer (PacScan 300P, Sonomed, inc) combined with a 75 MHz pulser-receiver (5073PR, Olympus NDT, inc.) and a 200 MHz digital oscilloscope (TDS2022, Tektronix) have been adopted to measure the thickness value on 20 different location points as shown in Figure 19.a.

To perform the measurement with the ultrasound oscilloscope the saline kept in the inner of the eye had to be removed in a way to get a strong acoustic reflection when the acoustic wave generated by the ultrasound hit the interface between the inner surface of the sclera and the air present inside the eye. In this part of the procedure the eye has been pressurized with air at a pressure level of 30 *mmHg*.

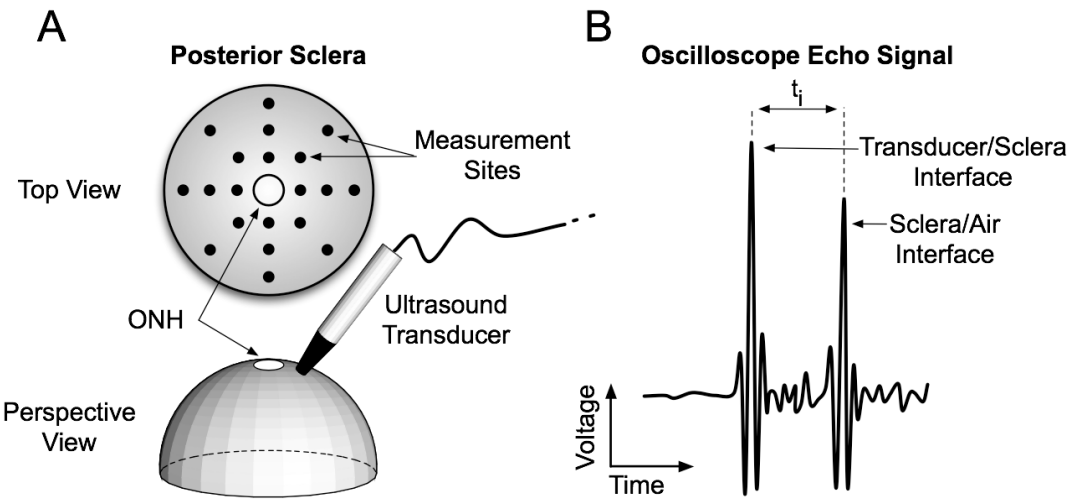

Figure 19.a. Location points for thickness measurement by ultrasound transducer device.
Figure 19.b. Example of oscilloscope signal. Picks made by the ultrasound wave reflection at sclera air-sclera and sclera-air interfaces.

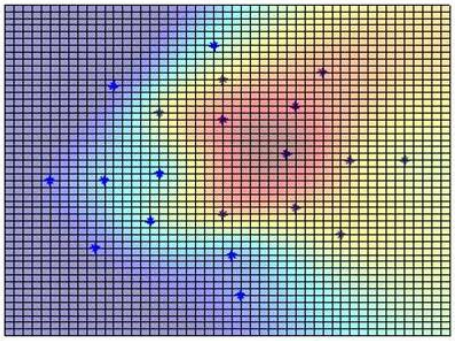

Figure 20. Thickness map defined by interpolating the 20 measured thickness values. Color codes represent low thickness values in blue, and high thickness value in red.

Finally, by interpolating the thickness value at these 20 different points (Figure 20), it has been possible to approximately reconstruct the shape of the inner surface of the tested eye.

CHAPTER 4

Interferometric Data Analysis

4.1. The Recorded Data

Performing the inflation test for the pressure range variation of 40 *mmHg* using pressure steps increments of 0.1 - 0.4 *mmHg* implies the storage and analysis of several hundreds of speckle fields carrying the information on the observed surface deformation.

The commercial adopted interferometer recorded four speckle fields per pressure step. This interferometer has been designed to work in conditions significantly different from the working condition in which the inflation test has to be performed.

In fact, the interferometer has been designed to record the deformation of 3 dimensional objects not supposed to be immersed in water, as the case considered in this work.

While the interferometer is able to track a 3D deformation field, the distance between the observed object and the observing CCD is supposed to be wide enough to allow some simplifying assumption in the data processing.

In the present set-up both the conditions are violated, since the spherical shape of the eye makes the tip of the outer surface too close to the laser beam sources and to the CCD of the ESPI, invalidating some simplifying assumptions usually considered in the most common testing set-up adopted in holographic interferometry.

To properly manage the analysis of the raw speckle fields recorded by the ESPI sensor, the analysis software of the ESPI had to be replaced by a customized software procedure reconstructing the 3D deformation field starting from the raw data recorded by the sensor.

The file type adopted by the ESPI analysis software is factory customized.

The first step for managing the raw data information has been to find the decoding procedure to extract the information needed for performing a customized analysis of the raw data.

A customized tool has been developed to export phase maps information stored in the mentioned files into a graphic format suitable to be imported and analyzed in *Mathematica*^{TM} .

An example of a phase map image is reported in the Figure 21.

The grayscale image contains the information relatively to the phase increment of the deformed region observed by each single pixel.

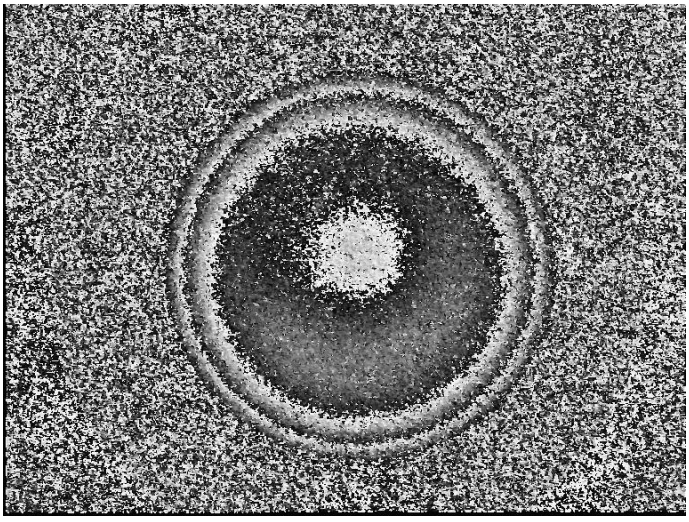

Figure 21. Phase map from one laser direction recording.

As mentioned before, speckle is a random distribution of laser light intensity in the space. When two speckle fields are “subtracted” before and after the observed object is deformed it can be seen a random distribution of black and white spots in the region of the image representing a part of the observed object that doesn’t experience any deformation. This behavior is explained by the fact that the light intensity “subtraction” of two random distributions of light intensities produces a random distribution of the phase values.

In the region of the image representing the deforming body it is possible to see that the grayscale distribution assumes a not random pattern.

Here the grayscale value of each pixel is proportional to the scalar product between the deformation vectors and the sensitivity vectors of the interferometer (eq. 5).

The adopted interferometer had 4 lasers symmetrically disposed around the viewing direction of the CCD sensor. With this optical configuration four different phase maps are recorded per step of load.

To reconstruct the displacement vector for each pixel of the phase map matrixes has to be performed a procedure of “unwrapping” on the recorded data.

4.2. The Problem of the Wrapped Phase

Data recorded by the interferometer cannot be directly used to reconstruct the deformation field of the observed object.

The grayscale value of each pixel is directly related to the phase change that the speckle field undergoes when the observed surface deforms.

The problem of the deformation field reconstruction form the phase values arises from an intrinsic feature of the phase that is its periodicity.

Let’s consider to plot in the upper side of the Figure 22 (above) a reasonable hypothetic out-of-plane displacement component for the points laying on a line parallel to the horizontal axis (*x*) and passing through the middle of the tested balloon shown in the Figure 21.

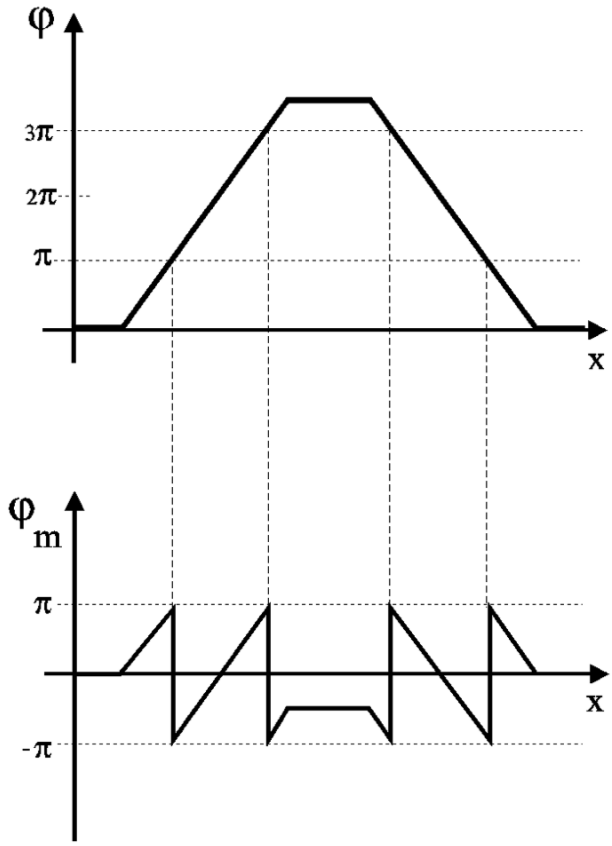

Figure 22.above. Schematic representation of the absolute phase value trend.

Figure 22.belove. Corresponding wrapped phase value diagram.

What we would see in the Figure 22.above is that the Z-component displacement of these points increases by moving from the border to the center of the balloon. The displacement is proportional to the absolute phase change recorded for these points.

In the lower part of the figure we can see the values that we would actually read in the phase map image at the position corresponding to the considered line.

The phase recorded cycles form $-\pi$ to π because of its periodicity. If we would read the phase value of the point at the center of the eye we could not relate this value to the displacement magnitude since the information about the absolute phase change of these points is lost because of the periodicity of the phase variation.

The phase maps are so called “wrapped”, since the value of the phase is constrained between the two bounds values it can assume that is $-\pi$ and π.

Absolute phase value =

$$= (\textit{wrapped phase value}) + \mathbf{2}\,\boldsymbol{\pi} * \textit{constant} \qquad \text{(eq. 19)}$$

Several algorithms have been built to reach the aim of reconstructing the absolute phase values of a two dimensional arrays.

In this work it has been used a customized unwrapping procedure and the strategy to unwrap the phase matrix has been based on the strategy developed by Flynn (Flynn, 1997).

An unwrapped phase matrix has the form like the one shown in the Figure 23. The values in the figure represent the phase values expressed in phase cycles (1 cycles = 2 π).

Let’s attempt to reconstruct the absolute phase value by reading the first row of the sub-matrix. The values of this row don’t present any phase-jump or discontinuities. By reading the firs column of the sub-matrix a phase jump can be seen at the 2nd row. Here the algorithm proceeds by performing iteratively an Elementary Operation (EO) that consists in adding a π modulus to a whole path of continuous values bounded by multiple line segments. The number of line segments represents how many π moduli should be add to the single value of the path to make this single phase value coherent with the neighboring points found in the direction shown by the direction marker. These markers show the direction where discontinuity with a higher value of cycles has been found.

Figure 23. Initial unwrapped phase with marked discontinuities. The numbers represent the unwrapped phase value per pixel in term of cycles. The line segments indicate the location and the magnitude of the discontinuities. The direction marker on each segment points toward the higher unwrapped phase. The sum of the discontinuity is 11.
(figure and captions are taken from *Two-dimensional phase unwrapping with minimum weighted discontinuity*- (Flynn, 1997)).

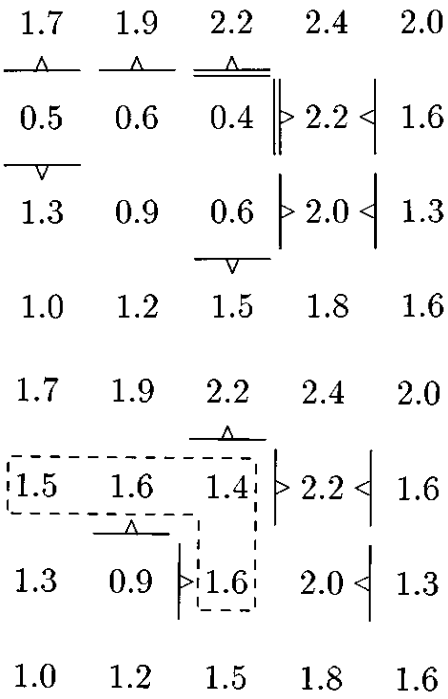

Figure 24. Result of performing an elementary operation (EO) on the unwrapped phase of Fig. 19. The phase values within the dashed contour have been increased of 1 cycle. The discontinuity markers reflect the changed phases. The discontinuity sum has been reduced to 6.
(figure and captions are taken from *Two-dimensional phase unwrapping with minimum weighted discontinuity*- (Flynn, 1997)).

After performing this operation (EO) of adding a π modulus to the bounded path, phase-jumps are recalculated and new discontinuities are highlighted as shown in Figure 24.

The algorithm iteratively proceeds by performing an addition of π moduli to paths of the phase value matrix (until the minimum number of discontinuities is reached, and no more EO can be performed.

In Figure 25 is shown a wrapped phase map and the resulting unwrapped phase map for an experimental test performed on a human eye.

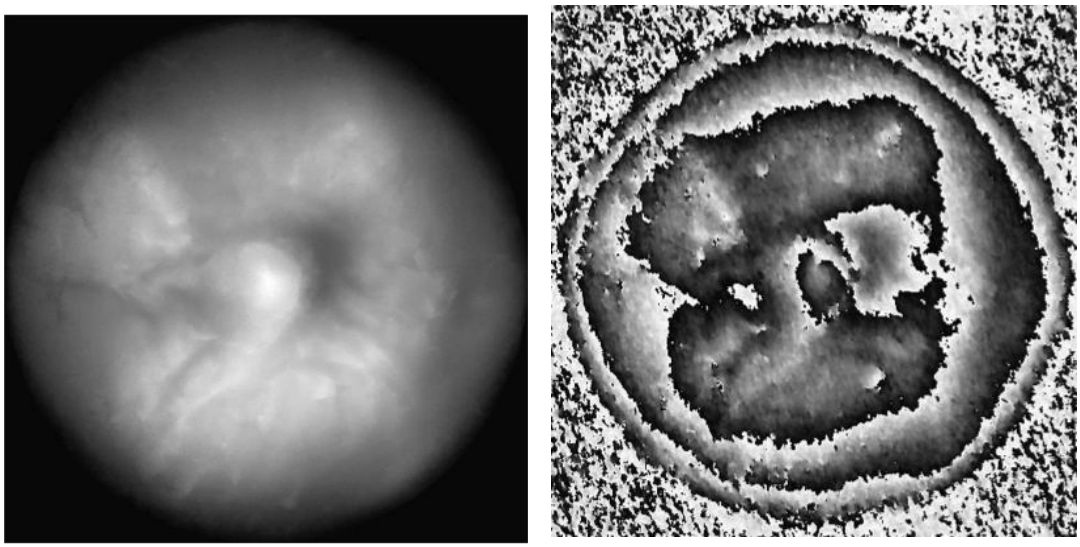

Figure 25 (left). Wrapped phase map from a testes human eye. (right) Corresponding unwrapped phase map.

4.3. Reconstruction of the Displacement Field

After performing the unwrapping procedure on each of the phase maps recorded per pressure step during the inflation test, the deformation field can be now reconstructed.

The unwrapped phase maps represent the absolute phase variation of the speckle field generated by the region imaged in the pixel before and after a pressure step increment.

Let's consider the same generic $\mathrm{pixel}(i,j)$ in all the 4 images created per pressure step, each of the 4 grayscale values of the 4 pixels is proportional to the scalar product between the displacement vector $\{d_x, d_y, d_z\}$ of the point of the surface that the $\mathrm{pixel}(i,j)$ observes and the sensitivity vector of the lasers ($\widetilde{\boldsymbol{K1}}$, $\widetilde{\boldsymbol{K2}}$, $\widetilde{\boldsymbol{K3}}$, $\widetilde{\boldsymbol{K4}}$) (as graphically simplistically represented in Figure 26).

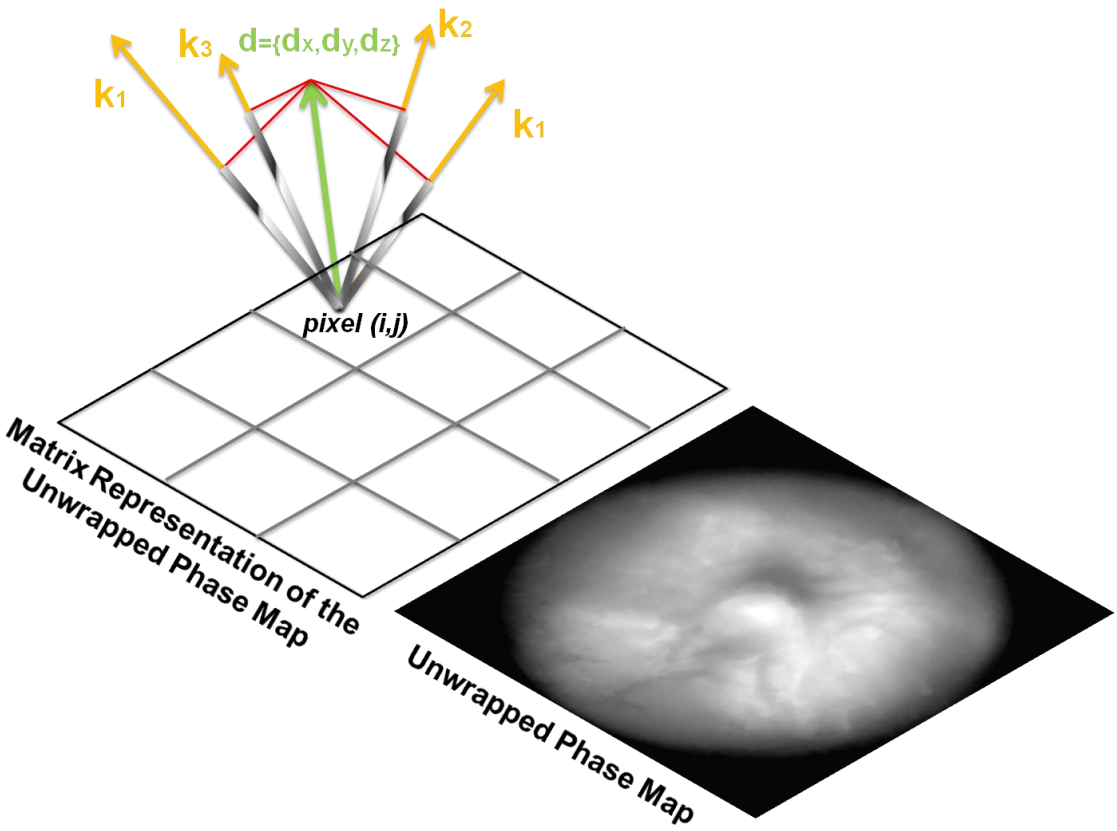

Figure 26. Graphical representation the projection of the displacement vector along the 4 sensitivity vectors of the ESPI.

Following equations show how is computed the displacement vector ($\widetilde{\boldsymbol{d}}$) of a point-region represented by the $\mathrm{pixel}(i,j)$.

$\widetilde{\boldsymbol{K1}}$, $\widetilde{\boldsymbol{K2}}$, $\widetilde{\boldsymbol{K3}}$, $\widetilde{\boldsymbol{K4}}$ are the 4 sensitivity vectors of the ESPI in the point of the region that the $\mathrm{pixel}(i,j)$ observes.

Let's here name the pixel-value of each of the 4 images considered ($\mathrm{PhV1}$, $\mathrm{PhV2}$, $\mathrm{PhV3}$, $\mathrm{PhV4}$).

We have that

$$\begin{cases} \tilde{d}.\widetilde{K_1} = \dfrac{2\pi}{255}\,\mathrm{PhV1} \\ \tilde{d}.\widetilde{K_2} = \dfrac{2\pi}{255}\,\mathrm{PhV2} \\ \tilde{d}.\widetilde{K_3} = \dfrac{2\pi}{255}\,\mathrm{PhV3} \\ \tilde{d}.\widetilde{K_4} = \dfrac{2\pi}{255}\,\mathrm{PhV4} \end{cases} = \begin{cases} d_x K_{1x} + d_y K_{1y} + d_z K_{1z} = \mathrm{PhV1} \\ d_x K_{2x} + d_y K_{2y} + d_z K_{2z} = \mathrm{PhV1} \\ d_x K_{3x} + d_y K_{3y} + d_z K_{3z} = \mathrm{PhV1} \\ d_x K_{4x} + d_y K_{4y} + d_z K_{4z} = \mathrm{PhV1} \end{cases}$$

(eq. 20)

$$\begin{pmatrix} K_{1x} & K_{1y} & K_{1z} \\ K_{2x} & K_{2y} & K_{2z} \\ K_{3x} & K_{3y} & K_{3z} \\ K_{4x} & K_{4y} & K_{3z} \end{pmatrix} \begin{Bmatrix} d_x \\ d_y \\ d_z \end{Bmatrix} = \frac{2\pi}{255} \begin{Bmatrix} \mathrm{PhV1} \\ \mathrm{PhV2} \\ \mathrm{PhV3} \\ \mathrm{PhV4} \end{Bmatrix}$$

(eq. 21)

assuming

$$\tilde{K} = \begin{pmatrix} K_{1x} & K_{1y} & K_{1z} \\ K_{2x} & K_{2y} & K_{2z} \\ K_{3x} & K_{3y} & K_{3z} \\ K_{4x} & K_{4y} & K_{3z} \end{pmatrix} \quad \mathbf{GS} = \begin{Bmatrix} \mathrm{PhV1} \\ \mathrm{PhV2} \\ \mathrm{PhV3} \\ \mathrm{PhV4} \end{Bmatrix} \quad \tilde{d} = \begin{Bmatrix} d_x \\ d_y \\ d_z \end{Bmatrix}$$

(eq. 22)

We obtain that the displacement vector of the point observed by the $\mathrm{pixel}(i,j)$ is

$$\tilde{d} = \frac{2\pi}{255}\,\mathbf{GS}\,\tilde{K}^{-1}$$

(eq. 23)

A customized routine written in *Mathematica*^{TM} performed the computing of the displacement vectors of the ESPI data.

In this work the displacement field has been computed only at certain pressure level. It has been computed the deformation the eye experienced during the inflation test at the pressure level of 7, 10, 15, 20, 25, 30, 35, 40,

45 *mmHg*. The baseline pressure level it has been always considered at 5 *mmHg*.

Figure 27 shows the displacement field reconstruction for a human eye at a pressure level of 7 *mmHg.* The displacement field is represented in 3 components of a Cartesian system d_x, d_y, and d_z.

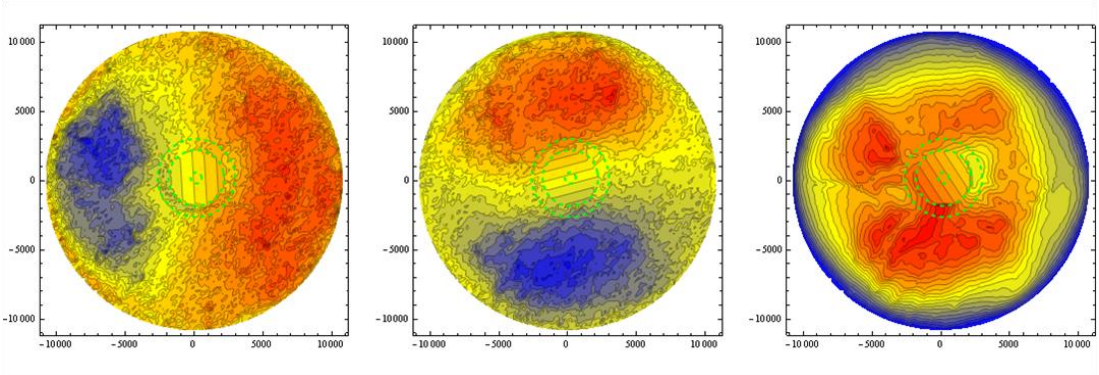

Figure 27. Displacement maps (d_x, d_y, d_z) computed from unwrapped phase maps for of a human eye pressurized at 7 *mmHg*.

In Figure 27 the two dashed circles drawn in all the displacement components are a graphical representation of a filtering procedure adopted to skip in the displacement fields reconstruction the region of the ONH. In fact, after cutting away the optic nerve from the sclera the chunk left of the nerve creates a noised region where the unwrapping algorithm would find several discontinuities that would reduce the quality of the absolute phase reconstruction.

The filter was formulated to linearly interpolate in 3 dimensions the deformation values of the points laying between the outer and inner green circles. The deformation points inside the inner circle are those substituted by the filter.

4.4. B-spline Based Fitting Method

After performing the unwrapping procedure it is required an operation of filtering or fitting because it is not possible to achieve a pattern of deformation without small local fluctuations of the unwrapped phase value, mainly due to electronic noise and partial decorrelation. Therefore, to avoid fluctuation (Figure 28) and discontinuities in the deformation field it has to be performed an operation of filtering to reduce these discontinuities, or of fitting to completely eliminate them.

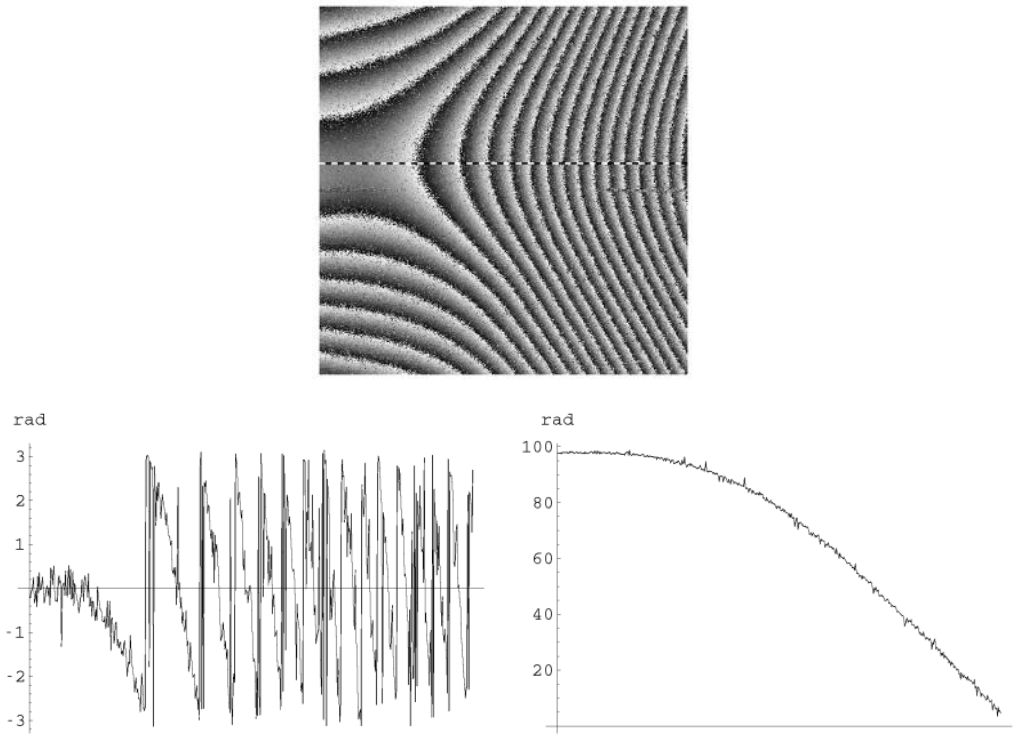

Figure 28. Wrapped phase map of a generic deformed surface (up). Fluctuating values of the wrapped phase map (left) and of the unwrapped phase (right). In both of the lower diagrams are clearly visible the irregular trend of the wrapped and unwrapped phase.

As mentioned, the experimental data obtained by the interferometer consists of four phase maps for each load step. A typical set of experimental data is reported in Figure 29, which represent the four displacement components along the corresponding sensitivity vectors.

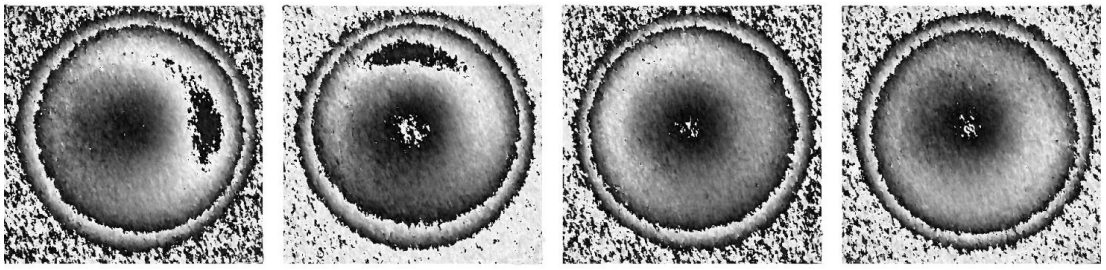

Figure 29. Phase maps for a single load step.

After the unwrapping of the phase maps a fitting procedure was applied to the experimental data in order to obtain a smooth distribution of the phase values over the observed domain. Moreover, it allows to drastically reduce the use of filtering procedures commonly applied in random-noise affected data (i.e. the speckle noise).

The most used filter in random noise-affected data is a linear filter (also known as a *median filter*). Linear filters are able to remove significant noise in the data, but data that deviates from a linear distribution are heavily distorted by this filtering procedure.

Phase maps like those reported in Figure 29 have an intrinsic sinusoidal distribution of the phase value, a feature that makes the use of a linear filter unsuitable. Furthermore, the wrapped nature of the phase makes the distribution of its value widely discontinuous, as shown in Figure 22.below, making a linear filter procedure heavily distorting the raw data.

The approach used in this customized data-fitting procedure is similar to the one proposed in (Bruno L. , 2007) where a set of B-spline based functions are linearly combined with the aim of obtaining an analytical model representing the fitted quantities. The model reported in (Bruno L. , 2007) is directly applicable to a rectangular domain and it works in a rectangular reference system. In the analysis of the posterior sclera shell deformation of the domain of the investigated region is circular, because of that the adoption of a polar coordinate system to perform the fitting procedure is an expectable choice.

In this case the B-spline functions were used only for modeling the variation along the radial coordinate, while in the circumferential direction sinusoidal functions were adopted. The overall number of functions to be linearly combined was equal to the control points chosen along the radius multiplied by the number of sinusoidal functions used for fitting the data along the circumferential direction.

Figure 30 reports the shape of cubic polynomials that define the functions along the radial direction. These functions were defined such that they assume zero value in correspondence of the maximum radius of the region of interest. This assumption is consistent with the loading configurations of the investigated tissues, which are clamped at the outer radius by the charging apparatus described in chapter 3 (Figure 13). The order of the polynomials reported in Figure 30 is that used in the fitting procedure of experimental data analyzed in the present work.

In the circumferential direction *l* integer harmonics were used consisting of a sin and a cos term for each harmonic plus the constant term, for a total of *2l*+1 terms.

Hence the generic overall fitting function for *n* control points along the radial coordinates and for *l* integer harmonics along the circumferential direction assumes the following form:

$$\begin{aligned} F(r,\theta) = {} & w_1 N_1(r) + \cdots + w_n N_n(r) + \\ & + [w_{n+1} N_1(r) + \cdots + w_{2n} N_n(r)]\cos\theta + [w_{2n+1} N_1(r) + \cdots + w_{3n} N_n(r)]\sin\theta + \cdots + \\ & + [w_{n(2l-1)+1} N_1(r) + \cdots + w_{n(2l-1)+n} N_n(r)]\cos k\theta + [w_{n(2l)+1} N_1(r) + \cdots + w_{n(2l)+n} N_n(r)]\sin l\theta \end{aligned}$$

(eq. 24)

where w_i are the $n(2l+1)$ weights to be evaluated by an optimization procedure based on least square method.

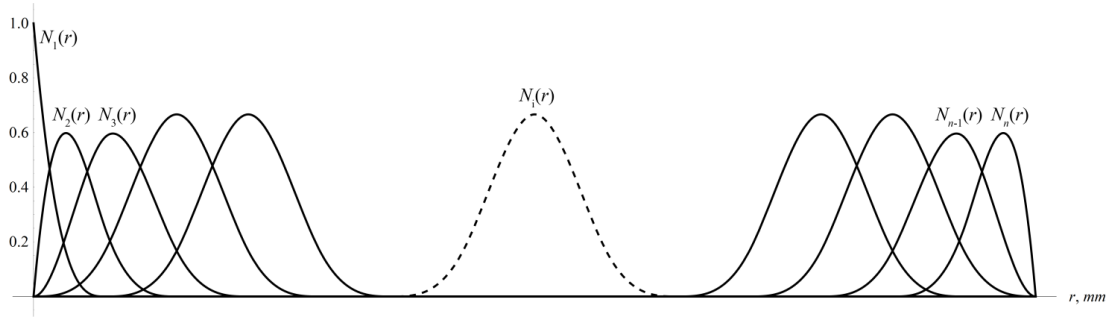

Figure 30. Cubic functions defined in the radial direction.

After the computation of the pseudo-inverse of the matrix whose elements are the values that the functions (that have to be linearly combined) assume at each experimental point vale; the weights w_i are estimated by multiplying this new matrix (pseudo-inverse) by the experimental data values. Thus, if *m* experimental data are available, the matrix whose pseudo-inverse must be evaluated assumes the following form:

$$\begin{bmatrix} N_1(r_1) & \cdots & N_n(r_1) & N_1(r_1)\cos\theta_1 & \cdots & N_n(r_1)\cos\theta_1 & N_1(r_1)\sin\theta_1 & \cdots & N_n(r_1)\sin\theta_1 & \cdots\cdots & N_1(r_1)\cos k\theta_1 & \cdots & N_n(r_1)\cos k\theta_1 & N_1(r_1)\sin k\theta_1 & \cdots & N_n(r_1)\sin k\theta_1 \\ \vdots & & \vdots & \vdots & & \vdots & \vdots & & \vdots & & \vdots & & \vdots & \vdots & & \vdots \\ N_1(r_m) & \cdots & N_n(r_m) & N_1(r_m)\cos\theta_m & \cdots & N_n(r_m)\cos\theta_m & N_1(r_m)\sin\theta_m & \cdots & N_n(r_m)\sin\theta_m & \cdots\cdots & N_1(r_m)\cos k\theta_m & \cdots & N_n(r_m)\cos k\theta_m & N_1(r_m)\sin k\theta_m & \cdots & N_n(r_m)\sin k\theta_m \end{bmatrix}$$

(eq. 25)

where (r_i) are the coordinates of the i-*th* point at which the experimental datum is retrieved.

It must be noticed that a reliable optimization requires that the number of experimental data is much greater than the number of the parameters to be estimated. In the method proposed in the present work it has been chosen *n*=6 and *k*=4, hence the overall fitting function is formed by 54 terms, while the phase maps to be fitted are about 400x400 pixel-values.

4.5. Numerical Analysis - Introduction

As mentioned above, the major aim of the work is to perform an inverse finite element procedure to estimate a set of material properties that best describe the biomechanics of the human sclera.

In the design of an engineered structure, the designer knows the material properties, shape, geometric properties, and the external loads, but the deformation field is unknown and must be determined by mechanical modeling of the structure.

In this case, an inverse engineering procedure is adopted when the material properties, or the shape, or the geometrical properties is an unknown variable in the design of the structure.

In the analysis of the sclera biomechanics performed in this work, the geometric properties and the shape are known by the data collected by ultrasound transducer (thickness), and by the mechanical 3D digitizer (shape). The deformation field of the structure (posterior scleral shell) is the outcome of the analysis made on the interferometric data. The load history is known as well, since it is imposed and recorded during the inflation test procedure.

By coupling geometric properties, shape, loads, and boundary condition information, it is possible to implement a FEM model describing the real eye-specific structural features of each posterior sclera shells.

The only missing information is the material properties. To determine the material properties of each scleral shell, a customized genetic algorithm was used to find a set of material properties best fitting the experimental displacement field recorded in the inflation test.

4.6. Numerical Analysis - FEM Model Implementation

For each tested eye an individual specific model has been implemented.

The shape information of the outer surface obtained by fitting the point cloud recorded by the mechanical digitizer coupled with the thickness map obtained by fitting the thickness values sampled in 20 measurement points by using the ultrasound transducer made possible to reconstruct the 3D geometry of the tested eye. A routine made in *Matlab*^{TM} has been used and adapted to create a FE mesh starting from the geometrical information available.

The element type used has been 8-noded hexahedral.

A convergence test was performed to assess the numerical accuracy of the FE approximation by increasing the number of nodes. This task was performed by the *Matlab*^{TM} routine by increasing the node density along the meridional, circumferential and transmural directions of the sclera. Node density and distribution was controlled by several parameter defining (Figure 31.right):

- The numbers of element to be used in the transmural direction (npt).
- The numbers of element along the meridional direction of the sclera (np12).
- The number of elements to be used for modeling the only peripheral sclera along the meridional direction (nelb).
- The number of elements along the circumferential direction (np34).

From information gathered by the mechanical digitizer was retrieved the position of the ON region. This region has been meshed with the same element used for the sclera shell region, but a different constitutive material model was adopted for the elements belonging to the ONH region.

Adequate numerical accuracy was achieved with 5091 nodes and 3328 elements (Figure 31.left).

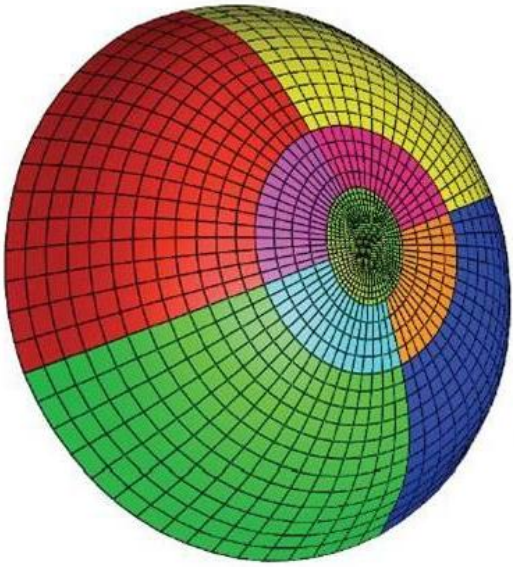

Figure 31.left. Individual specific FE mesh.

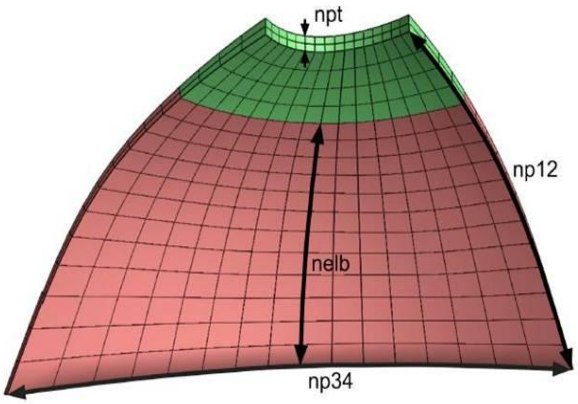

Figure 31.rigth. Partial view of the FE mesh highlighting the control parameters of the mesh topography.

Load pressure data recorded by the central unit connected to the digital manometer has been used to assess the nodal load conditions.

Displacement of the nodes belonging to the region where the tissues was clamped to the steel ring (Figure 14) have been forced to zero.

After creating the mesh structure the *Matlab*^{TM} routine automatically created the input file for the numerical FE solver.

In this part of the analysis the adopted solver was *Nike3D*^{TM}, a fully implicit, three-dimensional finite element solver code particularly suitable for analyzing the finite static and dynamic strain response of inelastic solids, shells, and beams (Lawrence Livermore National Laboratory, 2010).

4.7. Numerical Analysis - Material Properties

The material constitutive model adopted in this work has been extensively described in a previous work carried by some coworkers aiming to built a constitutive model enclosing the most of the features of the sclera (Girard, Downs, & Burgoyne, 2009).

The main properties of the material model are here briefly described:

Strain energy function was expressed as a nonlinear function of the fourth invariant of deformation I_4 (Spencer, 1985) defined as

$$I_4 = \boldsymbol{a_0}.\boldsymbol{C}.\boldsymbol{a_0} \qquad \text{(eq. 26)}$$

where $\boldsymbol{a_0}$ is a unit vector representing the local fiber direction in the undeformed configuration, and $\boldsymbol{C}$ is the right Cauchy-Green deformation tensor; relationship between I_4 and the fiber stretch λ can be expressed as

$$\lambda\, \boldsymbol{a} = \boldsymbol{F}.\boldsymbol{a_0} \qquad \text{(eq. 27)}$$

where $\boldsymbol{a}$ is a unit vector representing the local fiber direction in the deformed configuration, and $\boldsymbol{F}$ is the deformation gradient tensor. Since $\boldsymbol{C} = \boldsymbol{F}.\boldsymbol{T}.\boldsymbol{F}$, the fourth invariant I_4 is equivalent to the squared fiber stretch

$$I_4 = \boldsymbol{a_0}.\boldsymbol{C}.\boldsymbol{a_0} = \boldsymbol{a_0}.\boldsymbol{F}.\boldsymbol{T}.\boldsymbol{F}.\boldsymbol{a_0} = \lambda^2 \qquad \text{(eq. 28)}$$

For many soft-tissues, the collagen fiber alignment is multi-directional at local material points (Driessen, Bouten, & Baaijens, 2005) (Pinsky, Dolf, & Dimitri, 2005) instead of being unidirectional. In the particular case of the posterior sclera the collagen fibers have a large variation in their diameters and are formed into irregularly arranged, multi-layered lamellae, with each lamella having different preferred fiber orientation and thickness (Greene, 1980)

(Komai & Ushiki, 1991) (Rada, Shelton, & Norton, 2006). To allow for multi-directionality at local material points, it is assumed that scleral collagen fiber alignment is confined within a plane tangent to the scleral surface, following a 2-D statistical distribution function (P) defined as

$$P = \frac{1}{\pi\, I_0\, k} \exp\left(k\, \cos(\theta - \theta_p)\right) \qquad \text{(eq. 29)}$$

known as the semi-circular Von-Mises distribution (Fisher, 1993) where I_0 is the modified Bessel function of the first kind (order 0), θ_p is the preferred fiber orientation relative to a local coordinate system, and k is the fiber concentration factor.

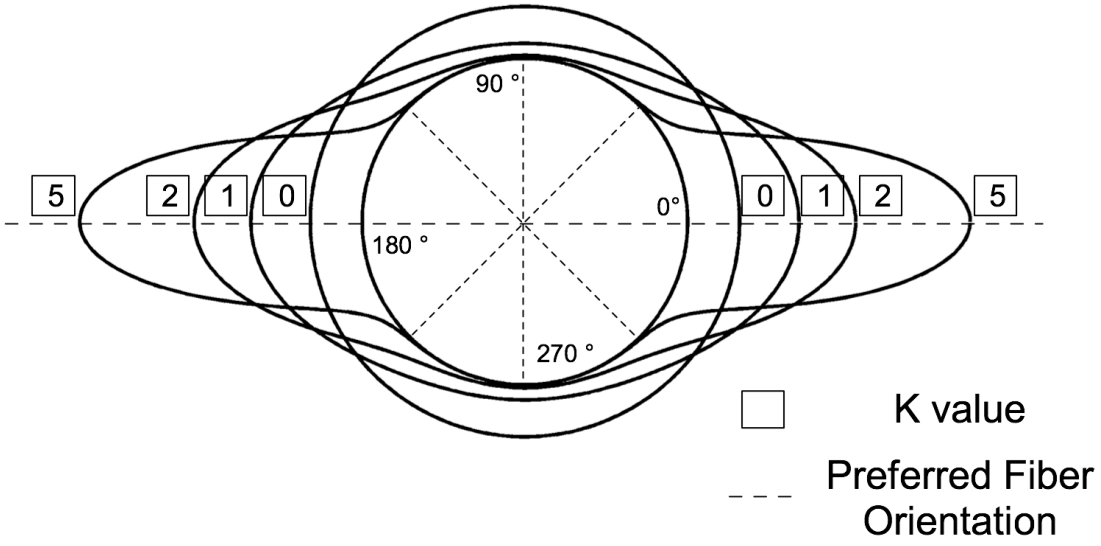

Figure 32. Semi-circular Von-Mises probability distribution of the preferred fiber orientation as a function of the *k* value.

Statistical distribution P was chosen for its capability of describing collagen fiber alignment with two only parameters (k, θ_p). When the fiber concentration factor k is equal to zero the collagen fibers assume an isotropic distribution in a plane tangent to the scleral wall. As k increases the collagen fibers align along the preferred fiber orientation θ (Figure 32).

A so formulated material constitutive model allows to account for large scale elastic anisotropic deformations.

Material constitutive model adopted in this work is based on the consideration described above.
The strain energy function considered in this work is derived eq. 18 and takes the form

$$W = C_1(I_1 - 3) + \frac{1}{2}K[\ln(\theta)]^2 + F(\lambda) \qquad \text{(eq. 30)}$$

Where in the right side of the equation the first member accounts only for the isotropic energetic contribution of the deformation, while the second and third members account for the transverse isotropy.
The isotropic part of the strain energy function is characterized by the Mooney-Rivlin coefficient C_1 and it is function of the first invariant of the deformation I_1; the anisotropic part is defined by the parameters k and θ, and it is function of the fiber stretch λ along the preferred fiber direction.
By considering eq. 30 we can express the additional contribution to Cauchy stress due to the fiber stretch as function of two parameters C_3 and C_4.

$$\frac{\partial F}{\partial \lambda} = C_3(\exp(C_4(\lambda - 1)) - 1) \qquad \text{(eq. 31)}$$

Here, C_3 scales the exponential stresses, while C_4 controls the uncrimping rate of the collagen fibers.

Finally we have that the material constitutive model adopted is function of

1. The first invariant of the deformation I_1.
2. The fiber stretch λ along the preferred fiber direction.

And it is characterized by 5 parameters

1. C_1: Mooney-Rivlin coefficient.

2. K: Fiber concentration factor.
3. θ: Preferred fiber orientation.
4. C_3: Scaling factor of the exponential stresses.
5. C_4: Parameter controlling the rate of uncrimping of the collagen fibers.

This material constitutive model was directly implemented by Michael Girard in the numerical solver *Nike3D*^{TM}.

Because of the non-homogeneities present through the whole sclera such as variable thickness, change of the preferred orientation, and density of the collage fibrils, it has been choose to define the material model with 5 parameters but it has been assumed a regionalization criteria for the assignment of the element properties of the mesh in a way that the elements belonging to the region close to the ONH (peripapillary sclera) and elements belonging to the region closer to the equator (peripheral sclera) were not defined by the same set of parameters describing the preferred fiber orientation θ and the fiber concentration factor k.

This approach arisen by the assumption that the fiber concentration and orientation in the peripheral sclera could be physiologically significantly different from those of the peripheral sclera.
In this way the algorithm used to assess the set of material properties had a higher flexibility for finding the best set of parameters minimizing the difference between the numerical and experimental displacement fields.

4.8. Numerical Analysis - Genetic Algorithm Optimization

Among the different strategies of optimization, genetic algorithm optimization has been choose for its capability to manage a relative wide set of parameters affecting the function describing the problem to be minimized (*fitness function*) (Price, Storn, & Lampinen, 2005) and for its searching method that is less prone than others direct search algorithm to fall in a local minimum of the solution space of the problem.

Genetic algorithm mimics the natural evolution. Individual selection is based on the evaluation of the fitness rate of the characteristic has to be fitted in the problem of each individual of the population.

The evolution usually starts from a randomly generated population. In each generation the fitness of every individual of the population is evaluated, multiple individuals are stochastically selected from the current population (based on their fitness rate), and modified (recombined and randomly mutated) to form a new population. The new population is then used in the next iteration of the algorithm. Commonly, the algorithm terminates when either a maximum number of generations has been produced, or a satisfactory fitness level has been reached. (Genetic algorithm, 2010-Genetic algorithm)

The most common operators used by a genetic algorithm are *mutation* and *crossover.*

Genetic operators define the strategy used to create a new population of individuals (offspring) starting from the old population of individuals (parents) of which the fitness rate of each individual has been evaluated (Hong, Wang, Lin, & Lee, 2002).

Briefly, *mutation* can be defined as an operator that creates a new individual by randomly modifying a parent individual of the population.

Crossover creates a new population of individuals by partially mixing some features of two (or more) parents.

Usually, both of the operators are simultaneously used on different individuals of the parents population. Figure 33 shows both operator applied to binary strings with a crossover probability of 50%.

Crossover probability defines how often will be crossover performed per iteration on the parents population.

If crossover probability is 100%, then all offspring are made by using crossover operator. If crossover probability is 0% all the new generation is made from exact copies of features taken by the old population.

Crossover is made in hope that new features will have good parts of the old features and maybe the new features will make new individuals having a better fitness rate. However, it is a good strategy to leave some parts of the population to survive to the next generation.

Mutation probability indicates how often will be parts of features mutated. If there is no mutation offspring is taken after crossover (or copied) without any change. If mutation is performed, a portion of the features is changed. If the mutation probability is 100%, all the features are changed, and if it is 0% none are changed.

Mutation is made to prevent falling GA into a local minimum; but mutation should not occur very often, or the GA will in fact change to random search.

The best rate of mutation and crossover usage is an extensively discussed topic (Schmitt, 2001), and a new developments on genetic algorithm strategy consists of dynamically change the appropriate rate of these two operators (Soung-Min & Ju-Jang, 2008).

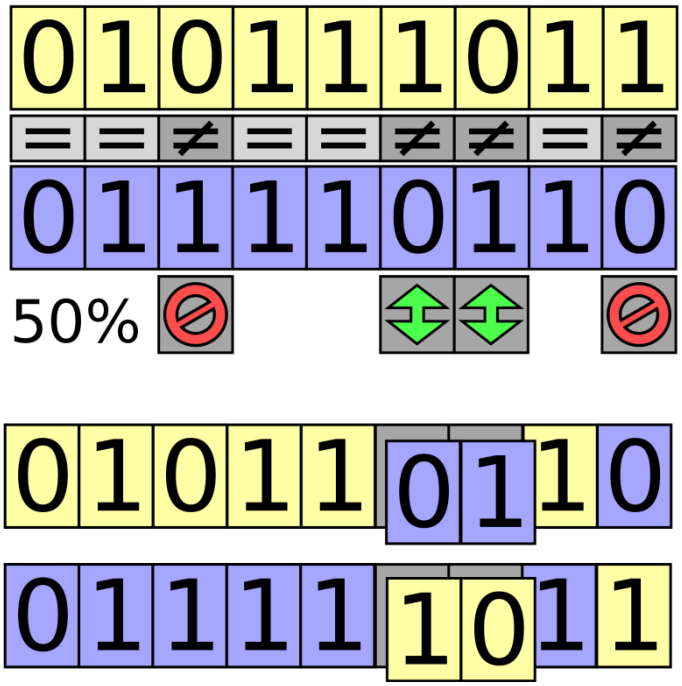

Figure 33. Genetic algorithm operators applied on binary strings at a rate of 50%. Four features are changed passing from old population to the new one. Two features are modified by crossover operation, and the remaining two by mutation.

4.9. Numerical Analysis - Genetic Algorithm Based Procedure

The aim of the FE implementation is to find a set of material properties that would produce the best matching between the numerical and the experimental displacement.

By purely guessing a set of material properties to be adopted in the individual specific FEM model, it would be possible to obtain and analyze the numerical displacement field of the implemented structure. The numerical displacement field obtained could be compared with the experimental displacement field recorded, and the differences between these two fields could be evaluated and analyzed.

The consistency of this strategy led the development of an algorithm whose purpose is to automatically create a series of automated operations structured as follows:

1. Creation of an initial guess of a set of material properties.
2. Embedding of the material properties set in the implemented FEM model.
3. Run of the numerical simulation of the model.
4. Evaluation of the obtained numerical displacement field .
5. Comparison of the numerical and experimental displacement fields.
6. Creation of a new set of material properties in an attempt to reduce the differences between the numerical and experimental displacement fields.
7. Looping steps 2 to 6 until a set of material properties is found that minimizes the differences between the two displacement fields.

Several customized routines written in *Fortran*^{TM} and *Perl*^{TM} have been implemented to perform the tasks described above.

The algorithm has been implemented to find a set of 13 parameters describing the mechanical behavior of the sclera. The regionalization criteria allowed the peripheral and the peripapillary sclera to assume two different values for the parameter defining the fiber concentration factor k.

Trying to represent the natural dispersion of the preferred fiber orientation that widely changes through the sclera, a set of 8 parameters were used to define the fiber orientation of all the elements of the sclera.

Four of these 8 parameters defined the fiber orientation of the elements belonging to the peripheral sclera region, and the 4 left defined the fiber orientation of the elements belonging to the peripapillary sclera region.

Local orientation that each element assumed as a function of the 4 parameters (for both the regions) has been defined as follows:

The set of 4 parameters defining the fiber orientation have been used as control points of a curvilinear interpolation system. Considering the sclera as a spherical oriented object, 4 parameters per region defined the local fiber orientation of the elements having the same azimuth angle of the control

points. All the elements having an azimuth included between the azimuth value of two control points assumed a fiber orientation interpolated between the fiber orientation value of the neighboring control points (Figure 34).

The final set of 13 parameters fit by the algorithm are (Figure 35):

- $C_{1,}$ $C_{3,}$ C_4 assigned to all the elements belonging to the sclera shell region.
- $K_{1,}$ K_2 assigned respectively to the peripheral and peripapillary sclera regions.
- θ_{p1}, θ_{p2}, θ_{p3}, θ_{p4} , assigned to the peripheral sclera, and θ_{p5}, θ_{p6}, θ_{p7}, θ_{p8} assigned to the peripapillary sclera.

At the elements belonging to the ONH region had an incompressible linear isotropic material property with an elastic modulus of 1 *MPa*.

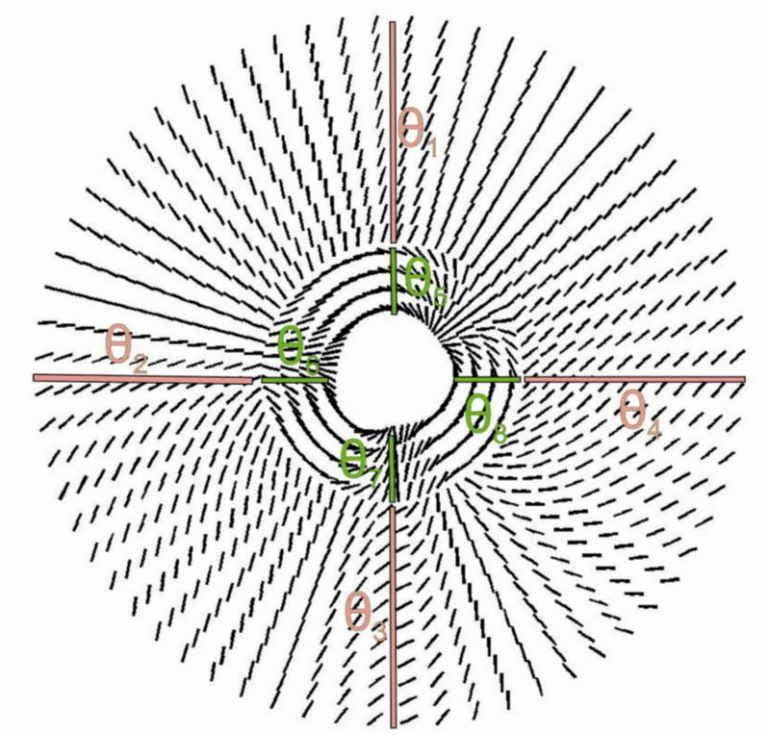

Figure 34. Preferred fiber orientation interpolation method.

A schematic representation of the tasks performed by the algorithm are represented in Figure 36.

The column on the left side of the Figure 36 describes the first iteration of the algorithm.

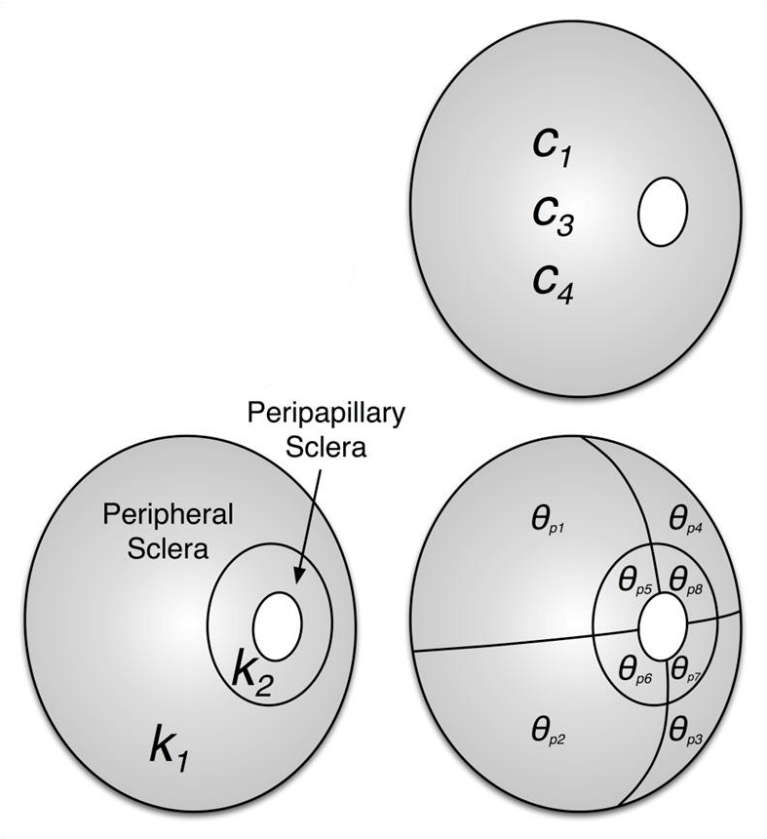

Figure 35. Regionalization criteria for the material properties of the elements of the mesh.

In this first step the genetic algorithm creates a population of 50 individuals whose set of parameters are randomly created. Each parameter is forced in the first iteration to assume a value between the lower and upper bound (Table 2).

	Lower bound	Upper bound
C_1	100000	1000000
C_3	1000	50000
C_4	300	1500
K_1	0	5
K_2	0	5
θ_{p1}	0	180
θ_{p2}	0	180
θ_{p3}	0	180
θ_{p4}	0	180
θ_{p5}	0	180
θ_{p6}	0	180
θ_{p7}	0	180
θ_{p8}	0	180

Table 2. Boundary values for each parameter in the first randomly created population.

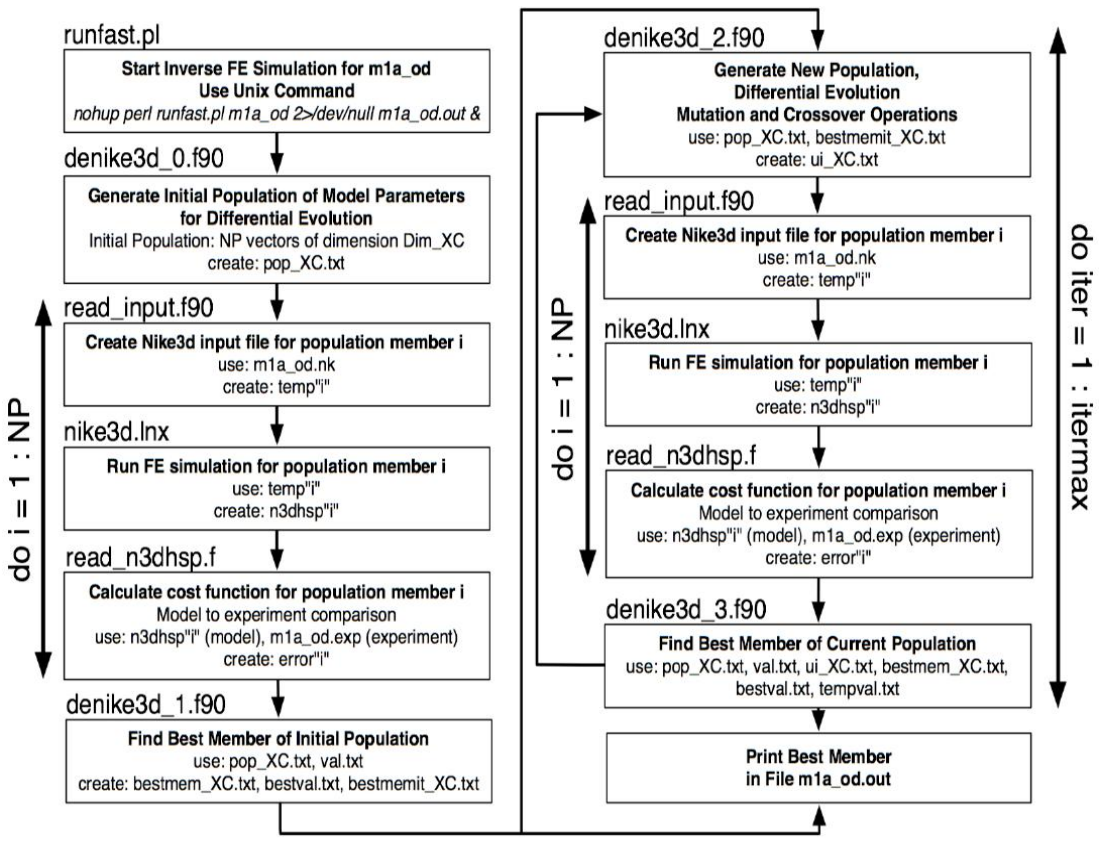

Figure 36. Flow chart representation of the tasks performer by the genetic algorithm.

Chapter 5

Experimental Results

5.1. Human Eyes Data Fitting

In this chapter are presented some preliminary results obtained by adopting the inverse engineering procedure carried out by using the genetic algorithm-based procedure previously described.

Displacement maps reconstruction from ESPI measurements have been analyzed in this instance by assuming some simplifying assumptions commonly adopted in speckle interferometry.

In particular, the direction of the sensitivity vectors of the ESPI system are considered not varying as a function of the tracked point belonging to the observed deforming surface. This implies that the wavefront generated by each of the four laser sources is assumed as a collimate laser beam (i.e. direction of the illuminating direction $\vec{K}_i$ is constant). Has mentioned in the paragraph 1.2, when a point on the observed surface experiences a deformation its displacement vector can be reconstructed by analyzing the phase value variation recorded by the interferometer. The displacement magnitude is related to the phase value by the mentioned relationship:

$$\phi = \frac{2\pi}{\lambda} \vec{d}.(\vec{K}_i - \vec{K}_o) = d_x K_x + d_y K_y + d_z K_z \qquad \text{(eq. 5)}$$

With $\vec{d}$ the displacement vector wanted to be reconstructed and $(\vec{K}_i - \vec{K}_o)$ the sensitivity vector of the interferometer.

As anticipated, in this instance the sensitivity vector $(\widetilde{K}_i - \widetilde{K}_o)$ direction is considered to be constant and independent to the position of the observed point. This is a common assumption that is considered in speckle interferometry since usually the observed surface is far enough from the CCD position (that defines the direction of observation $\widetilde{K}_o$) to allow considering the change in direction of the sensitivity vectors not impacting on the displacement vector reconstruction.

In the optical set-up used in this work the eyeball is not positioned far enough to considerer the sensitivity vector directions constant.

This miss consideration has been estimated in causing an error of a 3-5% on the deformation values for the out-of-plane component, and of a 15-35% on the in-plane components.

The genetic algorithm adopted to obtain the results shown in this section was designed to reduce the difference between the experimental and numerical displacement fields. Because the out-of-plane displacement magnitude is much more higher than the in-plane displacement magnitude (usually the out-of-plane displacement magnitude is three times higher than the in-plane), the cost function of the genetic algorithm was mainly driven by the out-of-plane displacement component.

Being the out-of-plane displacement components barely affected by the sensitivity vector direction change, the results shown in this section are not relevantly affected by the considered simplifying assumptions.

In the successive section these simplifying assumptions are not considered anymore, and it will be presented a compensation method that allows to discharge all the simplifying assumptions usually considered in the speckle interferometric data analysis considered in this section.

5.2. Preliminary Outcomes from Human Eyes Data Fitting – Testing Procedure

The testing procedure is briefly summarized here:

One eye was randomly selected from each of four normal human donors 75 to 82 years old and tested within 48 hours post mortem as follows. The intact posterior scleral shell of each eye was pressurized from 5 to 45 *mmHg* while the 3D displacements of the scleral surface were measured using speckle interferometry Figure 37.

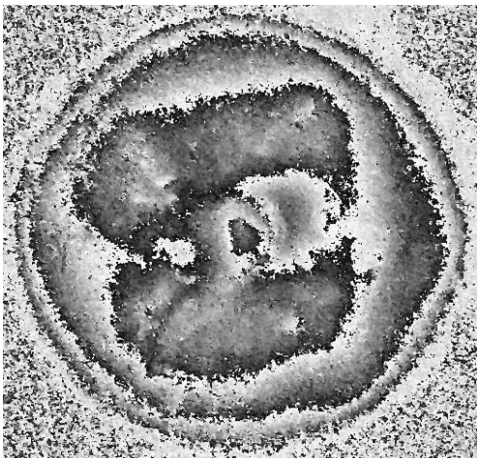

Figure 37. Speckle interferometry phase map after pressurization.

A finite element model of each scleral shell was constructed using data from a 3D digitizer (topography) and 20 MHz ultrasound transducer (thickness) Figure 38.

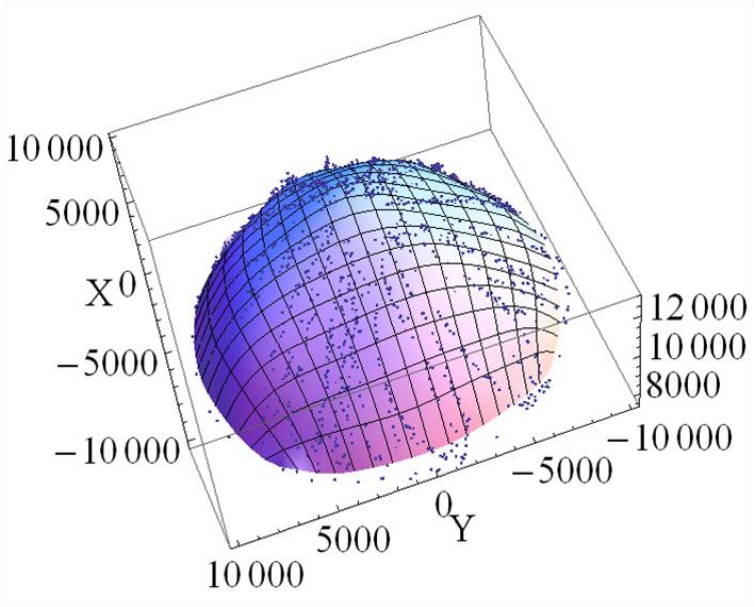

Figure 38. The geometric reconstruction of a scleral shell using 3D digitizer data.

A custom method has been developed to obtain a system of continuous functions that define the deformation fields (Figure 39).

A fiber-reinforced constitutive model that included both predominant collagen fiber orientation and stretch-induced collagen fiber stiffening was applied to each model of the eye, and a unique set of scleral mechanical properties were obtained by an inverse finite element method approach best fitting experimental and numerical displacement data.

The model parameters C_1 and C_3 describe the stretch-induced stiffening of the collagen fibers, but do not represent a direct measure of scleral stiffness at each IOP level. To capture scleral tissue stiffness two additional quantities were calculated and mapped: the tangent modulus along the preferred fiber orientation and the tangent modulus perpendicular to the preferred fiber orientation. Both tangent moduli represent an estimation of local scleral tissue stiffness. Moreover, tangent modulus can be computed at each IOP, and it is function of the model parameters and of the local collagen fiber stretch.

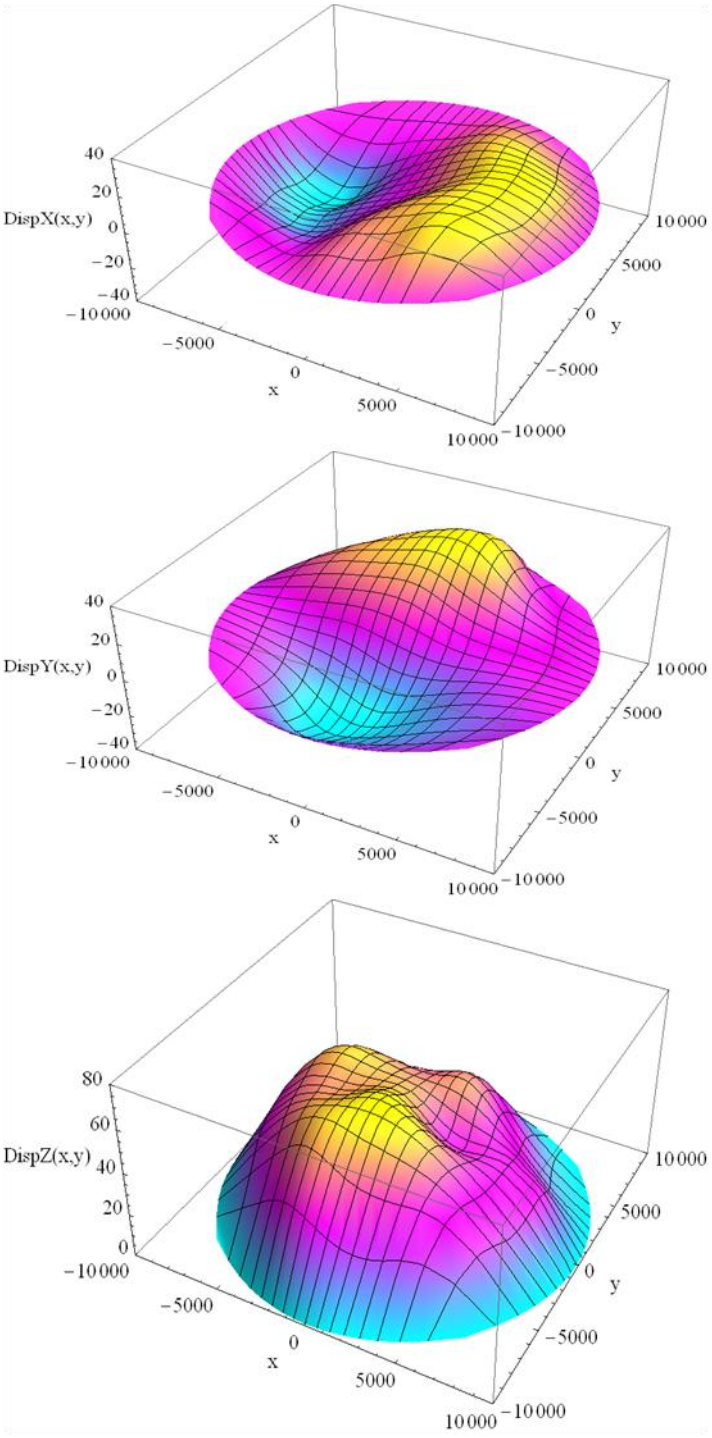

Figure 39. X, Y, and Z components of the continuous deformation functions fitting the experimental data.

Obviously, the tangent modulus varies at each integration point of the FE elements. This implied a statistical sampling of those values.

For the sake of clarity, only the median value of the tangent moduli distribution obtained for each tested eye is reported. The values of the tangent moduli is computed for the pressure levels of 10, 30, and 45 *mmHg*.

5.3. Preliminary Outcomes From Human Eyes Data Fitting – Numerical Results

As mentioned before it has been used a regionalization criteria that allowed to obtain 4 parameters defining the local fiber orientation of the elements belonging to the peripapillary sclera, and 4 different parameters for the peripheral sclera. This allowed the separate computation of the average stiffness of the peripapillary and peripheral scleral tissue along the parallel and perpendicular direction of the fibers.

The displacement maps obtained by the numerical FE model selected by the genetic algorithm based procedure can be compared in Figure 40 with the experimental displacement map recorded by the ESPI.

In this figure are shown the displacement maps in the X, Y, and Z components at a pressure level of 10, 30, and 45 *mmHg*.

Moreover, in this figure it can be noted that in-plane displacement magnitude is much lower than out-of-plane displacement magnitude. This condition justifies the assumption that the error committed by not accounting for the real direction of the sensitivity vectors should not heavily affect the outcome generated by the genetic algorithm procedure that is manly driven by the out-of-plane displacement component.

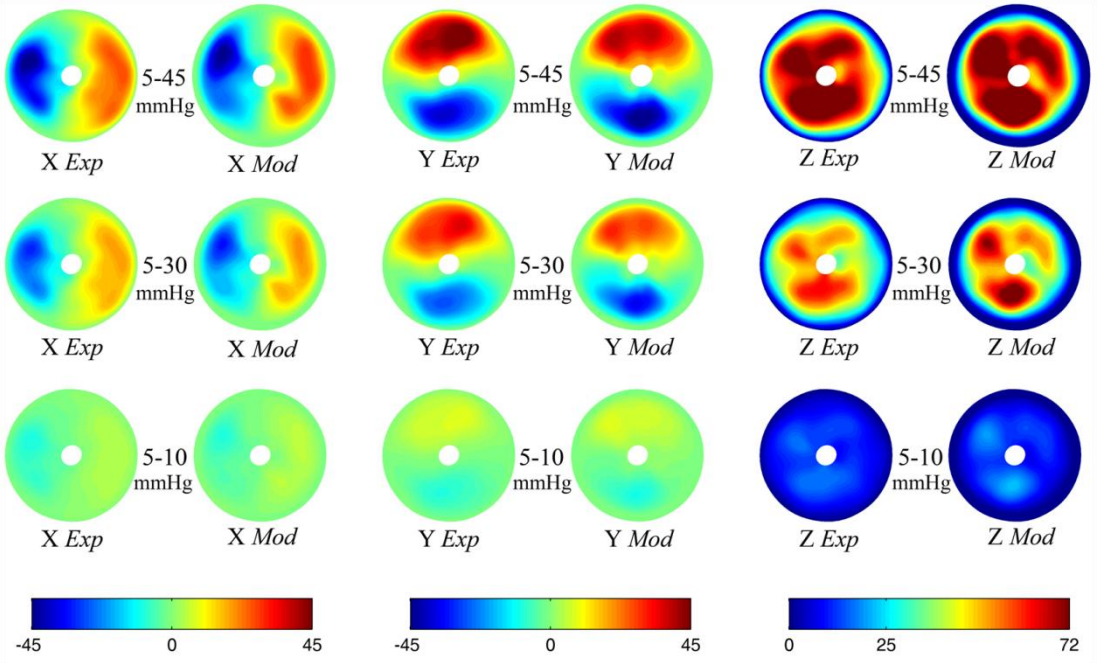

Figure 40. X, Y, and Z displacement components (in *μm*) for one eye showing the comparison between experimental measures (*Exp*) and model predictions (*Mod*) for three IOP ranges: 5-10, 5-30, and 5-45 mmHg. Model predictions were calculated using the final fitted scleral material property parameters for this eye.

In Figure 41(above) is drawn the median value for each eye of the plotted parameter. The outcome (median value) for the eyes showing the lower and higher values of the parameter are drawn using a thick line, while the remaining two outcomes (from the two eyes left) are drawn using dashed lines. In this way it is drawn the envelope of the distribution for both the peripapillary and peripheral region. The violet-shaded envelope shows the trend of the parameter as a function of the IOP for the elements belonging to the peripapillary sclera, while the red-shaded one for the peripheral sclera.

In Figure 41 (below) the same drawing criteria is used to plot the trend of the median value of the tangent modulus along the direction perpendicular to the preferred fiber orientation for all the four tested eyes.

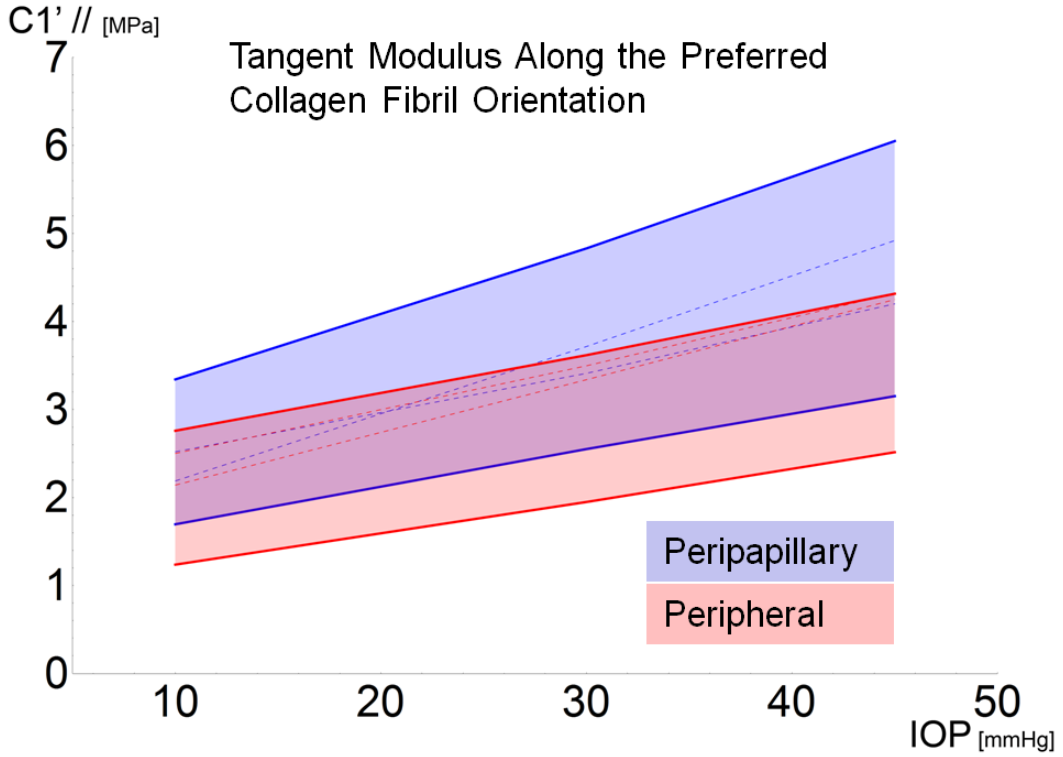

Figure 41. Tangent modulus of the sclera along (above) and perpendicular (below) to the predominant fiber direction for the peripapillary (blue) and peripheral (red) sclera evaluated at the pressure levels of 10, 30, and 45 *mmHg*. Every line represents the trend of the tangent modulus for one eye. Maximum and minimum values are represented by a continuous line, while the intermediate are represented by the dashed one.

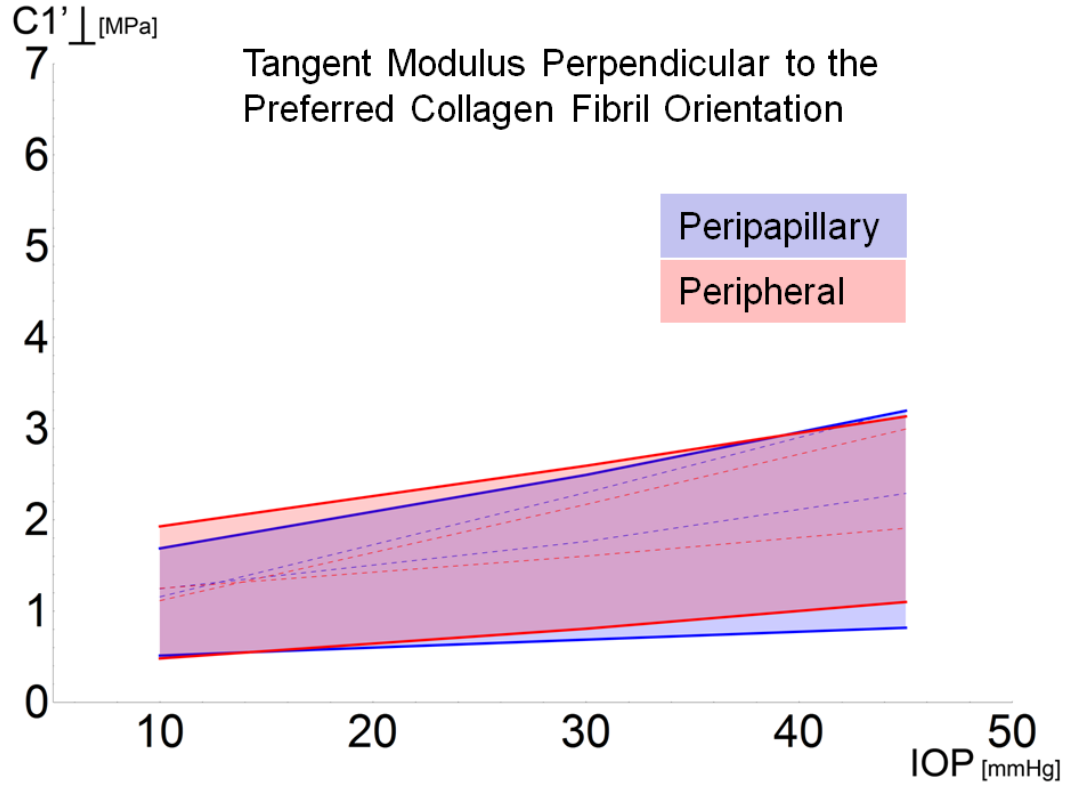

To highlight the stiffening of the sclera when IOP is increased it is plotted the trend of the maximum principal strain value Figure 42.

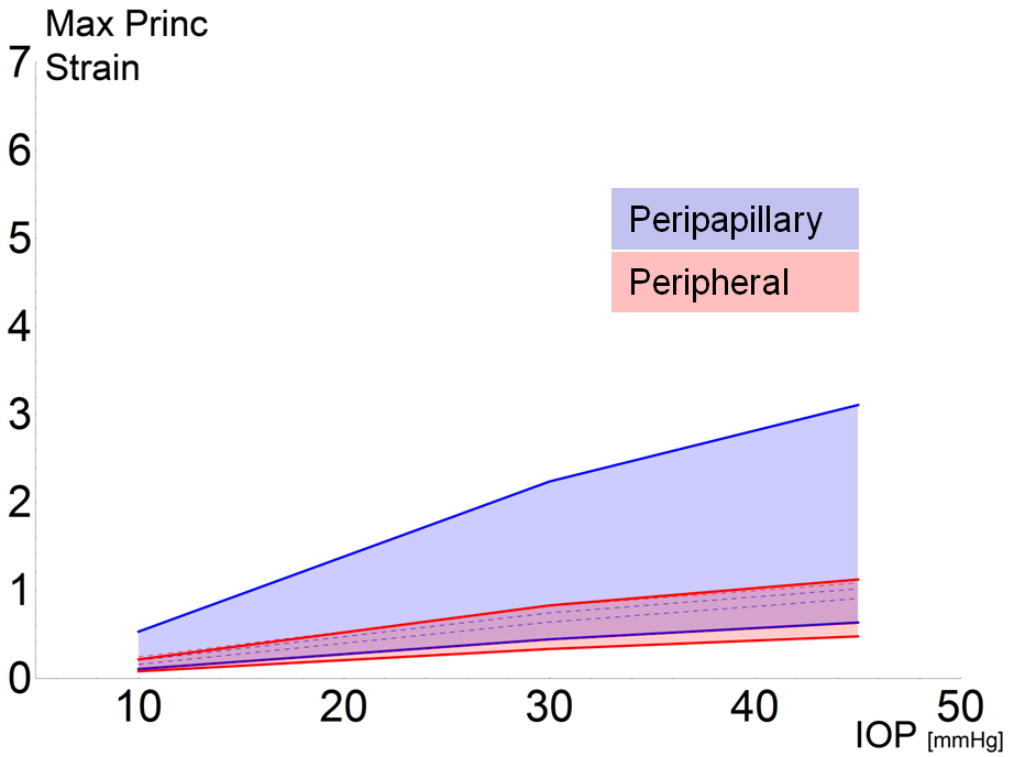

Figure 42. Maximum Principal Strain trend in the peripapillary (blue) and peripheral (red) sclera at pressure levels of 10, 30, and 45 *mmHg.*

By observing the reported figure it can be noted the increase of the stiffness in both the considered preferred fiber directions. It is worth of remind that a material having a linear stress-strain relationship would show a constant tangent modulus trend, since the tangent modulus is computed by the first derivative of the stress-strain curve.

In this figure it can be seen that the derivative of strain value along the local direction of the principal deformations decreases as IOP is increased. In this case, a direct relationship between stiffening and IOP cannot be assessed.

For a linear material the strain-IOP curve would be linear as well. Maximum principal strain trend shown in Figure 42 highlights an increase less than

linear when IOP is elevated. This would suggest a stiffening of the tissue as already observed in the analysis of the tangent modulus values.

While tangent modulus is a parameter directly related (by its definition) at the stiffness of the material, the strain value it can be only considered as an indirect indicator of the global stiffness locally present in the regions of the tested material.

Strain relates to stiffness by several geometrical factors, such as local thickness and shape of the surface.

The less than linear (negative tangent) strain value increase can be very likely justified by a stiffening of the tissue for two reasons:

1. Even if the thickness would locally remain constant during the deformation process (but it actually decreases) the strain-IOP curve would be linear (null tangent), so the negative tangent of the curve it would not be observed.
2. Due to the small amount of deformation experienced by the outer scleral shell (~100 μm) it is reasonable to neglect the geometric non-linearities that could cause the observed stiffening.

5.4. Preliminary Outcomes From Human Eyes Data Fitting – Comments

Experimental and numerical displacement maps were in good agreement for all the eyes. IOP-induced stiffening (nonlinearity) was marked in all the eyes as shown in Figure 41 wherein tangent modulus increases with IOP. Orientation-dependent stiffness (anisotropy) was clearly present in all eyes as shown in Figure 41. On average, the tangent modulus along the predominant collagen fibril direction was more than double the tangent modulus perpendicular to the predominant fibril direction in both the peripheral and peripapillary sclera.

Chapter 6

A New Approach of Speckle interferometric Data Analysis for 3D Objects

6.1. Introduction

In the previous section it has been mentioned that the reconstruction of the speckle data was performed by assuming some hypothesis usually considered in speckle holography.

The schematic representation of a Single-light and single-image absolute interferometer is again reported in Figure 43 to highlight dependency between the phase value recorded by the ESPI to the direction of the sensitivity vector. The last is function of the laser source position (illuminating direction) and of the CCD position (observing direction).

$$\phi = \frac{2\pi}{\lambda}\,\vec{d}.(\vec{K_i} - \vec{K_o}) = d_x K_x + d_y K_y + d_z K_z \qquad \text{(eq. 5)}$$

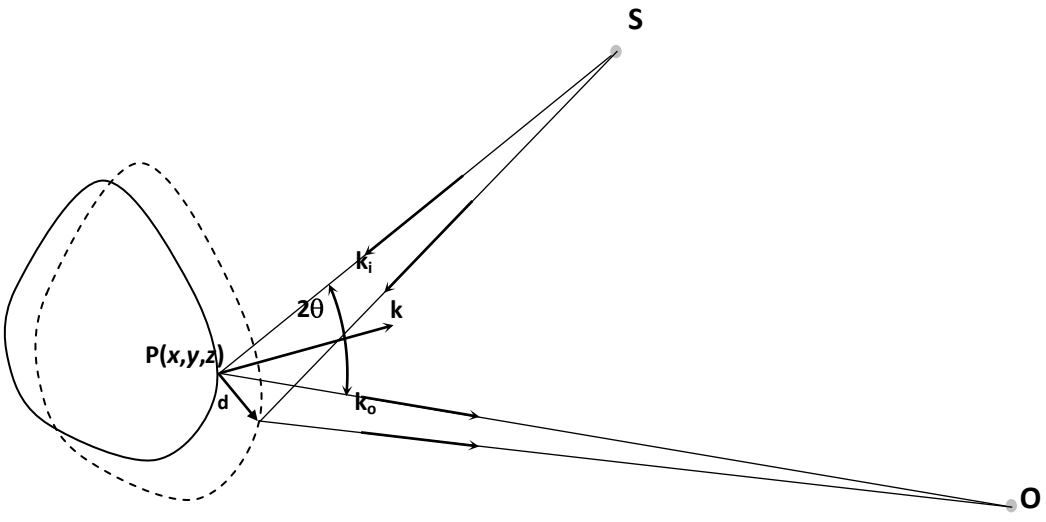

Figure 43. Schematic representation of a *Single-light and Single-image Absolute Interferometer.*

When speckle interferometry is used to acquire a deformation of an object the optical set-up is conveniently made to have the laser sources far enough from the deformed object to allow considering the wavefront of the lasers as series of waves parallel to each other.

In fact, if the laser source is far enough from the observed surface the laser waves ($\widetilde{K_i}$) can be assumed having all the same inclination respect to the observing direction ($\widetilde{K_o}$). This allows to consider the direction of the sensitivity vector not changing as a function of the observed point P(*x,y,z*).

In the optical set-up adopted in this work the observed object (scleral shell) is positioned less than 40 *mm* away from the CCD of the ESPI camera. This was done to have almost all the viewing region of the CCD observing the scleral shell.

The spherical geometry of the eye that usually has a radius of 12 *mm* made the distance between the CCD and the surface varying from around 40 *mm* at the equator of the shell to less than 30 *mm* at the tip.

The strong variation of distance between the CCD and the points of the observed surface doesn't allow to consider the laser waves hitting the surface with all the same direction.

As mentioned, this not satisfied assumption has been estimated in causing an error of a 3-5% of the deformation value for the out-of-plane component, and in a 15-35% in the in-plane components.

The cost function of the genetic algorithm is driven by the out-of-plane displacement component, so the set of material properties obtained by the procedure is not heavily affected by not considering the real direction of the sensitivity vectors.

In the next chapter it will be presented a micro scale based numerical fitting method developed by Rafael Gryt (Grytz & Meschke, 2010). This new fitting method aims to assess the non-linear anisotropic mechanical properties of

the sclera by means of a local adaptation criteria based on the fibers' stiffness and direction.

Because of the local adaptation that the method uses, it is very important that all the displacement components of deformation are congruently defined. For using this new fitting method it is not tolerable an error of the 15 - 35% in the in-plane displacement components.

For this reason it has been implemented a customized procedure written in *Mathematica*^{TM} to discharge all the simplifying assumptions previously assumed and to reconstruct the exact deformation displacement field that the scleral shell experienced during the inflation test.

6.2. Fitting and Analysis Method

It is briefly recalled the B-spline based fitting system method described in chapter 3:

The experimental data obtained by the interferometer consists of four phase maps for each load step. A typical set of experimental data is reported in Figure 29, which represents the four displacement components measured by the interferometer, these maps are quite similar to each other because at each point of the investigated area the in-plane components are much smaller than the out-of-plane component.

After the unwrapping of the phase maps a fitting procedure was applied to the experimental data in order to attain a smooth distribution over the observed domain. Figure 30 reports the shapes of cubic polynomial functions that define the functions along the radial direction. These functions were defined such as they assume zero value in correspondence of the maximum radius of the region of interest. This assumption is consistent with the loading configuration of the investigated tissues, which are clamped at the outer radius by the charging apparatus described in the previous section. The

order of polynomials reported in the figure is that used in the fitting of experimental data analyzed in the present paper. In the circumferential direction were used *k* integer harmonics based on sin and a cos functions plus a constant term.

Hence the generic overall fitting function for *n* control points along the radial coordinates and for *k* integer harmonics along the circumferential direction assumes the following form:

$$\begin{aligned} F(r,\theta) = {} & w_1 N_1(r) + \cdots + w_n N_n(r) + \\ & + [w_{n+1} N_1(r) + \cdots + w_{2n} N_n(r)]\cos\theta + [w_{2n+1} N_1(r) + \cdots + w_{3n} N_n(r)]\sin\theta + \cdots + \\ & + [w_{n(2k-1)+1} N_1(r) + \cdots + w_{n(2k-1)+n} N_n(r)]\cos k\theta + [w_{n(2k)+1} N_1(r) + \cdots + w_{n(2k)+n} N_n(r)]\sin k\theta \end{aligned}$$

(eq. 24)

where w_i are the *n*x(2*k*+1) weights to be evaluated by an optimization procedure based on the least square method.

After the computation of the pseudo-inverse of the matrix whose elements are the values that the functions to be linearly combined assumes at each experimental point, the weights w_i are estimated by multiplying this new matrix by the experimental data. Thus if *m* experimental data are available, the matrix for which the pseudo-inverse must be evaluated assumes the following form:

$$\begin{bmatrix} N_1(r_1) & \cdots & N_n(r_1) & N_1(r_1)\cos\theta_1 & \cdots & N_n(r_1)\cos\theta_1 & N_1(r_1)\sin\theta_1 & \cdots & N_n(r_1)\sin\theta_1 & \cdots\cdots & N_1(r_1)\cos k\theta_1 & \cdots & N_n(r_1)\cos k\theta_1 & N_1(r_1)\sin k\theta_1 & \cdots & N_n(r_1)\sin k\theta_1 \\ \vdots & & \vdots & \vdots & & \vdots & \vdots & & \vdots & & \vdots & & \vdots & \vdots & & \vdots \\ N_1(r_m) & \cdots & N_n(r_m) & N_1(r_m)\cos\theta_m & \cdots & N_n(r_m)\cos\theta_m & N_1(r_m)\sin\theta_m & \cdots & N_n(r_m)\sin\theta_m & \cdots\cdots & N_1(r_m)\cos k\theta_m & \cdots & N_n(r_m)\cos k\theta_m & N_1(r_m)\sin k\theta_m & \cdots & N_n(r_m)\sin k\theta_m \end{bmatrix}$$

(eq. 25)

where (r_i) are the coordinates in a polar coordinate system of the *i*-th point at which the experimental datum is retrieved.

This procedure has been validated by a specimen consisting in a spherical balloon clamped on the charging apparatus and loaded by the typical pressure increments imposed during the testing of the sclera shell.

Subsequently, the procedure was applied to human eyes provided by cadaver donors.

As already specified in the description of the experimental equipment, the posterior scleral shell must be tested in physiological solution in order to prevent the rapid degradation of the biological tissues. Hence, due to the non perpendicular illumination and to the proximity to the specimen of the spherical wavefronts produced by the interferometer, it was necessary to take into account both of the effects of the refractive phenomena when the light passes from air to saline solution, and of the non constant direction of the sensitivity vectors at each point of the specimen. Furthermore the problem was complicated by the non-planar development of the surface under test.

In particular, it has been taken into account the change in direction that laser wavefronts experienced when they passed through media of different refractive index (Snell's law), and the shortening of the wavelength that any electromagnetic wave undergoes when it passes from media having different refractive indexes (Figure 44).

A feature of electromagnetic waves is that they keep a constant oscillation period. This is defined by the frequency of the wave independently from the refractive index of the propagating media.

At the contrary, the propagation speed of an electromagnetic wave in a media is function of the refractive index.

$$\frac{c}{v} = n \qquad \text{(eq. 32)}$$

Where v is the propagation speed of the wave in a media having refractive index *n*, and *c* is the speed of light. The wavelength of an electromagnetic wave is function of the propagation speed and of the frequency of the wave.

$$\lambda = \frac{v}{f} \qquad \text{(eq. 33)}$$

Where λ is the wavelength and f is the frequency of the electromagnetic wave. By these definitions it can be obtained the relationship between the different wavelengths the same electromagnetic wave assumes when it passes through two different media having refractive index n_1 and n_2.

$$\frac{\lambda_0}{\lambda} = \frac{\frac{c}{f}}{\frac{v}{f}} = \frac{c}{v} = n \qquad \text{(eq. 33)}$$

With λ_0 the wavelength it assumes when it propagates in vacuum

$$\frac{\lambda_1}{\lambda_2} = \frac{\frac{v_1}{f}}{\frac{v_2}{f}} = \frac{v_1}{v_2} = \frac{n_1}{n_2} \qquad \text{(eq. 34)}$$

Snell's law (Figure 44): $$\frac{n_1}{n_2} = \frac{\sin\theta_1}{\sin\theta_2} \qquad \text{(eq. 35)}$$

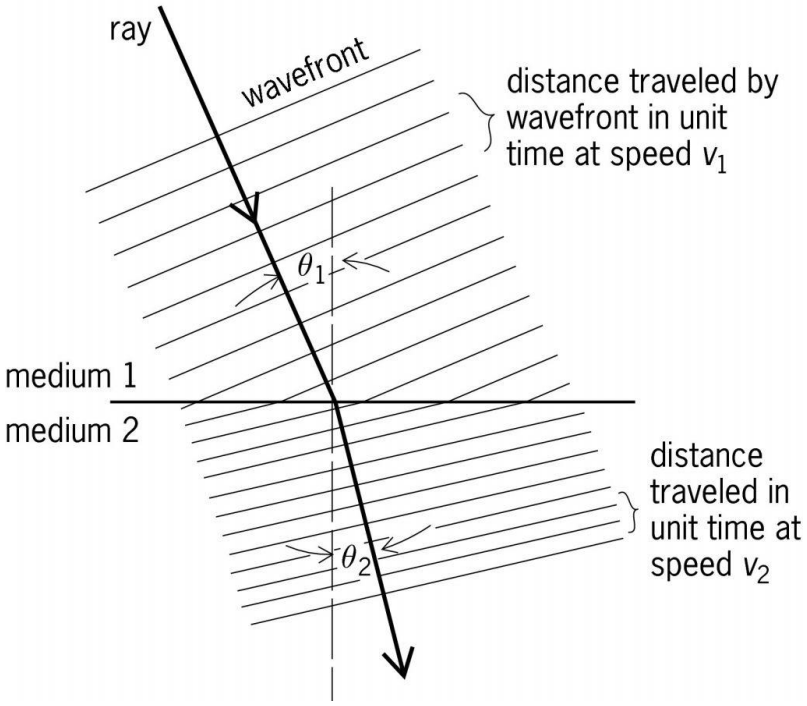

Figure 44. Modification of the laser wavefront due to the change of diffractive index of the media transmitting the electromagnetic wave. It can be observed the change in direction described by the Snell's law and the shortening of the wavelength due to the change of transmission speed. (Figure obtained by: http://encyclopedia2.thefreedictionary.com/Refraction+of+waves).

All these optical phenomena can be managed by considering the accurate knowledge of the geometry of the specimen, of the light source positions, of the viewpoint location, and of the geometry of the charging apparatus. Figure 45 reports a scheme emphasizing the geometrical quantities necessary to calculate at each point the sensitivity vector direction $\widetilde{K_i}$ for a single illumination direction:

- The location of the generic point of the specimen $P(x,y,z)$ whose deformation vector has to be computed.
- The coordinates of the spherical wavefront centered in S_i.
- The coordinates of the observation point V.

The refractive phenomena occurring when the light travels through the silica window separating the air from *PBS* are neglected, due to the small thickness of the window (0.5 *mm*).

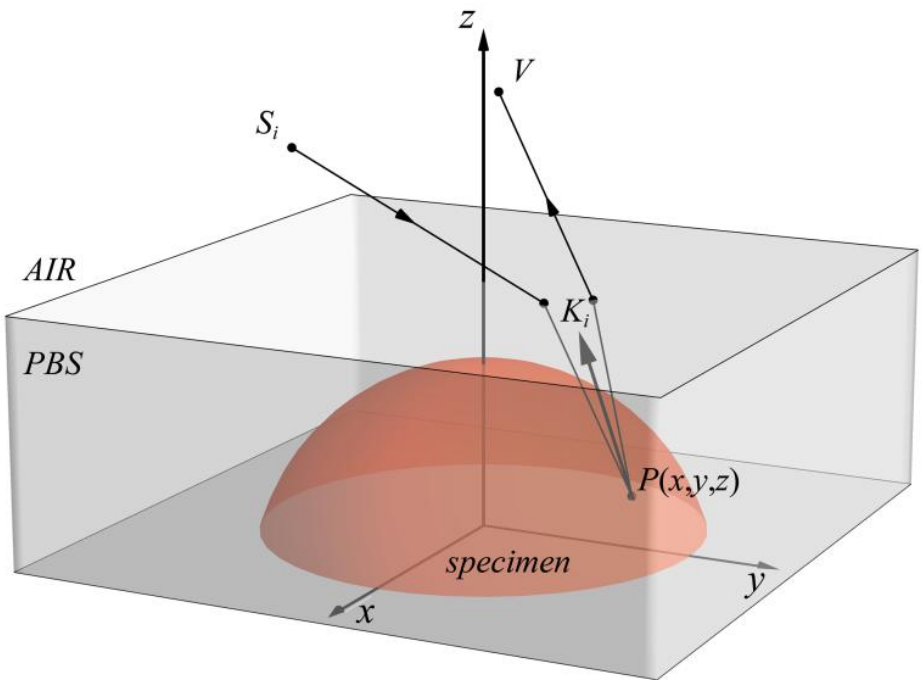

Figure 45. Schematic representation of the sensitivity vector direction (*Ki*) computation when the specimen is illuminated by a spherical wavefront centered in S_i and the observation point in *V*. Refractive implies the bending of the light when passing from air to *PBS,* and the shortening of the wavelength.

The validation of the method, initially carried out on a specimen faking the mechanical behavior of the scleral tissues – i.e. a polymeric balloon, consisted in the measurement of the full displacement field for a pressure step of 0.03 *mmHg*, with the balloon inflated both inside and outside the chamber containing the physiological solution (PBS). For these test performed on the polymeric balloon, the geometry was assumed to be a spherical cap with a diameter equal to 27.5 *mm*, and clamped in such a manner that top point of the sphere is 5 *mm* far from the upper surface of the clamping stage.

Figure 46 reports the undeformed (gray surface) and deformed (colored surface) geometry of the upper (half) surface of the polymeric balloon whose displacements are measured by the interferometer. Due to the small entity of the displacement (any micrometer) the deformed geometry is represented by amplifying the measured deformations by a factor of 600. It should be noticed that the expansion of the balloon is not uniform; in fact in the proximity of the vertical axis the deformations are smaller than the ones far from this area. This fact is due to the non-uniform thickness of the balloon, which is thicker near the axis for manufacturing reasons. On the other hand the whole measuring process – i.e. hardware and software – proved to be very sensitive, to retrieve these small quantities, and sufficiently repeatable, to be used for quantitative analysis of the mechanical behavior of materials tested in similar operating conditions.

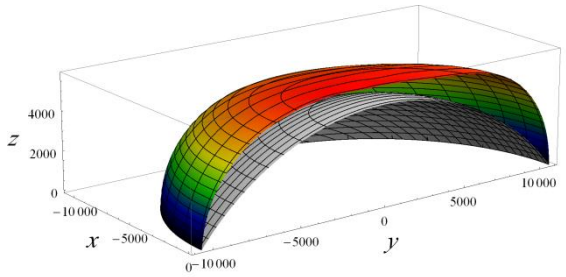

Figure 46. Undeformed (gray surface) and deformed (colored surface) geometry of the specimen under investigation. All the dimensions are in micrometers, displacements of the deformed geometry are amplified by a factor of 600.

The results obtained by choosing a fitting function formed by 54 terms linearly combined (n=6, k=4) are reported in the grid of the contour graphics of

Figure 47. In this figure the columns represent the three displacement components (u_x,u_y,u_z), the first three rows (AIR1, AIR2, AIR3) the displacements occurring when the specimen is outside the chamber, the last three rows the displacements retrieved when the specimen is inside the chamber (SOL1, SOL2, SOL3).

All the graphs of

Figure 47 are obtained at the theoretical same pressure level, in practice an unavoidable uncertainty in the imposed pressure is always present. Intentionally it has been applied the smallest load increment attainable by the charging apparatus.

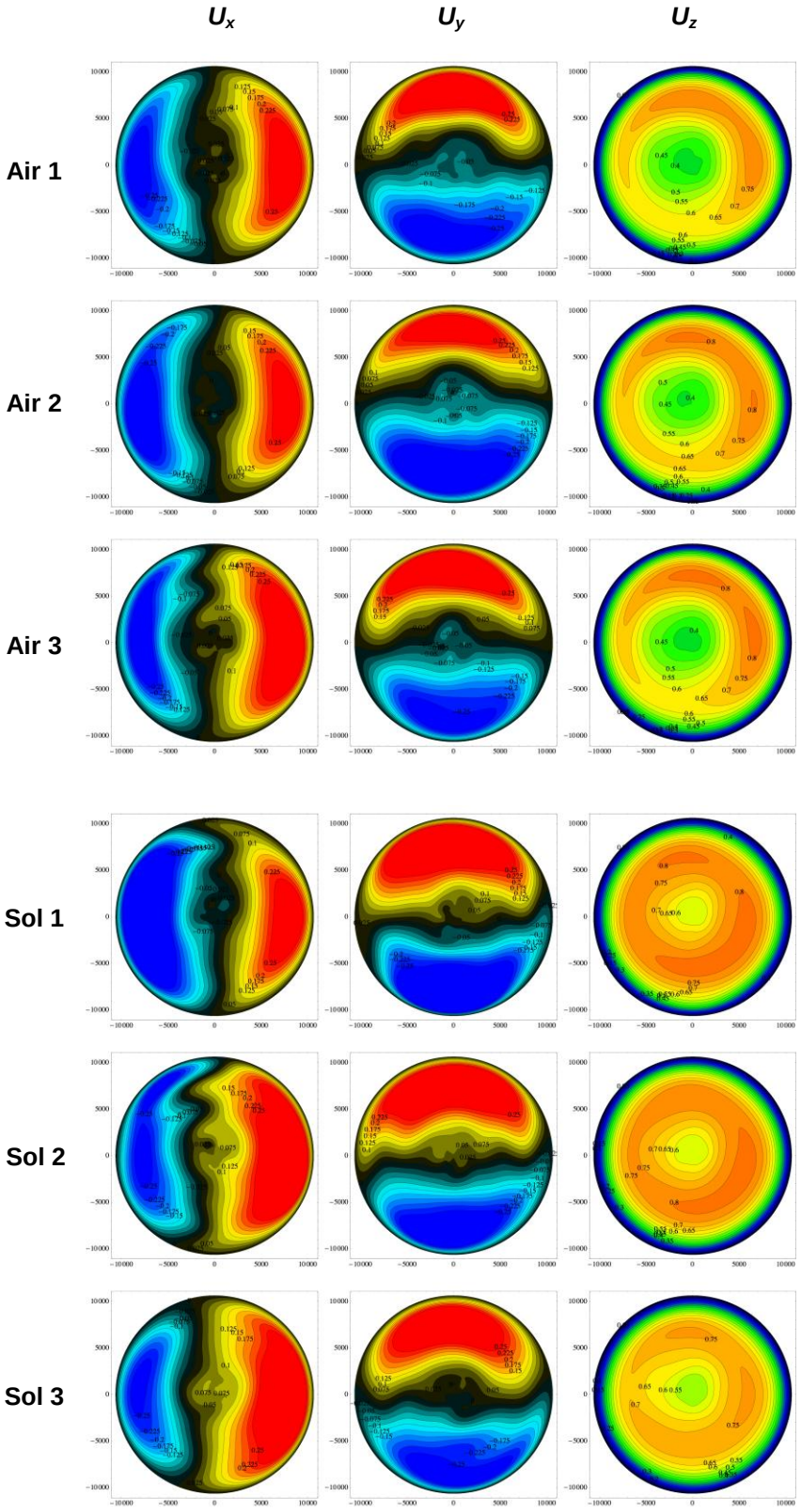

Figure 47. Contour plots of the displacement components (u_x, u_y, u_z) when the balloon is tested outside the chamber (Air 1, Air 2, Air 3) and inside the chamber (Sol 1, Sol 2, Sol 3). All the dimensions (x- and y- axes) and the displacements (contour labels) are in micrometers.

Nevertheless the proposed method exhibits a high repeatability. In fact, the results of the six tests carried out on the specimen are quite similar, and the inaccuracy observed in the measurements is significantly smoothed when a proper number of phase maps is cumulated. When the scleral tissues were tested not less than 15÷50 phase maps were cumulated, and this is a number of steps sufficiently high for averaging the inaccuracy due to the threshold error of the pressure loading system.

After the validation of the method carried out on the polymeric balloon, the measurement procedure was applied to a test performed on a human eye.

At first, the shape of the eye was acquired by a 3D mechanical digitizer (Immersion, model MicroScribe G2X), by which the coordinates of about 2500 points were determined with a nominal resolution of 0.23 *mm*, and fitted by the same model defined above for the balloon (fitting function formed by 54 terms, i.e. n=6 and k=4).

Figure 48 reports the results of the fitting of the point cloud acquired by the digitizer. The shape of the eye obtained by a least square method is represented in the figure by the colored surface whose contours represent the equidistant loci from the *xy* plane, which is assumed coincident with the upper surface of the clamping stage. Because of the presence of the optic nerve (ON) near the axis of the scleral shell, the shape data were fitted by the radial coordinate spanning from R_{min} and R_{max}, with R_{min} depending on the spatial obstruction of the ON (for the studied eye R_{min}=1.5 *mm*), and R_{max} depending on the hole diameter of the clamping stage (equal to 10 *mm*). Normally the ON is not located along the axis of the posterior scleral shell, this fact can be managed by changing the mathematical model used in the fitting procedure.

It must be pointed out that adopting a mechanical digitizer is not the best choice for shape acquisition of biological tissues. In fact, the pressurized tissues hardly maintain their original shape when they come into contact with the tip of the probe, this is due to the low stiffness of the tissues and the low

pressure applied to the specimen. Instead, the use of non-contact methods would provide more accurate and reliable results (Bianco, Bruno, Muzzupappa, & Luchi, 2010).

In the particular case of a human eye shape acquisition the almost spherical shape of the sclera shell doesn't require a very high resolution of the shape acquisition system. The low resolution of the adopted technique is compensated by a very high number of recorded points, and by the fitting method adopted to reconstruct the shape of the sclera shell.

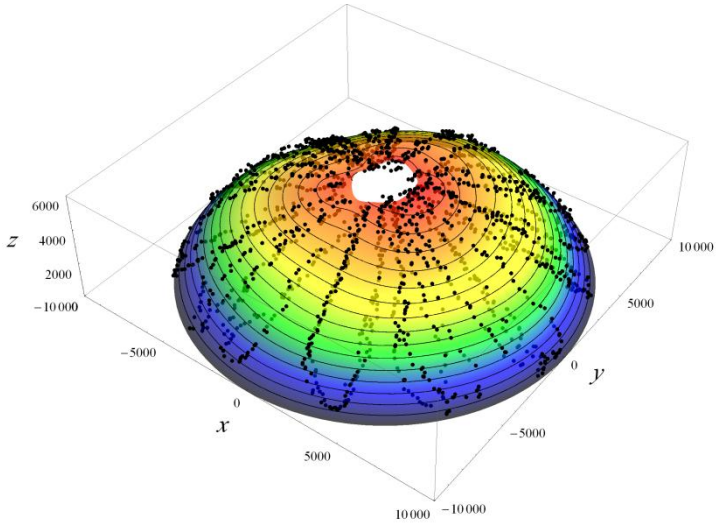

Figure 48. Best fit geometry (colored surface) obtained from the point cloud (black dots) acquired by the 3D mechanical digitizer.

By defining the shape of the specimen as an the analytical model, the sensitivity vectors can be calculated at each point of the observed area by taking into account the refractive phenomena, according to the geometry depicted in Figure 45. The human eye analyzed by the procedure proposed in the present paper was loaded by increasing the *IOP* from 4.81 *mmHg* to 45.46 *mmHg*, with step of 0.15÷0.54 *mmHg*; the entity of the steps depends on amount of deformations obtained when the pressure increment is applied.

The three displacement components obtained at three pressure increments are reported in the grid of contour plots of Figure 49. Qualitatively the graphs are similar to those reported in

Figure 47 obtained for the polymeric balloon, apart from the area surrounding the axis, where the experimental data are not significant. A careful comparison of

Figure 47 and Figure 49 reveals that the human eye exhibits a more heterogeneous mechanical behavior. In fact, in the right hand of the eye the in-plane displacements (u_x and u_y) are significantly smaller than the one in the left, and the out-of-plane displacements (u_z) in the area around the ON forms four lobes.

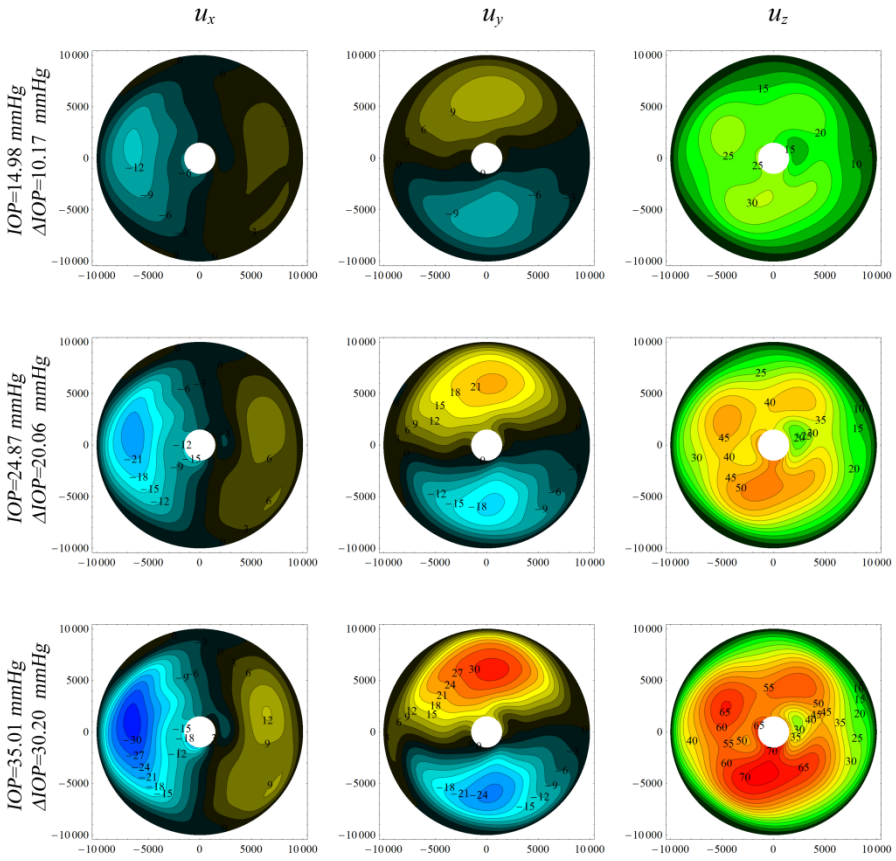

Figure 49. Contour plots of the displacement components (u_x, u_y, u_z) at three increment of pressure. All the dimensions (x- and y- axes) and the displacements (contour labels) are in micrometers.

Figure 50 reports the undeformed (gray surface) and deformed (colored surface) geometry when the IOP is equal to 14.98 *mmHg*. Also in this case the displacements are amplified by a factor of 50 in order to easily distinguish the two surfaces.

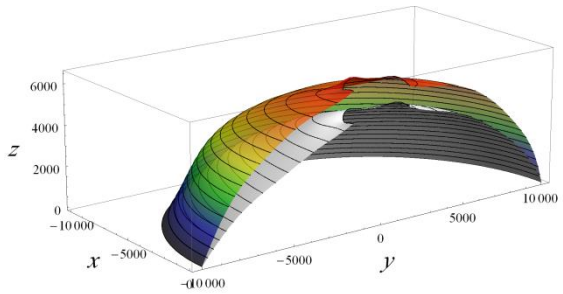

Figure 50. Undeformed (gray surface) and deformed (colored surface) geometry of the human eye at *IOP*=14.98 *mmHg*. All the dimensions are in micrometers, displacements of the deformed geometry are amplified by a factor of 50.

Finally, the analytical model of the geometry and of the displacements coupled with the information on the pressure measurement can be used to identify and quantify the necessary parameters for describing the mechanical behavior of the human sclera.

For instance, with regards to Figure 51, it is considered the module of the displacement vector versus the *IOP* variation for a point on the tip of the shell. A qualitative analysis of trend shows a non-linear curve that could address a structural stiffening of the scleral tissue.

A quantitative identification of the mechanical behavior of the human eye tissues requires the definition of a model and the measurement of its parameters, which is now under investigation by the author, and it will be the subject of future studies.

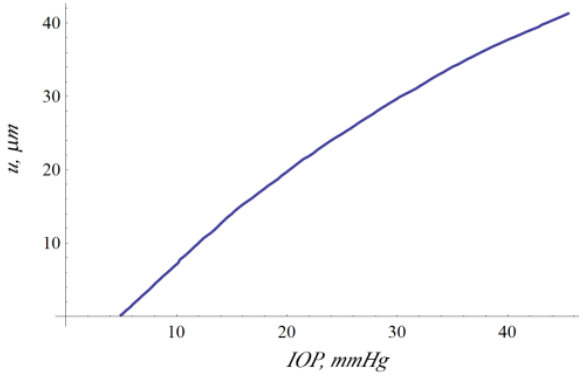

Figure 51. Module of the displacement vector of a point on the tip of the shell when the *IOP* was varied from 4.81 *mmHg* to 45.46 *mmHg.*

6.3. Comments on the Adopted Procedure

This fitting method presents a complete procedure for analyzing the experimental data obtained from mechanical test of biological tissues. The load applied to the specimen consists in a monotonic increase of pressure in the range that a human eye can experience. The displacement vectors were measured at each point of the observed specimen by a commercial speckle interferometer. The procedure, initially validated on a specimen consisting of a polymeric balloon, is addressed to the analysis of the deformation induced in human eye tissues with the aim of obtaining quantitative information about the mechanical behavior of this kind of tissues. The proposed procedure, which was applied to a cadaver human eye of a donor, provides an analytical model by which the displacement components can be easily calculated at any point of the investigated region.

Chapter 7

3D Interferometric Data Analysis and Microscale-based Numerical Fitting Method – A New Approach

7.1. Inverse Numerical Estimation of Eye-Specific intrinsic Material Properties and Local Collagen Architecture

Reliable biomechanical models of individual human eyes require detailed knowledge of the nonlinear and anisotropic response of these soft connective tissues. Latest advances in inverse finite element approaches allow for eye-specific estimations of intrinsic nonlinear constitutive properties and the local collagen architecture from inflation tests on posterior scleral shells (Grytz et al. 2010, ARVO abstract 51, 2133). In this section, the results of an eye-specific inverse analysis of the experimental data set earlier shown in paragraph 5.3 are presented.

Inverse finite element analysis is based on the simultaneous optimization of model parameters at a global and a local level. The mechanical properties of the sclera were derived from a constitutive model that incorporates physically meaningful parameters such as the collagen fibril crimp (Grytz & Meschke, 2009) and the local orientation and dispersion of collagen fibrils (Grytz & Meschke, 2010).

Parameters responsible for the hyperelastic response such as the crimp angle and stiffness of collagen fibrils were assumed to be constant across each scleral shell (global level).

Parameters that determine anisotropy were allowed to vary locally. The global parameters were optimized using the method of feasible directions such that model deformation predictions matched the experimental surface displacements. At the local level, the predominant orientations and the

dispersion of collagen fibrils were adapted at each material point to match the 1st and 2nd principal strains obtained from the experimentally measured surface displacements.

The experimental procedure presented in chapter 6 was applied to the right eye of a human donor. The sclera shell was pressurized from 5 to 45 *mmHg* and relative surface displacements $\mathbf{u}^{exp}$ were calculated from 5 *mmHg* at nine higher pressure levels *p* (7, 10, 15, 20, 25, 30, 35, 40, 45 *mmHg*).

To estimate the intrinsic material properties of the eye, the optimization algorithm was set to minimize the difference between the predicted FE displacements $\mathbf{u}^{FE}$ and the experimentally measured surface displacements $\mathbf{u}^{exp}$ by means of the following objective function:

$$\epsilon = \sum_{p=1}^{9} \left(\frac{\sum_i (\mathbf{u}_{p,i}^{\mathrm{FE}} - \mathbf{u}_{p,i}^{\mathrm{exp}})^2}{\sum_i (\mathbf{u}_{p,i}^{\mathrm{exp}})^2} \right)^2 \qquad \text{(eq. 36)}$$

where $\sum_i$ represents the summation over all nodes of the outer surface of the scleral shell.

First, only a global optimization of the nonlinear material properties was applied disregarding local anisotropic effects induced by the collagen architecture. In Figure 52 the numerically estimated surface displacements are compared to the experimental measurements for x-, y-, and z-displacements at three selected IOP levels. The optimal set of global constitutive parameters minimized the error estimator to ε = 0.01784. In a second analysis, the local optimization of the collagen architecture was incorporated into the inverse analysis. The displacement estimations of the second analysis are compared to the experiment in Figure 53. The optimal set of global and local constitutive parameters minimized the error estimator to ε = 0.01081. Incorporating the local anisotropy into the fitting procedure improved the inverse estimation of the tissue displacement response significantly as the displacement error was reduced by 39%.

The two-level optimization approach was able to estimate the detailed mapping of the local collagen architecture in the eye-specific scleral shell that engendered computed displacement and strain fields best matching the experimental inflation test results.

Estimated local collagen architecture is plotted in Figure 54. The model predicted that collagen fibrils in the sclera were largely randomly oriented except for the peripapillary region. The models predicted that a circumferential annulus of fibrils surround the scleral canal in the peripapillary sclera. If this circumferential annulus is predicted for a significant number of eyes, it would present a mechanical interpretation of the fibrils architecture around the ONH, as suggested in a study on the arrangement of collagen fibrils in human eyes (Oyama, Abe, & Ushiki, 2006).

The numerical inverse analysis presented here requires a detailed knowledge of the experimental strain field of the specimen, which in turn requires for a highly accurate recording and processing of the experimentally obtained surface displacements. Herein, full-field experimental displacement measurements with a resolution below 1 micron are a prerequisite to estimate local anisotropic inhomogeneities from scleral shell inflation tests. Only by incorporating the different correction steps outlined in chapter 6 was it possible to provide the required accurate experimental displacement maps to the inverse analysis.

Figure 52. Comparison of experimental surface displacements and numerically estimated displacements assuming isotropic collagen architecture.

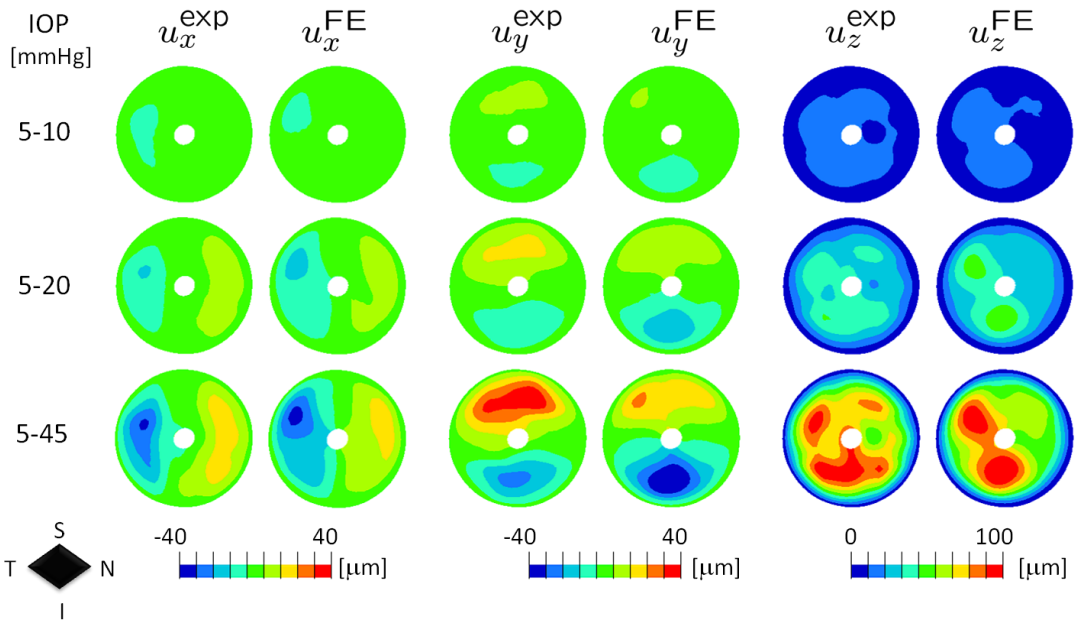

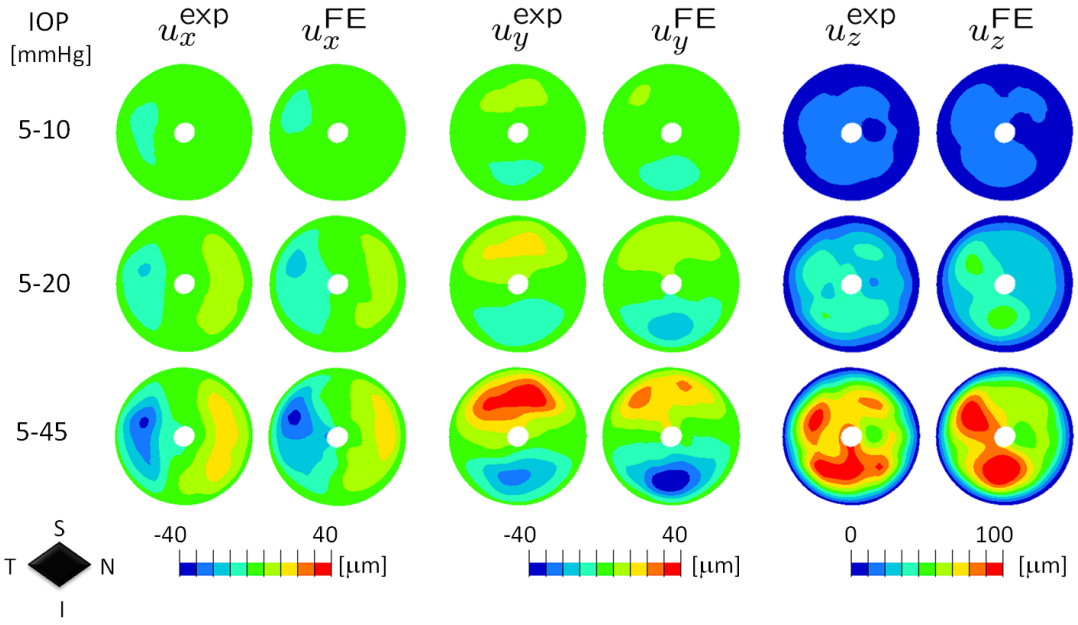

Figure 53. Comparison of experimental surface displacements and numerically estimated displacements assuming locally anisotropic collagen architecture.

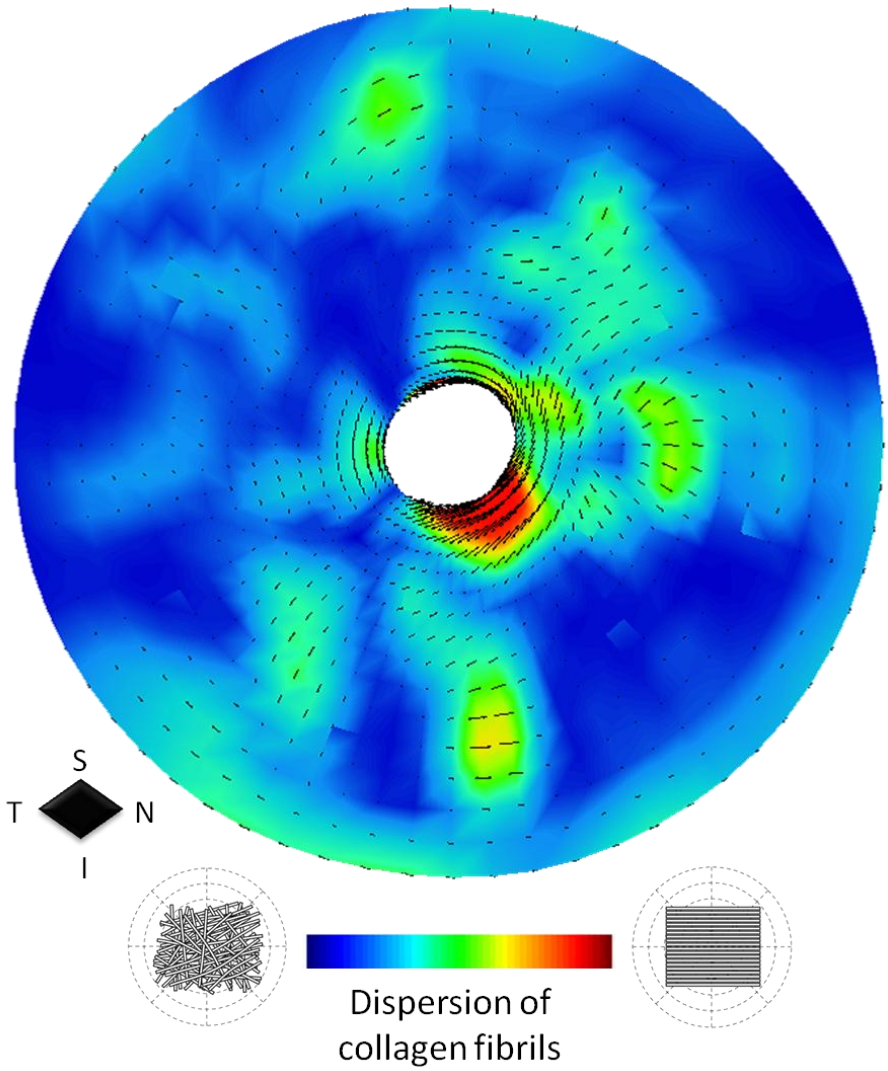

Figure 54. Local collagen architecture estimated by the two-level optimization approach. Contour plot: collagen fibril dispersion; black lines: preferred collagen fibril directions.

Chapter 8

Comments and Conclusions

8.1. Overview of the Mechanical Testing and Analysis Procedure

The work presented in this dissertation describes an experimental and numerical procedure to test and analyze speckle interferometric data collected by mechanical inflation tests performed on human eyes, with the aim of assessing the non-linear anisotropic mechanical behavior of human sclera.

Speckle interferometry has been adopted as measurement technique to record the deformation field induced in the scleral shells during an inflation test performed using a custom pressurization apparatus.

The inflation test consists of applying a pressure-controlled hydraulic load to the scleral shells while trying to preserve the physiological geometrical configuration of the sclera.

Experimental data recorded by the Electronic Speckle Pattern interferometer (ESPI) used in this work have been analyzed by a new, custom, fully automated routine written in *Mathematica*^{TM}. This routine has been used to completely replace the commercial software accompanying the interferometer (Q100, Dantec Dynamics A/S, Denmark) that was previously used to reconstruct the recorded displacement fields.

A second routine written in *Mathematica*^{TM} has been used to compensate for some assumptions used in classic holography that were not satisfied due to the particular optical conditions of the scleral pressurization testing set-up. This “compensation method” ensures accurate reconstruction of the real deformation field experienced by each tested specimen without incurring the errors associated with using the commercial software.

The new routines allow for the direct management of the raw recorded interferometry, scleral thickness and scleral surface geometry data, computation of the absolute phase change maps of the recorded speckle field (function of the recorded deformation fields) by performing a custom unwrapping procedure, and elimination of the errors associated with the change of the laser wavelength and the angle of the laser beams induced by speckle recording through an optical window in a saline-filled chamber (refraction changes).

Those errors in the displacement field computing were not significantly affecting the genetic algorithm-based procedure, but were not acceptable for the new material property fitting method developed by Rafael Grytz.

8.2. Comments on the Presented Preliminary Results

Results shown in Chapters 5, 6, and 7 are the preliminary outcomes of the newly developed procedures described herein. Results described in Chapter 5 are based on the material property fitting of four human eyes, which establishes the utility and accuracy of the new methodology.

While the presented sample is too small to allow statistical comparison of human scleral material properties, the relatively tight distributions of the estimated mechanical parameters indicate that they represent a meaningful description of the mechanical properties of human sclera.

These preliminary results highlight the strong non-linearity present in the strain-IOP relationship that characterizes the mechanical tissue behavior. The parameter used to emphasize this non-linearity has been the tangent modulus, which is directly related to the stiffness of the tissue, since it is by definition the derivative of the strain-IOP curve. The analysis of the tangent moduli obtained for all the tested eyes used for these preliminary results show that the human sclera gets stiffer has IOP is increased.

Moreover, it seems that the peripapillary sclera (the region of the posterior sclera shell close to the ONH) is stiffer than the peripheral sclera (the region closer to the equator of the eye). This finding suggests that the region around the ONH could provide mechanical “protection” to the ONH, the site of axon damage in glaucoma.

This hypothesis could represent a partial explanation for the stiffer nature of the peripapillary sclera. Studies carried by Ian Sigal and colleagues (Sigal & Ethier, 2009) using parametric FE models to analyze the factors that are most influential in the biomechanics of the ONH, have demonstrated that while a stiffer sclera usually corresponds to lower stress and strains at the level of the lamina cribrosa, this is not always the case when sclera is particularly compliant.

While the role of ocular biomechanics in glaucoma remains unknown, a detailed knowledge of scleral biomechanics is the starting point for a detailed analysis of the mechanical effects of IOP as it relates to glaucoma and the mechanobiology of the eye.

These preliminary results show that in human sclera anisotropy is very likely a mechanical feature of the tissue. The results obtained by the genetic algorithm-based procedure show that the best fit between the numerical and experimental displacement fields is achieved when significant anisotropy is introduced into the material description. It is worth noting that the material model allows for isotropy, but the best fit of the displacement fields have been achieved when the material parameters include both strong non-linearity and anisotropy.

A different approach has been considered in the fitting method described in Chapter 8. While the genetic algorithm-based fitting method is based on a mathematical formulation that attempts to reach the best fit of the experimental data using brute force numerical computation, the new fitting

method uses a formulation that mimics some of the physiologic structural features of the sclera itself. This new fitting method describes the mechanical properties of the sclera in terms of the angular dispersion and uncrimping rate of the collagen fibers that make up the sclera. The uncrimping rate is a function of the amount of stretch that bundles of fibers experience when the IOP load is increased. Hence, this formulation mimics the real mechanical behavior of the collagen fibers that constituting the posterior shell of the sclera, and as such the resulting parameters have real physical values that represent the collagen microstructure.

8.3. Final Conclusions

It has been hypothesized that ONH and scleral biomechanics play a crucial role in the IOP-induced axonal damage in glaucoma. Characterization of the mechanical behavior of human sclera is a crucial goal in the quest to better understand the biomechanical behavior of the ONH. The testing and analysis procedure presented herein has been shown to be an accurate and repeatable methodology for experimental determination of the biomechanics of the human sclera.

The final analysis of all the tested eyes will lead to the identification of the most important features of the mechanical properties of the human sclera, and how aging and ethnicity affect those properties. These findings will be applied to understanding important features of the etiology of glaucoma, the second leading cause of blindness in the world.

Bibliography

AGIS investigators, A. (2002). The Advanced Glaucoma intervention Study (AGIS): 12. Baseline Risk Factors for Sustained Loss of Visual Field and Visual Acuity in Patients With Advanced Glaucoma. *American Journal of Ophthalmology , 134* (4), 499-512.

Albon, J., Farrant, S., Akhtar, S., Young, R., Boulton, M. E., Smith, G., Et Al. (2007). Connective Tissue Structure of the Tree Shrew Optic Nerve and associated Ageing Changes. *Investigative Ophthalmology & Visual Science , 48* (5), 2134-2144.

Albon, J., Karwatowski, W. S., Avery, N., Easty, D. L., & Duance, V. C. (1995). Changes in the Collagenous Matrix of the Aging Human Lamina Cribrosa. *British Journal of Ophthalmology , 79* (4), 368-375.

Albon, J., Karwatowski, W. S., Easty, D. L., Sims, T. J., & Duance, V. C. (2000). Age Related Changes in the Non-Collagenous Components of the Extracellular Matrix of the Human Lamina Cribrosa. *British Journal of Ophthalmology , 84* (3), 311-317.

Albon, J., Purslow, P. P., Karwatowski, W. S., & Easty, D. L. (2000). Age Related Compliance of the Lamina Cribrosa in Human Eyes. *British Journal of Ophthalmology , 84* (3), 318-323.

Bailey, A. J., Paul, R. G., & Knott, L. (1998). Mechanisms of Maturation and Ageing of Collagen. *Mechanisms of Ageing and Development , 106* (1-2), 1-56.

Beghini M, B. L. (1999). Identificazione Della Curva Tensione-Deformazione Di Acciai Sulla Base Di Prove Di Durezza Strumentate. *XXVIII Convegno Nazionale AIAS* , (P. 597-606). Vicenza.

Belkoff, S. M., & Haut, R. C. (2008). *Experimental Methods in Biological Tissue Testing* (Vol. Springer Handbook of Experimental Solid Mechanics). Springer US.

Bellezza, A. J., Hart, R. T., & Burgoyne, C. F. (2000). The Optic Nerve Head as A Biomechanical Structure: initial Finite Element Modeling. *Investigative Ophthalmology & Visual Science , 41* (10), 2991-3000.

Bellezza, A. J., Rintalan, C. J., Thompson, H. W., Downs, J. C., Hart, R. T., & Burgoyne, C. F. (2003). Deformation of the Lamina Cribrosa and Anterior Scleral Canal Wall in Early Experimental Glaucoma. *Investigative Ophthalmology & Visual Science , 44* (2), 623-637.

Bianco, G., Bruno, F., Muzzupappa, M., & Luchi, M. L. (2010). Underwater Shape Reconstruction By Fringe Projection.

Broadway, D. C., Nicolela, M. T., & Drance, S. M. (1999). Optic Disk Appearances in Primary Open-Angle Glaucoma. *Survey of Ophthalmology , 43* (Suppl 1), S223-5243.

Brown, C. T., Vural, M., Johnson, M., & Trinkaus-Randall, V. (1994). Age-Related Changes of Scleral Hydration and Sulfated Glycosaminoglycans. *Mechanisms of Ageing and Development , 77* (2), 97-107.

Bruno, L. (2007). Global Approach for Fitting 2D interferometric Data. *Optics Express , 15* (8), 4835-4847.

Bruno, L., & Poggialini, A. (2000). Phase Retrieval in Speckle interferometry: A One-Step Approach. *Proceedings of interferometry in Speckle Light - theory and Applications* (pp. 461-472). Springer, Heidelberg, Germany: Jacquot P. and Fournier J. M.

Bruno, L., Pagnotta, L., & Poggialini, A. (2000). Laser Speckle Decorrelation in NDT. *Optics and Lasers in Engineering , 34* (1), 55-65.

Burgoyne, C. F., & Morrison, J. C. (2001). The Anatomy and Pathophysiology of the Optic Nerve Head in Glaucoma. *Journal of Glaucoma , 10* (5 Suppl 1), S16-8.

Burgoyne, C. F., Downs, J. C., Bellezza, A. J., & Hart, R. T. (2004). Three-Dimensional Reconstruction of Normal and Early Glaucoma Monkey Optic Nerve Head Connective Tissues. *Investigative Ophthalmology & Visual Science , 45* (12), 4388-4399.

Burgoyne, C. F., Downs, J. C., Bellezza, A. J., Suh, J.-K. F., & Hart, R. T. (2005). The Optic Nerve Head as A Biomechanical Structure: A New Paradigm for Understanding the Role of IOP-Related Stress and Strain in the Pathophysiology of Glaucomatous Optic Nerve Head Damage. *Progress in Retinal and Eye Research , 24* (1), 39-73.

Burgoyne, C. F., Mercante, D. E., & Thompson, H. W. (2002). Change Detection in Regional and Volumetric Disc Parameters Using Longitudinal Confocal Scanning Laser Tomography. *Ophthalmology, 109* (3), 455-466.

Cheng, S., Clarke, E. C., & Bilston, L. E. (2009). The Effects of Preconditioning Strain On Measured Tissue Properties. *Journal of Biomechanics, 42* (9), 1360-1362.

Chumbley, L., & Brubaker, R. (1976). Low-Tension Glaucoma. *American Journal of Ophthalmology , 81* (6), 761-767.

De Fazio, L., Syngellakis, S., & Fugiuele, F. M. (2001). Nanoindentation of CVD Diamond: Comparison of An FE Model With Analytical and Experimental Data. *Diamond and Related Materials , 10* (3-7), 765-769.

Doval, A. F. (2000). A Systematic Approach To TV Holography. *Measurement Science and Technology , 11* (11), R1.

Downs, J. C., Suh, J.-K. F., Thomas, K. A., Bellezza, A. J., Hart, R. T., & Burgoyne, C. F. (2005). Viscoelastic Material Properties of the Peripapillary Sclera in Normal and Early-Glaucoma Monkey Eyes. *Investigative Ophthalmology & Visual Science , 46* (2), 540-546.

Drance, S. M., & anderson, D. R. (1995). *Optic Nerve in Glaucoma.* Kugler Publications.

Driessen, N. J., Bouten, C. V., & Baaijens, F. P. (2005). A Structural Constitutive Model for Collagenous Cardiovascular Tissues incorporating the Angular Fiber Distribution. *Journal of Biomechanical Engineering , 127* (3), 494-503.

EGPS investigators, E. (2007). Predictive Factors for Open-Angle Glaucoma Among Patients With Ocular Hypertension in the European Glaucoma Prevention Study. *Ophthalmology , 114* (1), 3-9.

Eilaghi, A., Flanagan, J. G., Tertinegg, I., Simmons, C. A., Brodland, G. W., & Ethier, C. R. (2010). Biaxial Mechanical Testing of Human Sclera. *Journal of Biomechanics , 43* (9), 1696-1701.

Erf, R. (1978). *Speckle Metrology.* New York: Academic Press inc.

Fan, H., Wang, J., & Tan, Y. (1997). Simultaneous Measurement of Whole in-Plane Displacement Using Phase-Shifting ESPI. *Optics and Lasers in Engineering , 28* (4), 249-257.

Fechtner, R. D., & Weinreb, R. N. (1994). Mechanisms of Optic Nerve Damage in Primary Open Angle Glaucoma. *Survey of Ophthalmology , 39* (1), 23-42.

Fisher, N. I. (1993). *Statistical Analysis of Circular Data.* Cambridge, UK: Cambridge University Press, .

Flynn, T. J. (1997). Two-Dimensional Phase Unwrapping With Minimum Weighted Discontinuity. *Journal of the Optcial Society of America , 14* (10), 2692-2701.

Fratzl, P. (2008). *Collagen: Structure and Mechanics.* New York: Springer.

Friberg, T. R., & Lace, J. W. (1988). A Comparison of the Elastic Properties of Human Choroid and Sclera. *Experimental Eye Research , 47* (3), 429-436.

Geijssen, H. C. (1991). *Studies On Normal Pressure Glaucoma.* Amsterdam: Kugler Publications.

Genetic Algorithm. (2010-Genetic Algorithm, October 4). Retrieved 8 8, 2010, From Wikipedia: Http://En.Wikipedia.Org/Wiki/Genetic_Algorithm.

Girard, M. J. Scleral Biomechanics in the Normal, Glaucomatous and Aging Eye. Tulane University School of Science and Engineering, 2008, 353 pages. http://gradworks.umi.com/33/48/3348246.html

Girard, M. J., Downs, J. C., & Burgoyne, C. F. (2009). Peripapillary and Posterior Scleral Mechanics---Part I: Development of An Anisotropic Hyperelastic Constitutive Model. *Journal of Biomechanical Engineering , 131* (5), 051011.

Girard, M. J., Downs, J. C., Bottlang, M., Burgoyne, C., & F. Suh, J.-K. F. (2009). Peripapillary and Posterior Scleral Mechanics, Part II – Experimental and inverse Finite Element Characterization. *Journal of Biomechanical Engineering , 131* (5), 051012.

Girard, M. J., Downs, J. C., Burgoyne, C. F., & Suh, J.-K. F. (2008). Experimental Surface Strain Mapping of Porcine Peripapillary Sclera Due To Elevations of intraocular Pressure. *Journal of Biomechanical Engineering , 130* (4), 041017.

Girard, M. J., Downs, J. C., Burgoyne, C. F., & Suh, J.-K. F. (2008). Experimental Surface Strain Mapping of Porcine Peripapillary Sclera Due To Elevations of intraocular Pressure. *Journal of Biomechanical Engineering , 130* (4), 041017.

Girard, M., Dahlmann, A., Vijay, S., Khaw, P., & Ethier, C. (2010). Quantitative Mapping of Scleral Fiber Orientation in Normal Rat Eyes. *2128/A227* (P. May 03). Fort Lauderdale: ARVO.

Girkin, C. A., Mcgwin, G., & Xie, A. (2005). Differences in Optic Disc Topography Between Black and White Normal Subjects. *Ophthalmology , 112* (1), 33-39.

Goodman, J. W. (1975). Statistical Properties of Laser Speckle Patterns. *Laser Speckle and Related Phenomena*.

Greene, P. (1980). Mechanical Considerations in Myopia: Relative Effects of Accommodation, Convergence, intraocular Pressure, and the Extraocular Muscles. *American Journal of Optometry and Physiological Optic , 57* (12), 902-914.

Grytz, R., & Meschke, G. (2010). A Computational Remodeling Approach To Predict the Physiological Architecture of the Collagen Fibril Network in Corneo-Scleral Shells. *Biomechanics and Modeling in Mechanobiology , 9* (2), 225-235.

Grytz, R., & Meschke, G. (2009). Constitutive Modeling of Crimped Collagen Fibrils in Soft Tissues. *Journal of the Mechanical Behavior of Biomedical Materials , 2* (5), 522-533.

Grytz, R., Meschke, G., & Jonas, J. B. (2010). The Collagen Fibril Architecture in the Lamina Cribrosa and Peripapillary Sclera Predicted By a Computational Remodeling Approach. *Biomechan*ics *and Modeling in* Mechano*biology* . Jul 14. Epub.

H, H., F, M., H, S. F., & J, S. (1995). Evidence of Constriction of Optic Nerve Axons At the Lamina Cribrosa in the Normotensive Eye in Humans and Other Mammals. *Ophthalmic Research , 27* (5), 296-309.

Hayreh, S. S. (1986). Pathogenesis of Optic Nerve Head Changes in Glaucoma. *Seminars in Ophthalmology, 1* (1), 1-13.

Hernandez MR, L. X. (1989). Age-Related Changes in the Extracellular Matrix of the Human Optic Nerve Head. *American Journal of Ophthalmology , 107* (5), 476-484.

Hong, T.-P., Wang, H.-S., Lin, W.-Y., & Lee, W.-Y. (2002). Evolution of Appropriate Crossover and Mutation Operators in A Genetic Process. *Applied intelligence , 16* (1), 7-17.

Hong, T.-P., Wang, H.-S., Lin, W.-Y., & Lee, W.-Y. (2002). Evolution of Appropriate Crossover and Mutation Operators in A Genetic Process. *Applied intelligence , 16* (1), 7-17.

Hung, Y. Y., Wang, J. Q., & Hovanesian, J. D. (1997). Technique for Compensating Excessive Rigid Body Motion in Nondestructive Testing of Large Structures Using Shearography. *Optics and Lasers in Engineering , 26* (2-3), 249-258.

Huntley, J. M. (1997). Random Phase Measurement Errors in Digital Speckle Pattern interferometry. *Optics and Lasers in Engineering , 26* (2-3), 131-150.

Jeffery, G., Evans, A., Albon, J., Duance, V., Neal, J., & Dawidek, G. (1995). The Human Optic Nerve: Fascicular Organisation and Connective Tissue Types Along the Extra-Fascicular Matrix. *Anatomy and Embryology , 191* (6), 491-502.

Joenathan, C., Haible, P., & Tiziani, H. J. (1999). Speckle interferometry With Temporal Phase Evaluation: influence of Decorrelation, Speckle Size, and Nonlinearity of the Camera. *Applied Optics , 38* (7), 1169-1178.

Kao, B., & Razgunas, L. (1986, 04 22). On the Determination of Strain Energy Functions of Rubbers. *SAE international* .

Knox Cartwright, N. E., Tyrer, J. R., & Marshall, J. (2010, September). Age-Related Differences in the Elasticity of the Human Cornea. *Investigative Ophthalmology & Visual Science* , Iovs.09-4798.

Kokott, W. (1934). Das Spaltlinienbild Der Sklera. (Ein Beitrag Zum Funktionellen Bau Der Sklera). *Klin Mbl Augen , 92*, 177-185.

Komai, Y., & Ushiki, T. (1991). The Three-Dimensional Organization of Collagen Fibrils in the Human Cornea and Sclera. *Investigative Ophthalmology and Visual Science , 32* (8), 2244-2258.

Lawrence Livermore National Laboratory. (S.D.). Tratto Da Https://Www-Eng.Llnl.Gov/Mdg/Mdg_Codes_Nike3d.Html

Lawrence Livermore National Laboratory. (2010, August 13). *Methods Development Group - Nike3D*. Retrieved From Engineereing At LLNL: Https://Www-Eng.Llnl.Gov/Mdg/Mdg_Codes_Nike3d.Html

Lehmann, M. (1997). Decorrelation-induced Phase Errors in Phase-Shifting Speckle interferometry. *Applied Optics , 36* (16), 3657-3667.

Lesk, M. R., Hafez, A. S., & Descovich, D. (2006). Relationship Between Central Corneal Thickness and Changes of Optic Nerve Head Topography and Blood Flow After intraocular Pressure Reduction in Open-Angle Glaucoma and Ocular Hypertension. *Archives of Ophthalmology, 124* (11), 1568-1572.

Leske, M. C., Connell, A. M., Wu, S.-Y., Hyman, L., & Schachat, A. P. (1997). Distribution of intraocular Pressure: the Barbados Eye Study. *Archives of Ophthalmology , 115* (8), 1051-1057.

Leskea, M. C., Heijl, A., Hyman, L., Bengtsson, B., & Komaroff, E. (2003). Factors for Progression and Glaucoma Treatment: The Early Manifest Glaucoma Trial. *Current Opinion in Ophthalmology , 121* (1), 48-56.

Levene, R. Z. (1980). Low Tension Glaucoma: A Critical Review and New Material. *Survey of Ophthalmology , 24* (6), 621-664.

Molimard, J., Cordero, R., & Vautrin, A. (2008). Signal-To-Noise Based Local Decorrelation Compensation for Speckle interferometry Applications. *Applied Optics , 47* (19), 3535-3542.

Morrison, J. C., Lhernault, N. L., Jerdan, J. A., & Quigley, H. A. (1989). Ultrastructural Location of Extracellular Matrix Components in the Optic Nerve Head. *Archives of Ophthalmology , 107* (1), 123-129.

Nicolela MT, D. S. (1996). Various Glaucomatous Optic Nerve Appearances: Clinical Correlations. *Ophthalmology , 103* (4), 640-649.

Nicoli, S., Ferrari, G., Quarta, M., Macaluso, C., Govoni, P., Dallatana, D., Et Al. (2009). Porcine Sclera as a Model of Human Sclera for in Vitro Transport Experiments: Histology, SEM, and Comparative Permeability. *Molecular Vision , 15* (Epub 2009 Feb), 259-266.

Oliver, W. C., & Pharr, G. M. (1992). An Improved Technique for Determining Hardness and Elastic Modulus Using Load and Displacement Sensing indentation Experiments. *Journal of Materials Research , 7* (6), 1564-1583.

Oyama, T., Abe, H., & Ushiki, T. (2006). The Connective Tissue and Glial Framework in the Optic Nerve Head of the Normal Human Eye: Light and Scanning Electron Microscopic Studies. *Archives of Histology and Cytology , 69* (5), 341-356.

Pinsky, P. M., Dolf, V. D., & Dimitri, C. (2005). Computational Modeling of Mechanical Anisotropy in the Cornea and Sclera. *Journal of Cataract & Refractive Surgery , 31* (1), 136-145.

Price, K., Storn, R. M., & Lampinen, J. A. (2005). *Differential Evolution - A Practical Approach To Global Optimization* (Vol. 20). Berlin, Germany: Springer.

Quigley, H. A., & Addicks, E. M. (1981). Regional Differences in the Structure of the Lamina Cribrosa and their Relation To Glaucomatous Optic Nerve Damage. *Archives of Ophthalmology , 99* (1), 137-143.

Quigley, H. A., & Addicks, E. M. (1981). Regional Differences in the Structure of the Lamina Cribrosa and their Relation To Glaucomatous Optic Nerve Damage. *Archives of Ophthalmology , 99* (1), 137-143.

Quigley, H. (1995). *Overview and introduction To Session On Connective Tissue of the Optic Nerve in Glaucoma.* in: Drance SM, anderson DR. *Optic Nerve in Glaucoma.* (Chapter 2). Amsterdam/New York: Kugler.

Quigley, H., Brown, A., Morrison, J., & Drance, S. (1990). The Size and Shape of the Optic Disc in Normal Human Eyes. *Archives of Ophthalmology , 108* (1), 51-57.

Rada, J. A., Shelton, S., & Norton, T. T. (2006). The Sclera and Myopia. *Experimental Eye Research , 82* (2), 185-200.

Rubbens, M. P., Mol, A., Boerboom, R. A., Bank, R. A., & Baaijens, F. P. (2009). Intermittent Straining Accelerates the Development of Tissue Properties in Engineered Heart Valve Tissue. *Tissue Engineering , 15* (5), 999-1008.

Rudnicka, A. R., Mt-Isa, S., Owen, C. G., Cook, D. G., & ashby, D. (2006). Variations in Primary Open-Angle Glaucoma Prevalence By Age, Gender, and Race: A Bayesian Meta-Analysis. *Investigative Ophthalmology & Visual Science , 47* (10), 4254-4261.

Schmitt, L. M. (2001). Theory of Genetic Algorithms. *Theoretical Computer Science , 259* (1-2), 1-61.

Sigal, I. A., & Ethier, C. R. (2009). Biomechanics of the Optic Nerve Head. *Experimental Eye Research , 88* (4), 799-807.

Sigal, I. A., Flanagan, J. G., & Ethier, C. R. (2005). Factors influencing Optic Nerve Head Biomechanics. *Investigative Ophthalmology & Visual Science , 46* (11), 4189-4199.

Sigal, I. A., Flanagan, J. G., Tertinegg, I., & Ethier, C. R. (2004). Finite Element Modeling of Optic Nerve Head Biomechanics. *Investigative Ophthalmology & Visual Science , 45* (12), 4378-4387.

Sirohi, R. S. (2002). Speckle interferometry. *Contemporary Physics , 43* (3), 161-180.

Sirohi, R. S. (1993). *Speckle Metrology.* New York: Marcel Dekker.

Soung-Min, I., & Ju-Jang, L. (2008). Adaptive Crossover, Mutation and Selection Using Fuzzy System for Genetic Algorithms. *Artificial Life and Robotics , 13* (1), 129-133.

Spencer, A. J. (1985). *Continuum Theory of the Mechanics of Fibre-Reinforced.* New York: Springer-Verlag.

Steinchen, W., Kupfer, G., Mäckel L, P., & Vössing, F. (1999). Determination of Strain Distribution By Means of Digital Shearography. *Measurement , 26* (2), 79-90.

Takai, N., & asakura, T. (1985). Statistical Properties of Laser Speckles Produced Under Illumination From A Multimode Optical Fiber. *Journal of the Optical Society of America, 2*, 1282-1290.

the Advanced Glaucoma intervention Study (AGIS): 12. Baseline Risk Factors for Sustained Loss of Visual Field and Visual Acuity in Patients With Advanced Glaucoma. (2002). *American Journal of Ophthalmology , 134*, 499-512.

Timoshenko, S. (1940). T*heory of Plates and Shells.* New York: Mcgraw-Hill Book Company.

Tyrer, J. R., & Petzing, J. N. (1997). In-Plane Electronic Speckle Pattern Shearing interferometry. *Optics and Lasers in Engineering , 26* (4-5), 395-406.

Vest, C. (1979). *Holographic interferometry.*

Weih, L. M., Mukesh, B. N., Mccarty, C. A., & Taylor, H. R. (2001). Association of Demographic, Familial, Medical, and Ocular Factors with intraocular Pressure. *Archives of Ophthalmology , 119* (6), 875-880.

Weiss, J. A., Maker, B. N., & Govindjee, S. (1996). Finite Element Implementation of incompressible, Transversely Isotropic Hyperelasticity. *Computer Methods in Applied Mechanics and Engineering , 135*, 107-128.

Wolff, J. (1892). *Das Gesetz Der Transformation Der Knochen. Berlin A. Hirchwild.* Hirchwild, Berlin: Springer-Verlag.

Woo, S., Kobayashi, A., Schlegel, W., & Lawrence, C. (1972). Nonlinear Material Properties of intact Cornea and Sclera. *Experimental Eye Research , 14* (1), 29-39.

Yan, D. B., Coloma, F. M., Metheetrairut, A., Trope, G. E., Heathcote, J. G., & Ethier, C. R. (1994). Deformation of the Lamina Cribrosa By Elevated intraocular Pressure. *British Journal of Ophthalmology , 78* (8), 643-648.

Yan, D., Mcpheeters, S., Johnson, G., Utzinger, U., & Vande Geest, J. (2010, November). Microstructural Differences in the Human Posterior Sclera as A Function of Age and Ethnicity. *Investigative Ophthalmology & Visual Science* , Iovs.09-4651.

Zeimer R. Biomechanical Properties of the Optic Nerve Head. Drance SM Eds. Optic Nerve in Glaucoma. (1995). Kugler.

Zeimer, R. (1995). *Biomechanical Properties of the Optic Nerve Head. Optic Nerve in Glaucoma.* New York: Kugler.

Zeimer, R. C., & Ogura, Y. (1989). The Relation Between Glaucomatous Damage and Optic Nerve Head Mechanical Compliance. *Archives of Ophthalmology , 107* (8), 1232-1234.

Zeimer, R., Wilensky, J. T., Goldberg, M. F., & Solin, S. A. (1981). Noninvasive Measurement of Optic Nerve-Head Compliance by Laser Doppler Velocimetry. *Journal of the Optical Society of America , 71* (4), 499-501.

Zemánek, M., Burša, J., & Děták, M. (2009). Biaxial Tension Tests With Soft Tissues of Arterial Wall. *Engineering Mechanics , 16* (1), 3-11.